

VORTEX FORMATION BY MERGING AND INTERFERENCE OF MULTIPLE TRAPPED BOSE-EINSTEIN CONDENSATES

by

David René Scherer

A Dissertation Submitted to the Faculty of the

COLLEGE OF OPTICAL SCIENCES

In Partial Fulfillment of the Requirements
For the Degree of

DOCTOR OF PHILOSOPHY

In the Graduate College

THE UNIVERSITY OF ARIZONA

2 0 0 7

THE UNIVERSITY OF ARIZONA
GRADUATE COLLEGE

As members of the Final Examination Committee, we certify that we have read the dissertation prepared by David René Scherer entitled Vortex Formation by Merging and Interference of Multiple Trapped Bose-Einstein Condensates and recommend that it be accepted as fulfilling the dissertation requirement for the Degree of Doctor of Philosophy.

Brian Anderson

Date: 2 March 2007

Alexander Cronin

Date: 2 March 2007

Poul Jessen

Date: 2 March 2007

Final approval and acceptance of this dissertation is contingent upon the candidate's submission of the final copies of the dissertation to the Graduate College.

I hereby certify that I have read this dissertation prepared under my direction and recommend that it be accepted as fulfilling the dissertation requirement.

Dissertation Director: Brian Anderson

Date: 2 March 2007

STATEMENT BY AUTHOR

This dissertation has been submitted in partial fulfillment of requirements for an advanced degree at The University of Arizona and is deposited in the University Library to be made available to borrowers under rules of the Library.

Brief quotations from this dissertation are allowable without special permission, provided that accurate acknowledgment of source is made. Requests for permission for extended quotation from or reproduction of this manuscript in whole or in part may be granted by the head of the major department or the Dean of the Graduate College when in his or her judgment the proposed use of the material is in the interests of scholarship. In all other instances, however, permission must be obtained from the author.

SIGNED: _____
David René Scherer

ACKNOWLEDGEMENTS

First I'd like to thank my advisor, Brian Anderson, for teaching me the importance of critical thinking, persistence, and working in a team. Through his mentorship and guidance, Brian has taught me how to zero in on and think critically about the important parts of a problem, and, equally importantly, what parts to ignore. In the years since I've been working with Brian, what I've learned about technical problem solving, physical intuition, and working in a team successfully have been a direct result of his mentorship.

I couldn't have completed this dissertation had it not been for the contributions of many other students in our group: Chad Weiler, Tyler Neely, Dave Henry, Elaine Ulrich, Dave Kaz, and Tim McComb. Chad and I have worked together for many years, and I am continually amazed by his optimism and positive outlook. Chad's energy seems to fly in the face of experimental breakdowns or lack of results, when things get difficult, he is still able to approach everything with a positive attitude. Tyler has been a great addition to our research group, the experiment is in good hands with his meticulous attention to detail. Until I had worked with Dave Henry, I had never seen so much enthusiasm in an adult. Dave's persistence, high energy, and unwillingness to rest until the problem he happens to be working on is solved will always amaze me. Elaine built a lot of the early stages of the experimental apparatus. Dave Kaz provided some of the funniest and most creative experiences our lab has ever seen, and Tim McComb built a diode laser in the most impressively efficient way possible.

It has been a pleasure to interact with several other faculty members at the University of Arizona. I thank Poul Jessen for teaching me most of what I know about quantum mechanics, in a mathematically rigorous way that I really connected with. I appreciate Alex Cronin for always asking probing questions, and being genuinely interested in everything under the sun. Jim Wyant has been enormously supportive during my time as a graduate student and I appreciate him as a mentor.

My friends Souma and O have provided camaraderie and companionship over the many years of working on difficult atomic physics experiments.

I thank Susan Meyers for her support, friendship, and continued willingness to go on adventures with me.

Finally, I'd like to thank my parents, my sisters, and all the members of my extended family. My parents provided an environment at home in which creativity and individuality flourished, and always supported my myriad (and always changing) interests. I credit that environment with sparking my initial interest in science, and the support network of my entire family is what enabled me to finish the Ph.D.

DEDICATION

To my sisters: Stephanie and Elisabeth

TABLE OF CONTENTS

LIST OF FIGURES	9
LIST OF TABLES	11
ABSTRACT	12
CHAPTER 1 INTRODUCTION	13
1.1 Bose-Einstein Condensation: Some Preliminary Concepts	13
1.2 Outline of this Dissertation	16
CHAPTER 2 BUILDING A BEC LABORATORY: LASER COOLING AND MAGNETIC TRAPPING	17
2.1 Introduction	17
2.1.1 Building a BEC laboratory: the basic steps	17
2.1.2 A review of the literature: other experimental descriptions	18
2.2 Computer Timing System	19
2.2.1 Overview of how LabVIEW controls the experiment	20
2.2.2 Computer boards used	20
2.3 Vacuum System	25
2.3.1 Design of a dual-chamber system	27
2.3.2 Vacuum system construction and baking	32
2.3.3 Vacuum system integrity test	40
2.4 Lasers	41
2.4.1 MBR laser and lock	43
2.4.2 Diode laser construction	47
2.4.3 Repump laser and lock	49
2.4.4 Probe laser and lock	52
2.5 MOT	55
2.5.1 Magneto-optical trapping using diverging beams	55
2.6 CMOT	60
2.7 Optical Pumping	62
2.8 Initial Magnetic Trap	62
CHAPTER 3 MAGNETIC TRANSFER OF ATOMS TO SCIENCE CELL	64
3.1 Introduction	64
3.2 Overview of the Magnetic Transfer System	64

TABLE OF CONTENTS – *Continued*

3.3	Hardware Used in the Magnetic Transfer System	66
3.3.1	Overview of components used	66
3.3.2	Magnet coils and mounts	69
3.3.3	Power supply and ground	72
3.3.4	Sample-and-hold circuit	73
3.3.5	Transfer control box	76
3.3.6	MOSFET boxes	81
3.3.7	Diode box	82
3.3.8	Safety interlock box	84
3.3.9	Direction of current flow	87
3.4	Calculation of the Current Sequence	87
3.5	Transfer Revisited	93
CHAPTER 4 BEC FORMATION AND IMAGING		95
4.1	Introduction	95
4.2	TOP Trap	95
4.2.1	Physical layout of TOP trap	96
4.2.2	Electronics used in TOP trap	101
4.2.3	Transfer into TOP trap	105
4.3	RF Coils	106
4.4	Evaporative Cooling	107
4.4.1	Initial evaporation in the tight TOP trap	108
4.4.2	Evaporative cooling in a weakly-confining TOP trap	108
4.5	Imaging	111
4.5.1	Overview, physical layout of imaging systems	111
4.5.2	Absorption imaging	117
4.5.3	Phase-contrast imaging	121
4.5.4	Image processing and analysis	122
4.6	Final BEC Characteristics	125
4.7	Complete Timing Sequence	127
CHAPTER 5 VORTEX FORMATION		130
5.1	Introduction	130
5.2	The Concept of Phase in a BEC	130
5.2.1	The superfluid velocity and quantized vortices	131
5.2.2	On the relative phase of independent superfluids	133
5.2.3	Example case: interference between two BECs	134
5.2.4	Matter-wave interference between two expanding BECs	134

TABLE OF CONTENTS – *Continued*

5.3	Research Question: <i>Can vortices be made by merging and interfering independent superfluids?</i>	136
5.4	Experimental Details	138
5.4.1	BEC formation	138
5.4.2	Three-well atom trap	139
5.4.3	Making a custom-shaped optical potential	140
5.4.4	Direction of fluid flow for given relative phases	141
5.4.5	Timescale for merging	145
5.4.6	Making a vortex lattice by rotating an asymmetric TOP trap	146
5.5	Vortex Formation by Merging Independent BECs	150
5.5.1	Formation of independent BECs	150
5.5.2	Vortex observation fraction vs. merging time	151
5.6	Vortex Formation During BEC Creation	154
5.6.1	Experimental sequence	154
5.6.2	Discussion	156
5.6.3	Intermediate potential barriers	156
5.7	Vortex Formation by Splitting and Recombining a BEC	157
5.8	Spontaneous Vortices	158
5.9	Numerical Simulations	159
5.10	Where Does the Angular Momentum Come From?	160
CHAPTER 6 CONCLUSIONS		161
6.1	A Review of the Experimental Apparatus	161
6.2	A Summary of the Experimental Results	162
6.3	Directions for Future Research	163
APPENDIX A COHERENT MBR-110 AND VERDI V-10 LASER OPERATION TIPS		165
REFERENCES		171

LIST OF FIGURES

2.1	Computer and computer boards used to control the experiment . . .	21
2.2	Opto-isolator circuit schematic	22
2.3	DAC circuit	24
2.4	Schematic of vacuum system	27
2.5	Photograph of vacuum system	28
2.6	Photograph showing magnetic transfer coils and vacuum system . . .	29
2.7	Vacuum integrity test	42
2.8	^{87}Rb energy levels	43
2.9	MBR laser lock	45
2.10	Photograph of diode laser	48
2.11	Repump laser lock	51
2.12	Probe laser lock	53
2.13	Photograph of MOT optics	57
2.14	Schematic of MOT circuit	59
3.1	Top-view photograph of magnetic transfer coils	65
3.2	Schematic of the overall transfer system	67
3.3	Photograph of a single magnet coil	69
3.4	Illustration of sample-and-hold technique	75
3.5	Schematic of the transfer circuit	77
3.6	Sections of the transfer circuit	78
3.7	Photograph of a MOSFET box	83
3.8	Coil locations, current ramps, and field gradients for magnetic transfer system	91
4.1	Photograph of TOP trap	97
4.2	Schematic of the TOP trap mount and nearby coils	99
4.3	Schematic of DC TOP circuit	102
4.4	AC TOP coils driving circuit	103
4.5	Phase-shifter circuit	104
4.6	Evaporative cooling sequence	110
4.7	Layout of horizontal and vertical imaging systems	112
4.8	ZEMAX layout of horizontal imaging system	115
4.9	ZEMAX spot diagram for horizontal imaging system	116
4.10	Vertical absorption image	120
4.11	Horizontal phase-contrast image	123

LIST OF FIGURES – *Continued*

4.12	BEC transition data	126
4.13	Complete BEC formation timing sequence	129
5.1	2π phase winding of a singly-charged vortex	133
5.2	Three-well potential	139
5.3	Experimental setup, including optical barrier beam	142
5.4	Illustration showing which relative phases can lead to a vortex	144
5.5	Vortex lattice	149
5.6	Images showing only a few vortices created by rotating an asymmetric TOP trap	150
5.7	Image of trapped condensates formed in the presence of a strong barrier	151
5.8	Example images of vortices created by merging independent BECs . .	152
5.9	Image of a BEC formed in the presence of a weak barrier	155
5.10	Gallery of images from weak, intermediate and zero barrier strengths	155
5.11	Vortex observation fraction for splitting and then recombining three condensates	158

LIST OF TABLES

3.1	Coil locations	71
3.2	Coil configurations	71
4.1	Parameters for DC and AC TOP coils	98

ABSTRACT

An apparatus for producing atomic-gas Bose-Einstein condensates (BECs) of ^{87}Rb atoms is described. The apparatus produces ^{87}Rb BECs in a dual-chamber vacuum system that incorporates magnetic transport of trapped atoms from the magneto-optical trapping cell to the BEC production cell via the operation of a series of overlapping magnet coils. The design, construction, and operation of the apparatus are described in detail.

The apparatus is used to study the creation of quantized vortices in BECs by the merging and interference of multiple trapped condensates. In this experiment, a single harmonic potential well is partitioned into three sections by an optical barrier, enabling the simultaneous formation of three independent, uncorrelated BECs. The BECs may either merge together during their growth, or, for high-energy barriers, the BECs can be merged together by barrier removal after their formation. Either process may instigate vortex formation in the resulting BEC, depending on the initially indeterminate relative phases of the condensates and the merging rate.

CHAPTER 1

INTRODUCTION

1.1 Bose-Einstein Condensation: Some Preliminary Concepts

A Bose-Einstein condensate (BEC) is a coherent collection of bosonic atoms that all occupy the same quantum state [1, 2, 3]. When a dilute atomic gas is cooled below a density-dependent critical temperature T_c , a temperature-dependent fraction of the atoms undergo a quantum phase transition to form a new state of matter: the Bose-Einstein condensate [4, 5, 6]. One important consequence of the decrease in temperature of the atoms during BEC formation is an increase in the atoms' thermal de Broglie wavelength [7]. For example, as the ^{87}Rb atoms in our experiment are cooled from room temperature to $T_c \approx 20$ nK, their de Broglie wavelength increases by ~ 6 orders of magnitude to $\lambda_{dB} \approx 1 \mu\text{m}$. Such large macroscopic wavelengths have enabled a wide variety of wave-physics experiments involving atomic matter waves. More to the point, the large coherence length of a BEC (which can be up to tens of microns) has enabled many experiments within the field of atom optics [8] that involve the propagation, interference, and control of atomic matter waves.

The atoms in a BEC share the same property of coherence [9] as the photons in a laser beam; if two separate BECs are brought into contact, they are able to constructively or destructively interfere, depending on their relative phase. This *matter-wave interference* is similar to the interference of two light waves, and can exhibit a pattern of bright (many atoms) and dark (few atoms) interference fringes.

In fact, one of the first experiments within the field of BEC was similar to Thomas Young's double-slit experiment of 1805 [10], which paved the way for our contemporary understanding of the wave properties of light. In the analogous BEC experiment, reported by Andrews *et al.* in 1997 [11], two initially isolated condensates were physically overlapped, allowing them to interfere, and matter-wave interference fringes were observed. This experiment will be discussed in the context of matter-wave interference between BECs in more detail in Section 5.2.4.

If matter-wave interference fringes are one possible outcome of bringing two independent BECs into contact, the other extreme is the merging of two BECs into one coherent condensate, an experiment that was reported by Chikkatur *et al.* in 2002 [12]. In this experiment, a continuous source of Bose-Einstein condensed atoms was realized by the merging of multiple condensates.

In the experiments presented in this dissertation, *three* independent condensates are merged while remaining trapped, and may or may not exhibit interference fringes based on the timescale of merging, a parameter that will be discussed in Section 5.4.5. The results of these experiments demonstrate a novel outcome of condensate merging: the formation of quantized vortices.

As a system with a macroscopic occupation of a single quantum state that can be described by a single many-body wavefunction, a BEC can be considered a superfluid [13]. One of the defining characteristics of a superfluid is its response to rotation: in superfluids, rotation of the system can result in the formation of quantized vortices of fluid flow around a fluid-free core. In the case of a BEC, rotation will set the atoms in motion at a velocity that is dependent on the local phase gradient of the condensate. But because the wavefunction of the superfluid must be

single-valued, the phase of the wavefunction after motion around a closed loop must be either the same as its original value, or different by a multiple of 2π . The latter describes a situation in which a *vortex* of quantized orbital angular momentum exists in the superfluid, described in more detail in Section 5.2.1. These vortices are the hallmark feature of superfluidity, and have been created in BEC by a number of different methods [14]. Most of these methods have involved the deliberate introduction of orbital angular momentum into the BEC, which manifests itself as the appearance of quantized vortices.

A new mechanism for vortex generation in BECs, presented in Chapter 5, is novel in that it relies on matter-wave interference between trapped condensates with indeterminate phase differences. In our experiment, three independent condensates are merged together while remaining trapped, and the direction of atomic flow caused by the merger depends on the relative phases of the condensates, a quantity that is not known *a priori*. For certain conditions in the relative phases, a circular atomic flux will ensue, resulting in the orbital angular momentum necessary to create vortices within the condensate. The vortex observation fraction and the timescale for ensuing dynamics after the merger are consistent with a simple conceptual model.

The purpose of this dissertation is to describe in detail the experimental apparatus used to form our BEC and the results of the aforementioned experiment. Before proceeding further, the following section provides an outline of the entire dissertation.

1.2 Outline of this Dissertation

The bulk of this dissertation is devoted to a detailed description of the entire experimental apparatus used by our research group to generate, manipulate, and probe our BEC. As the first student in Dr. Brian Anderson's research group, I have had the opportunity be involved in all aspects of building a BEC experiment from scratch, and all aspects of our experimental apparatus are catalogued in Chapters 2, 3, and 4. Although atomic-gas BECs have been around since 1995, there is no single best way to set up a BEC experiment. We present the method we have chosen to use, along with many of its advantages and disadvantages.

Our method of BEC production can be divided into three basic steps: (1) loading atoms in a magneto-optical trap; (2) magnetically transferring the trapped atoms to a lower-pressure region of the vacuum chamber; and (3) evaporatively cooling the atoms to form a BEC. These three basic steps are described in Chapters 2, 3, and 4, respectively.

The principal scientific result of this dissertation is the discovery of a novel mechanism for vortex formation in superfluids [15], described in Chapter 5. This chapter includes a discussion of the background information and concepts relevant to our experiment, the experimental procedure, and the results and conclusions of our findings.

A summary of the major results presented in this dissertation can be found in Chapter 6, which includes a review of the experimental apparatus, a summary of the experimental results, and a discussion of further research that can be done to continue the work presented in this dissertation.

CHAPTER 2

BUILDING A BEC LABORATORY: LASER COOLING AND MAGNETIC TRAPPING

2.1 Introduction

Chapters 2, 3, and 4 describe what the bulk of my time as a graduate student was spent doing: building a BEC laboratory from scratch. The construction details and steps needed to build all the components of our experimental apparatus are presented in the chronological order in which we built them. This chapter describes the first step in the BEC formation process: trapping atoms in a Magneto-optical trap (MOT) and transferring them into the initial magnetic trap.

Before proceeding on with a description of the components used in laser cooling and magnetic trapping, a basic overview of the construction timeline for building a BEC laboratory and a literature review are presented. Then, a description of the hardware used, such as the computer timing system, vacuum system, and lasers, is presented. Finally, descriptions of the MOT and trapping atoms in the initial magnetic trap are presented.

2.1.1 Building a BEC laboratory: the basic steps

The basic steps we followed in order to build our experimental apparatus are:

1. We constructed a computer timing program capable of controlling the many devices needed to operate in sequence to form a BEC.

2. We built a vacuum chamber containing a source of ^{87}Rb atoms.
3. We built lasers and laser locks that we use to cool, manipulate, and probe an atomic gas.
4. We implemented a Magneto-optical Trap (MOT) of $\sim 10^9$ ^{87}Rb atoms.
5. We magnetically trapped atoms and transferred them into a Time-averaged Orbiting Potential (TOP) trap.
6. We evaporatively cooled the atoms through the critical temperature to create a Bose-Einstein Condensate (BEC).
7. We built the imaging systems we use to extract information about the condensate.

2.1.2 A review of the literature: other experimental descriptions

There is no single best way to go about constructing an experimental BEC apparatus, many different groups have chosen to do things a particular way because of various historical and technical reasons. What we provide in this chapter is the hows and whys of our experimental apparatus, but there are numerous other places to go for technical information on building all or part of the components necessary for a BEC experiment.

The first experimental observation of BEC was made in 1995 in the group of Eric Cornell and Carl Wieman at JILA [16], and was followed shortly thereafter in the groups of Wolfgang Ketterle at MIT [17] and Randall Hulet at Rice [18, 19]. Our experimental approach follows more closely the lineage of the current JILA experiments, which tend to favor smaller vacuum systems and the use of Rb

dispensers, rather than the MIT approach, which involves a larger vacuum system and a Zeeman slower.

The first experimental dissertation on BECs was written by Jason Ensher [20], and it contains a detailed description of the experimental approach used in the first JILA BEC experiment as well as a wealth of details on the TOP trap. The dissertation of Heather Lewandowski [21] includes valuable information on building a BEC experiment from scratch, and includes descriptions of many of the same technical issues as this dissertation. The dissertation of Brian DeMarco [22] includes information on building a similar experiment for fermions, and is a good resource for its many figures and electronics schematics on driving magnet coils. The dissertation of Michael Matthews [23] contains a thorough description of many of the different methods used for imaging a condensate. Paul Haljan's dissertation [24] includes updated and more complete information on phase-contrast imaging. Descriptions of the basics of building a BEC experiment can be found in the review articles written by the JILA group [25] and the MIT group [26]. A detailed description of the methods used by the MIT group, particularly useful for imaging and image processing, can be found in Dan Stamper-Kurn's dissertation [27] and in Ref. [28].

2.2 Computer Timing System

Contemporary experiments in ultracold atomic physics require precise control of lasers, magnetic fields, and other devices on the nanosecond timescale. For this reason, a computer timing system was built that controls the experiment through the use of the commercial software package LabVIEW. LabVIEW interfaces with the computer boards, which themselves interface with various devices in our laboratory

to control the experiment.

2.2.1 Overview of how LabVIEW controls the experiment

One PC with four computer interface boards is used to control the experiment. This PC uses several different programs, written using the software packages LabVIEW and Matlab, to run the experiment. The main LabVIEW program interfaces with computer boards which are capable of reading analog inputs and controlling the experiment using both analog and digital outputs. The program controls the creation of a BEC, controls a subsequent experiment with the BEC, and then triggers the image acquisition on a CCD camera. A separate computer controls the CCD camera parameters and is used for image acquisition and analysis.

2.2.2 Computer boards used

Figure 2.1 shows an overview of the different computer boards and how they fit together with the experiment. The experiment PC contains 4 computer boards: a Viewpoint DIO-128 digital input/output board, a National Instruments (NI) PCI-6023E analog input board, a NI PCI-6713 analog output board, and a GPIB board. The GPIB board is used to load an arbitrary waveform onto a function generator, this is described in Section 3.3.4 on Page 73. The following sections describe the remaining computer boards and components (opto-isolator boxes, breakout boxes, DAC, and transfer control circuit) shown in Figure 2.1.

DIO-128 digital output board

The workhorse computer board in our experiment is the Viewpoint DIO-128 digital output board, which has 4 ports (labeled Ports A, B, C, and D) of 16 digital output

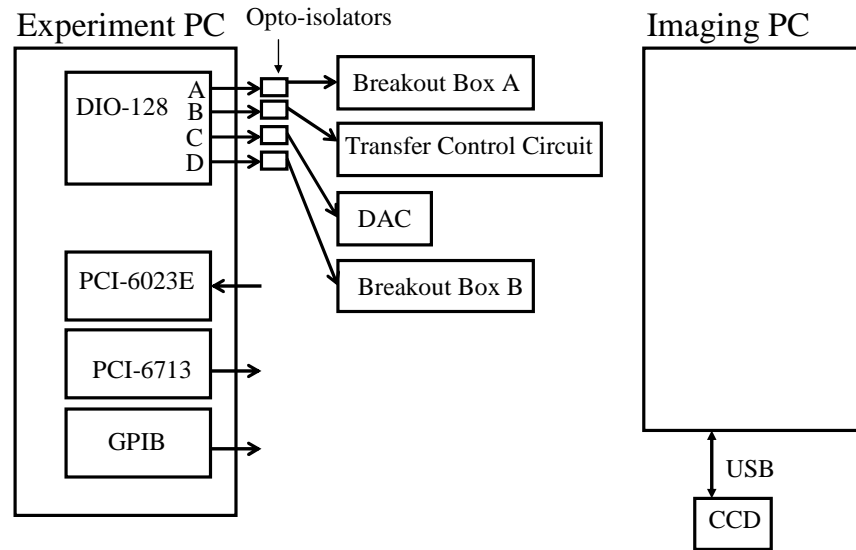


Figure 2.1: Computers and computer boards used to control the experiment. The ‘Experiment PC’ contains four computer boards: the DIO-128 Digital Input/Output board, the PCI-6023E Analog Input board, the PCI-6713 Analog Output board, and the GPIB board. The four Ports (A, B, C, and D) on the DIO-128 connect with Breakout Box A, the Transfer Control Circuit, the DAC, and Breakout Box B. The ‘Imaging PC’ communicates with the CCD camera through a USB connection.

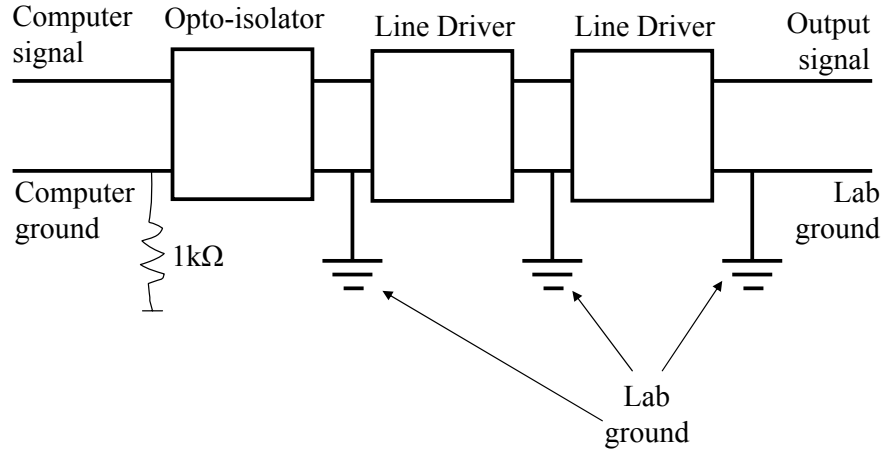


Figure 2.2: Schematic showing the circuit used for isolation of computer ground from lab ground. Each digital line on the DIO-128 passes through an opto-isolator, which isolates computer ground from lab ground, then passes through two line drivers. Each line driver inverts the signal, so the output signal is a faithful representation of the original computer signal, but is referenced to lab ground.

lines each. This board is used to turn on and off various devices in the experiment, such as shutters, laser beams, magnets, etc. with precise timing.

Each digital line on the DIO-128 must be carefully electrically isolated so as to avoid ground loops. A potential problem occurs when an electrical signal is reflected from a lab device back into the computer, which can destroy the board. To prevent this, electrical isolation of the computer ground from the lab ground is necessary. A schematic of the opto-isolator circuit is shown in Figure 2.2.

Each digital line from the DIO-128 is first sent through an Agilent HCPL-220 opto-isolator, which electrically isolates the input and output signals and grounds with an optical signal. This ensures that the computer ground is not connected to the lab ground in any of our electronics boxes. Then each signal is sent through a TI SN74128 line driver that provides the digital line with additional current output

capability. The line driver inverts the digital signal, so each line is sent through two line drivers. This is done for all of the digital lines directly after the DIO-128 ribbon cable, before they connect to lab devices.

Port A of the DIO-128 connects to Breakout Box A, visible on the equipment rack in our lab. This Port is responsible for turning on and off many devices in our lab, such as shutters, AOMs, and the MOT coil, as well as triggering many other lab devices.

Port B of the DIO-128 connects directly into the Transfer Control Circuit, used to control a series of electromagnets used in the magnetic transfer system, described in Chapter 3. The digital lines on this Port become the TTL lines responsible for turning on and off the individual coils used in the transfer sequence.

Port C of the DIO-128 connects to the 16 input lines of the 16-bit Digital-to-Analog Converter (DAC), described in the subsequent section.

Port D of the DIO-128 connects to Breakout Box B, visible on the equipment rack. This Port is responsible for turning on and off additional devices in our lab.

The DIO-128 runs on an internal clock at 100 MHz, and is capable of producing timing events every 10 ns. Because of its stability, we use the DIO-128 as the master clock in our laboratory. The DIO-128 outputs a square wave at 10 MHz which is synchronized to its internal clock. We use this clock output as the external clock reference for the analog output board, as well as the two SRS function generators used in the transfer sequence, described in Section 3.3.4. By doing this, we have synchronized all the timing devices in our experiment to one master clock on the DIO-128, eliminating any possible mismatch or phase slip. An advantage of using this approach is that high-precision analog signals generated through a DAC can be

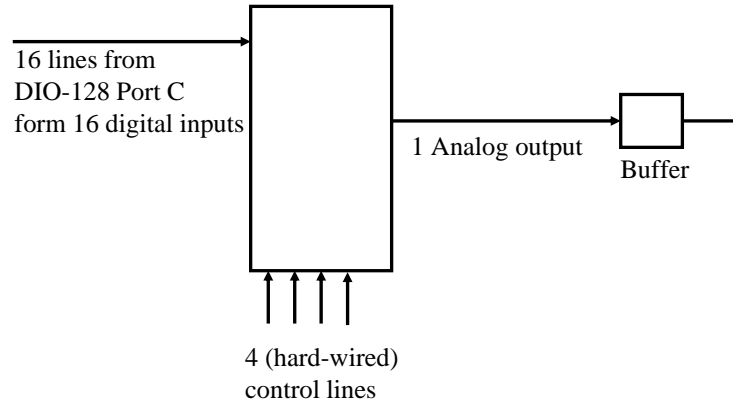


Figure 2.3: Schematic showing the Digital-to-Analog Converter (DAC) circuit. 16 digital lines from the DIO-128 are sent to the DAC chip, which provides one analog output, which is then sent through a unity-gain buffer.

synchronized precisely with the digital lines coming from the same board.

DAC

A 16-bit Digital-to-Analog Converter (DAC), Analog Devices AD7846JN, is used to generate a high-resolution analog signal from 16 digital lines on Port C of the DIO-128. This method of analog signal generation has the benefit of ensuring that the digitally derived analog signal is exactly synchronized with all the digital lines already being used. The DAC signal is used to control either the varying MOT coil current in the first stages of the transfer sequence or the DC TOP coils' current during the evaporation sequence. Figure 2.3 shows a schematic of the DAC circuit.

Analog input board

A NI PCI-6023E board is used for analog input. One channel on this board reads the voltage level on a photodiode monitoring the MOT fluorescence and proceeds with the rest of the timing sequence only when a certain voltage has been reached.

This ensures that we start out with the same number of atoms in the MOT for every run of the experiment, which helps to maintain greater repeatability in BEC production.

Analog output board

A NI PCI-6713 analog output board is used to control the devices that need to vary continuously in the MOT and CMOT portion of the sequence, such as the cooling beam intensity and detuning, and the repump beam intensity. The analog output board is not fully isolated from lab ground like the DIO-128 board is, however, a differential amplifier is placed along each line to separate computer ground from lab ground by $240\text{ k}\Omega$. The analog output board uses the 10 MHz clock reference signal from the DIO-128 board as an external timing reference, ensuring that the analog output from this board is synchronized with the digital board. One limitation of the analog output board is the finite buffer size, using the 10 MHz reference signal means that there is a 100 ns update rate in the analog output. Because of this limitation, we only use the analog output board for an analog output sequence of up to ~ 100 ms during the CMOT stage of the experiment.

2.3 Vacuum System

The vacuum chamber is the centerpiece around which the entire experiment is built. The vacuum system houses our source of atoms and provides a container with convenient access for optical and magnetic fields to interact with the atoms inside the chamber. The design of the vacuum system, in particular the background pressure and amount of optical access in different areas, will greatly effect what experiments

are realizable with a particular geometry.

We use a vacuum system that includes two glass cells separated by a linear distance of ~ 80 cm, comparably larger than many similar dual-chamber BEC experiments. The use of Rb dispensers, housed in the MOT cell, is a simple and reliable source of Rb atoms for our experiment that can easily produce MOTs of greater than $1 \cdot 10^9$ atoms. Although the number of atoms in a ^{87}Rb MOT with this source will likely be slightly smaller than that of a system using a Zeeman slower, dispensers are simple to use, particularly with glass vacuum cells. A description of the number of atoms trappable in a vapor-cell MOT based on the volume and background pressure of the vacuum chamber was discussed by Monroe *et al.* in 1990 [29].

We have chosen to use a dual-chamber, single-MOT design that requires magnetic transfer of trapped atoms from the MOT cell to a lower-pressure science cell. A significant advantage afforded by a single-MOT design over a dual-MOT design is the increased optical access afforded by the lack of laser cooling beams around the much smaller science cell. It is easy to put small magnet coils outside of the science cell that are efficient, unobstructive, and easily cooled.

The vacuum system and adjoining components of the experiment are shown in different ways in Figures 2.4, 2.5, and 2.6. A diagram showing a top-down view of the vacuum system is shown in Figure 2.4. This is a not-to-scale diagram that highlights all the important parts of the vacuum system in a pictorial representation. A side-view photograph of the vacuum system prior to the attachment of the two glass cells is shown in Figure 2.5. Figure 2.5 was taken after a preparatory bake of the vacuum system (described below) and does not show the two glass cells. Another

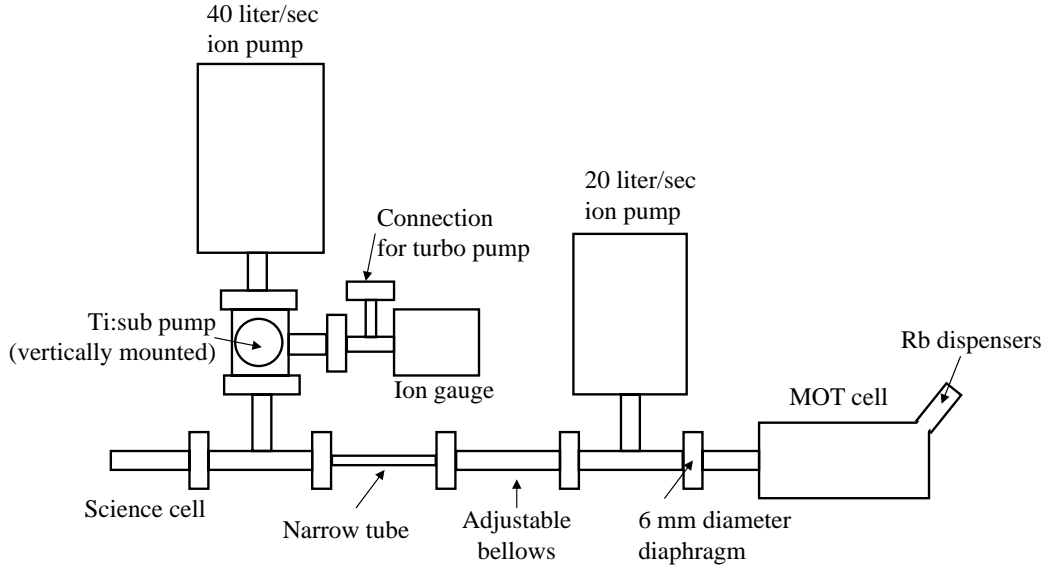


Figure 2.4: Schematic showing a top-down view of the vacuum system and glass cells (not to scale). Illustrated here is the second iteration of our chamber, which differs from the first in the position of the 40 l/s ion pump and the addition of an ion gauge.

angled side view of the vacuum system is shown in the two photographs of Figure 2.6. Figure 2.6 (a) is a photograph of the vacuum system and adjoining experimental apparatus taken after the bake, but before the installation of the magnetic transfer coils. The science cell, MOT cell, and optics used for the MOT are clearly visible. Figure 2.6 (b) is a photograph of the same apparatus after the addition of the magnetic transfer coils. The TOP trap is still absent from the picture, and the science cell is visible.

2.3.1 Design of a dual-chamber system

The design of our differentially pumped vacuum system incorporates two glass cells, a MOT cell and a science cell, with a linear distance of 76.2 cm between the location

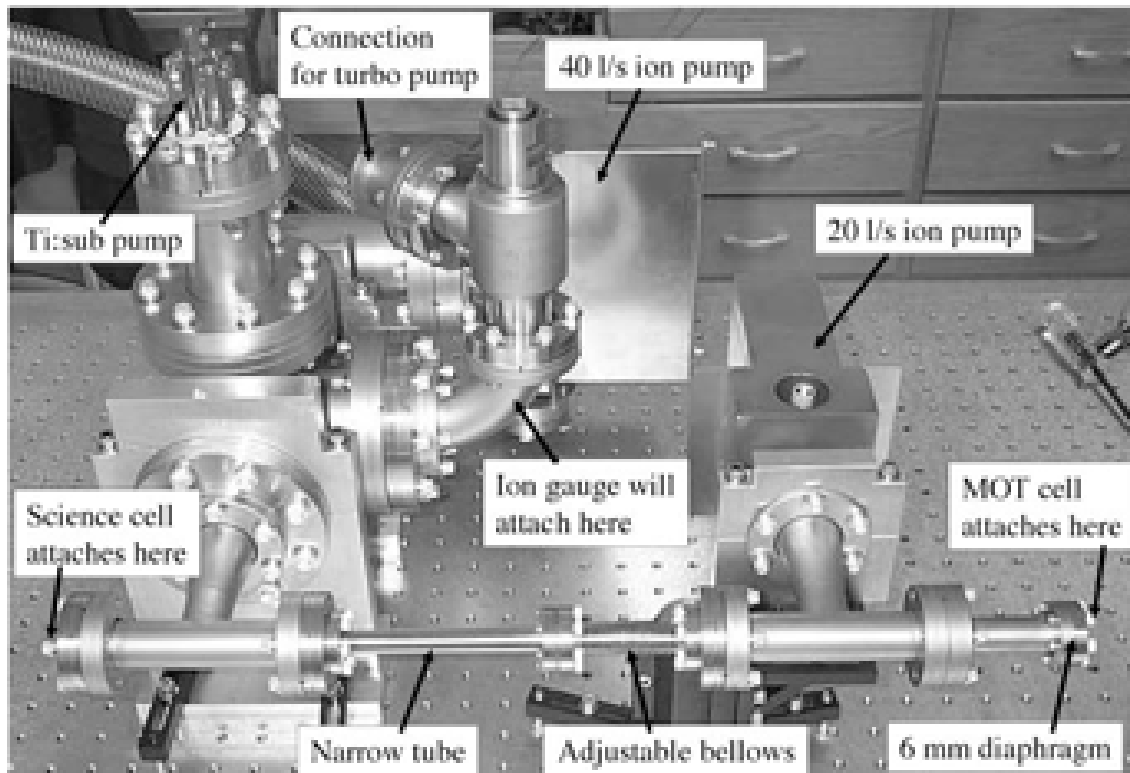


Figure 2.5: Photograph of the vacuum system (first iteration), taken after assembly of components but *without* the glass cells in place. The 4 electrical connections to the 4 titanium:sublimation pumps are visible in the upper left-hand corner. The magnets that attach to both the 40 l/s and 20 l/s ion pump have not been attached. The ion gauge (added in the second iteration) is attached at the position shown.

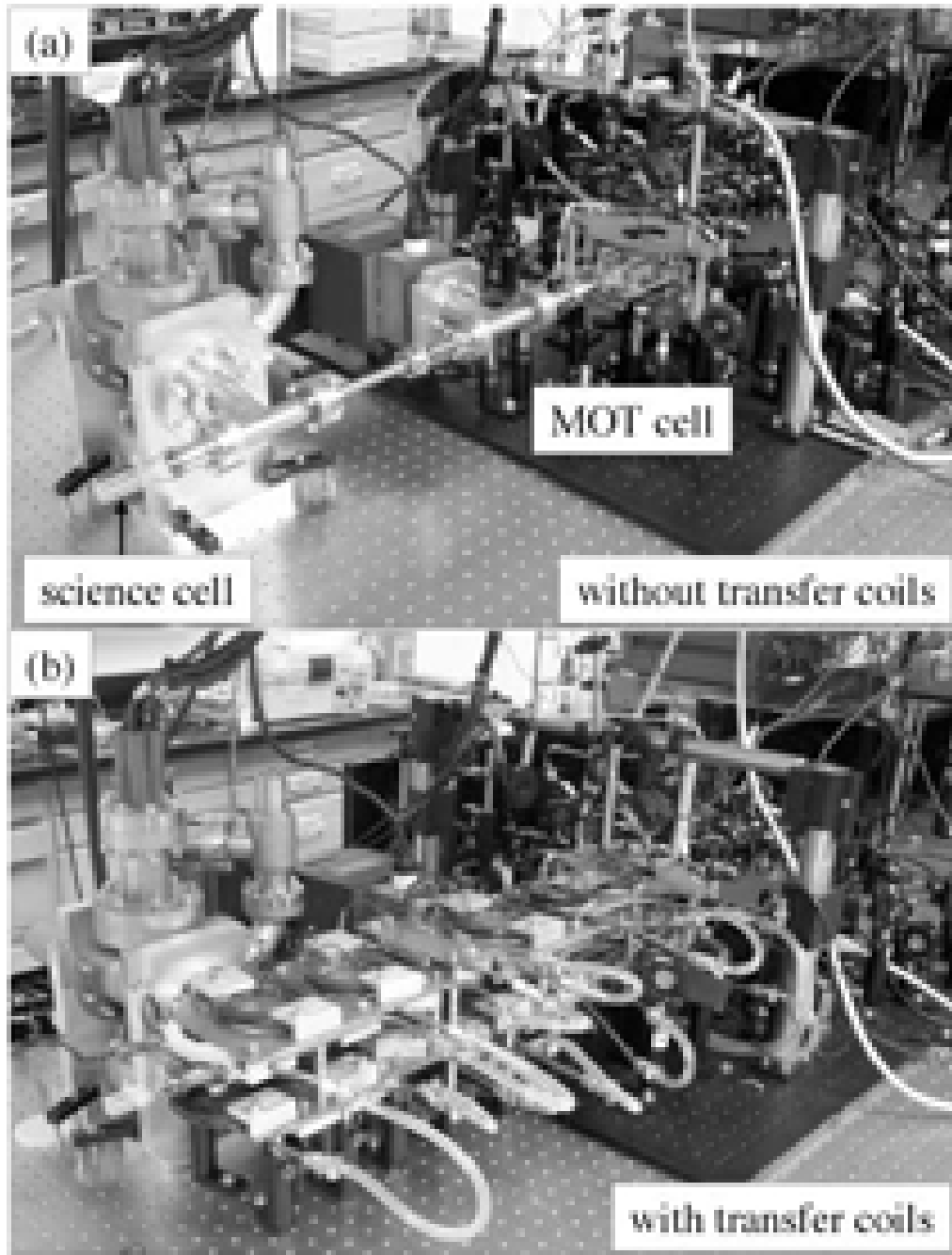


Figure 2.6: Photographs of the vacuum system (first iteration) with and without the magnetic transfer coils. (a) The system before the installation of the magnetic transfer coils. The science cell and MOT cell are indicated. The connections to the titanium:sublimation pump and the magnets used in the ion pumps, not visible in Figure 2.5, are shown. (b) The system after the installation of the magnetic transfer coils. The TOP trap coils are not in place.

of the MOT and the location of the BEC. The two glass cells allow for optical access into these two different regions of the chamber that have vastly different pressure and size requirements. The MOT requires a large glass cell so that one can use large laser cooling beams for optimum capture volume, and will operate at a higher pressure due to the Rb dispensers, which are housed in the MOT cell. In our approach, formation of the BEC requires a long vacuum-limited magnetic trap lifetime in the science cell, which dictates that the pressure in the science cell needs to be very low, preferably in the 10^{-12} torr range. We achieve this pressure difference by using a larger ion pump and a titanium:sublimation pump near the science cell and limiting the vacuum conductance from the MOT cell into the rest of the chamber.

The MOT cell is a $4'' \times 2'' \times 2''$ rectangular glass cell that also houses our source of Rb, 4 SAES Rb dispensers. Since August 2005, only one of these, the yellow dispenser, has been used. The MOT cell was custom constructed by Ron Bihler of Technical Glass in Aurora, Colorado¹. The MOT is connected to the main chamber by a 6 mm diameter diaphragm (highlighted in Figure 2.5) that has the effect of limiting the vacuum conductance between the MOT cell and the rest of the chamber. The MOT cell is pumped by a Physical Electronics² 20 liter/sec ion pump on the other side of this diaphragm. The ‘transfer tube’ consists of the tubes in between the MOT cell and the science cell, and has a limiting inner diameter of 1 cm at its narrowest region and is ~ 70 cm long. The science cell is a rectangular glass fluorimetry cell of $12\text{ mm} \times 12\text{ mm}$ outer area that is ~ 55 mm long and has a glass thickness of 1 mm. The glass science cell is connected to a stainless steel flange using a composite alloy in which the thermal expansion coefficient between the

¹website: <http://www.techglass.com>

²Now Gamma Vacuum; website: <http://www.gammavacuum.com/>

glass and steel varies continuously. The fluorimetry cell was attached to a standard glass/metal adapter by Ron Bihler.

The science cell is pumped by a titanium sublimation (ti:sub) pump that is vertically mounted in a standard 4.5" 5-port cross connected to the transfer tube. This structure houses 4 titanium filaments vertically within the cross. Also attached to the cross is a Physical Electronics 40 liter/second ion pump, a Varian model UHV-24 ion gauge (not shown in Figures 2.5 and 2.6), and a valve used for rough pumping with a Varian Turbo-V70 turbo pump. The ion gauge outgasses into the system and causes a temporary increase in pressure and is used only rarely, after baking the system or to diagnose a problem, but is the most reliable measure of the pressure in the chamber during baking. The ti:sub pumps are also used only rarely; they are degassed during the baking process and used daily, occasionally, and then rarely in the subsequent days and weeks after a bake. In normal, everyday operation, the only things pumping on the system are the two ion pumps and a layer of titanium deposited on the inner walls of the 5-port cross. The ion pump controller normally displays a value of $1 \cdot 10^{-10}$ torr as the pressure in the region of both ion pumps; however, this is the lower limit of the built-in gauge on these pumps and is not an accurate reflection of the pressure of the chamber.

We estimate that the pressure in the MOT cell is $\sim 5 \cdot 10^{-9}$ torr, but this is difficult to measure because there are no accurate gauges in the MOT cell. An estimate of the pressure in the science cell can be inferred from the reading on the ion gauge nearby. Pressures as low as $2 \cdot 10^{-12}$ have been recorded on the ion gauge before it reaches its lower limit, and we estimate that the pressure in the science cell is within this range. What we are most concerned about is not the pressure reading,

but the background-limited lifetime of atoms held in a magnetic trap. In the science cell, we have measured the background-limited lifetime of thermal atoms held in a quadrupole trap to be as long as eight minutes.

There are 4 Rb dispensers mounted to the MOT glass cell, each of which contains enough Rb for several years of experiments. We are currently working with the yellow dispenser and turn it on each morning to 3.4 A and leave it on for the day, but turn it off at night and while we are not working on the experiment.

Our dual-chamber vacuum system satisfies the design requirements of having a large MOT cell containing the source of Rb atoms, separation of the higher-pressure MOT cell from the main chamber by limiting the vacuum conductance, and having a small, lower-pressure science cell that allows for convenient optical and magnetic access. One difficulty of our design is the requirement that we transfer atoms collected in the MOT cell to the science cell, which we do by operating a series of overlapping magnet coils. The complexity of this magnetic transfer apparatus is described in Chapter 3.

2.3.2 Vacuum system construction and baking

The purpose of this section is to describe the ideal complete procedure we would use for preparation and baking of a vacuum system containing glass cells for use in ultra-high vacuum (UHV) situations. The following sections describe (1) the preparation for baking; (2) the initial all-metal bake; and (3) the final bake of the chamber including the glass cells. This section is written in the hope that it will be usable by another research group that is preparing a vacuum system similar to ours. In practice, the timeline of events that we actually followed differed slightly

from the recipe below. These differences will be discussed in the final portion of this section.

Preparation for baking

The preparation of components that are as clean as possible is a necessary first step in setting up a vacuum system to be used as a UHV chamber [21, 30]. Our procedure starts with cleaning all the stainless steel components, copper gaskets, and flanges with deionized water to remove oils. After this, all the components are placed in a 45-minute ultrasonic bath with deionized water and Cole-Parmer Micro-90 concentrated cleaning solution. The components were then rinsed with deionized water. All the components then undergo another ultrasonic bath with acetone; and finally, an ultrasonic bath with methanol. At this point the components are considered clean enough to use and are handled only with powder-free latex gloves and stored in an enclosed wrapping of oil-free aluminum foil.

For the initial all-metal bake, all the stainless steel components, including the ti:sub pump and ion pumps (with magnets off), are assembled and the chamber is mounted to the optical table. Stainless steel blanks are placed at the locations where the two glass cells will later attach. Figure 2.5 shows what the system looks like at this point in the procedure.

In preparation for baking, oil-free aluminum foil is placed over the entire system to provide better heat distribution and to minimize burning from the heater tape at hot-spots. Eight heater tapes are carefully wrapped around different parts of the system. Eight thermocouples are placed in various locations to record the temperatures of different parts of the vacuum chamber. The entire system is wrapped

repeatedly in aluminum foil to create an ‘oven’ that will keep the heat trapped inside.

Initial all-metal bake

The aim of the initial bake is to remove any impurities that exist on the insides of the metal components that make up the vacuum chamber. This is accomplished by bringing the system up to a very high temperature while pumping with the turbo pump for several days. After assembly of all the vacuum components, the turbo pump was attached to the system and it began pumping for the entire bake. The following is a timeline of the 8-day baking schedule:

Day 1 (5/26/2005) The temperature of the entire system was brought up slowly to an average temperature of ~ 300 °C over the course of the day. By the end of the day, the ion gauge read a pressure of $1.3 \cdot 10^{-6}$ torr.

Day 2 (5/27/2005) On this day, the temperature of the entire system was increased slightly, to an average temperature of ~ 325 °C. By the end of the day, the ion gauge read a pressure of $9.0 \cdot 10^{-7}$ torr.

Days 3-7 (5/28/05)-(6/1/2005) Over the course of these five days, the temperature remained constant and the pressure dropped from $3.3 \cdot 10^{-7}$ torr on the third day to $1.2 \cdot 10^{-7}$ torr on the seventh day.

Day 8 (6/2/2005) The temperature of the system was slowly decreased to room temperature over the course of the day. By the end of the day, the pressure had dropped to $1.5 \cdot 10^{-8}$ torr. The valve to the turbo pump was closed and the turbo pump was turned off. This concluded the bake.

The magnets on both ion pumps were attached, and on the subsequent day (6/3/2005), the large ion pump reported the lowest pressure it can record, $1.0 \cdot 10^{-10}$ torr. Because this was the first time that we used the Varian UHV-24 ion gauge, it initially caused a large amount of outgassing into the chamber and caused the pressure indicator on the ion pump to temporarily increase. After repeated outgassing of the ion gauge and running it continuously for 30 hours, the ion gauge reported a pressure of $1.3 \cdot 10^{-10}$ torr by 6/9/2005.

Final bake

The aim of the final bake is to prepare the entire system (including the glass cells, Rb dispensers, and ti:sub pump) for use as a UHV vacuum chamber. This involved the addition of the two glass cells and another 7-day bake that included degassing both the Rb dispensers and the ti:sub pump filaments.

When baking a vacuum chamber that includes both glass and metal components, it is essential to keep the temperatures on either side of the glass/metal interfaces as close to each other as possible because these materials have different thermal expansion coefficients. Also, glass cannot be brought up to as high of a temperature as the stainless steel components. It is possible to do the entire vacuum preparation procedure in only one bake, but we felt that the preceding factors made an initial high temperature all-metal bake more satisfactory.

To prepare the chamber for baking, the glass cells must be attached to the rest of the chamber, which requires bringing the entire vacuum system up to atmospheric pressure. To accomplish this, the ion pumps were turned off and the magnets on the ion pumps were removed. Then, the valve that connects the turbo pump to the

vacuum system was slowly opened (with the turbo pump turned off) to allow the system to come up to atmospheric pressure. During this entire process, dry nitrogen was flowing into the vacuum system through a source connected on the turbo pump side of the valve. This ensured that the major pollutant in the chamber would be N_2 , which is easily removed by our pumps. With N_2 flowing into the chamber and the system at atmospheric pressure, a blank was removed and replaced with the glass MOT cell. The entire time, N_2 was flowing into the system so that it would act to push out any impurities through the hole left where the MOT cell attaches. The same steps were repeated for insertion of the glass science cell. In both cases, the time involved in between removal of a blank and insertion of the glass cell was less than a minute, minimizing contact between the inside of the vacuum chamber and non- N_2 atmosphere.

Two additional glass heater tapes were placed around the two glass cells, and ten thermocouples were used to record the temperatures at various locations of the vacuum chamber. To commence baking, the flow of N_2 was stopped, the valve was sealed, and the turbo pump was turned on for the duration of the bake. The following is a timeline of the remaining 7-day baking schedule:

Day 1 (8/9/2005) The temperature of the entire system was brought up slowly to an average temperature of ~ 200 °C over the course of the day. By the end of the day, the ion gauge read a pressure of $1.8 \cdot 10^{-8}$ torr. On this day, the ti:sub pump degas routine was started. The ti:sub pump consists of 4 filaments, filament #1, having been used from 2001 to 2005, has not been used at all after the summer of 2005. Since then, filament #2 has been used predominantly as the main sublimation pump, and filaments 3 and 4 were also degassed. The

ti:sub pump degas routine consists of running each filament (#2, 3, and 4) at 30 A for 2 minutes, then 40 A for 2 minutes, then 45 A for 2 minutes, then 50 A for 2 minutes, then 50 A again for 2 minutes. This degas procedure was repeated on later days. The Rb dispensers were also degassed by running each of the 4 dispensers at 6 A for 15 seconds, then at 5 A for 15 seconds. The dispensers get visibly red-hot when running a current of 6 A for only a few seconds, indicating that they are clearly hot enough to be dispensing Rb and other adsorbed materials into the chamber. All 4 Rb dispensers were then left on at 3 A for the entire duration of the bake.

Day 2 (8/10/2005) The temperatures remained constant. The ti:sub pump and Rb dispensers were degassed according to the above procedure.

Day 3 (8/11/2005) The temperatures remained constant and the ti:sub pump and Rb dispensers were degassed. By the end of the day, the ion gauge read a pressure of $5.7 \cdot 10^{-8}$ torr.

Day 4 (8/12/2005) The temperatures remained constant everywhere except for the two ion pumps. The temperatures on these were brought down slowly to room temperature over several hours and the aluminum foil was removed in order to attach the magnets to the ion pumps. With the two magnets attached, both ion pumps, as well as the turbo pump, were now pumping on the system. At this point, the ion gauge read a pressure of $4.4 \cdot 10^{-8}$ torr. The ti:sub pump and Rb dispensers were degassed. Then, ti:sub filament #2 was turned on to 25 A and left on continuously for the duration of the bake.

Day 5 (8/13/2005) Temperatures were held constant, the ti:sub pump was degassed, and all dispensers were degassed at 5 A for 30 sec. By the end of the day, the ion gauge read $2 \cdot 10^{-8}$ torr.

Day 6 (8/14/2005) Temperatures were held constant, the ti:sub pump was degassed, and all dispensers were degassed at 5 A for 30 sec. By the end of the day, the ion gauge read $2.3 \cdot 10^{-8}$ torr. Ti:sub filament #2 was still left running at 25 A.

Day 7 (8/15/2005) Ti:sub pumps #2, 3, and 4 were degassed at 40 A for 2 minutes, then ti:sub pump #2 was degassed at 45 A for 2 minutes. All temperatures in the system were brought down slowly over the course of the day, and by the end of the day the aluminum foil could be removed and the system was near room temperature. The valve to the turbo pump was closed and the turbo pump was turned off. This concluded the bake.

If we were to build a new vacuum chamber from scratch, we would follow the 2-bake procedure above. However, if our current vacuum system were exposed to atmospheric pressure for a short period of time, it would probably only be necessary to perform the second, ‘final’ bake as described above.

What actually happened

What has actually occurred over the history of our lab differs slightly from the above recipe. When the lab was initially set up in 2001, two bakes, similar to the ones described above, were performed. In April 2005, after working with smaller than expected MOTs and failed attempts at making a BEC, we discovered that there was

significantly more K than Rb in our vacuum chamber. We had originally designed our system to have three Rb and three K dispensers, in the hope of doing experiments with both atoms. For some unknown (and still baffling) reason, the K from each of the six dispensers was much more plentiful after 4 years. The abundance of K in the chamber was not originally checked and compared with Rb when we first set up the experiment. We suspect that all the dispensers were actually K dispensers, but were ‘contaminated’ with a small amount of Rb, enough to make small Rb MOTs, consistent with our observations. This kind of ‘cross-contamination’ with residual amounts of other alkali atoms is not unusual for these kinds of dispensers.

A decision was made to replace the MOT cell with a new cell containing only four Rb dispensers, and we prepared to perform two bakes as described above. The first bake occurred from 5/26/2005 through 6/2/2005 and is described exactly above. The second bake, which included both glass cells, occurred from 6/10/2005 through 6/16/2005 and was very similar to the ‘final bake’ described above. However, after this second bake, a vacuum leak was created by accidentally breaking off one of the Rb dispensers’ electrical leads. Vacuum sealant was not able to fix the leak. The cell had to be removed and returned to Ron Bihler, who closed the leak. After re-installing the cell, we performed a third bake with both glass cells in place, this bake occurred from 8/9/2005 through 8/15/2005 and is described exactly above.

A final scare occurred on the last day of this third bake, during the process of bringing the system back down to room temperature. Shortly after the system returned to room temperature, the ion gauge read a pressure of $6.2 \cdot 10^{-10}$ torr. At this point we began to suspect that things were awry, because at the corresponding point of the second bake the system had already come down to a pressure of $1 \cdot 10^{-11}$ torr.

We noticed that when both ion pumps were turned off, the pressure on the ion gauge jumped up to $\sim 10^{-7}$ torr in ~ 2 minutes, clearly a bad sign. We began looking for a leak by blowing dry N_2 into the chamber at all the seal locations, and noticed a small but observable increase in pressure when blowing N_2 into one of the dispenser leads. We applied VacSeal vacuum sealant to the probable location of the leak and the pressure began dropping immediately. After an hour and a couple of VacSeal applications, the pressure on the ion gauge had dropped to $7.3 \cdot 10^{-11}$ torr, the 40 l/s ion pump read $1.36 \cdot 10^{-10}$ torr, and the 20 l/s ion pump read $2.3 \cdot 10^{-9}$ torr.

By the next day (8/16/2005), the ion gauge was reporting pressures as low as $3 \cdot 10^{-12}$ torr before the device hit its lower limit and could no longer accurately record the pressure. After repeated degassing of the Rb dispensers, we were able to observe a small Rb MOT by the end of the day.

The size of the MOT grew steadily over the next few days. We transferred atoms into the science cell and achieved our first Bose-Einstein Condensate of ^{87}Rb atoms only one month after this bake, on 9/23/2005.

2.3.3 Vacuum system integrity test

Immediately following the final bake and daily for several weeks afterward we performed a vacuum system integrity test using the ion gauge. This was used as a diagnostic tool to see how well the ion pumps were able to pump down to low pressure, and as a check against any suspected vacuum leaks. During everyday operation the two ion pumps read a pressure of $1.0 \cdot 10^{-10}$ torr, the minimum pressure readable on the gauges, but in reality the pressure is much lower than that at the pumps. Because the built-in gauges on the ion pumps cannot record pressures below

$1.0 \cdot 10^{-10}$ torr, we need to use the ion gauge to determine the actual pressure in the vacuum chamber. After being turned on, the ion gauge will quickly decrease its reading to as low as $1.2 \cdot 10^{-12}$ torr before the device can no longer record the pressure. To perform the vacuum system integrity test, we turn off both ion pumps and record the pressure on the ion gauge every 15 seconds for 3 minutes, watching the pressure steadily rise. We then turn both ion pumps back on and record the pressure on the ion gauge every 15 seconds for 1-2 minutes afterward, watching the system pump down to lower pressures before the ion gauge bottoms out.

When the ion pumps are turned off, the eventual value and speed of increase in pressure yields information on the quality of the vacuum system and how well it can maintain low pressures without any pumping. When the ion pumps are turned back on, the rate of decrease in pressure tells us how well the ion pumps are able to perform at pulling the system back down to lower pressures. A plot of ion gauge reading vs. time for this test both immediately after the final bake and one week after it are shown in Figure 2.7. After the system had been pumped on for only a few days, the pressure only rose to 10^{-9} torr after 3 minutes, whereas on the final day of the last bake, before we had plugged the leak with VacSeal, the pressure rose to 10^{-7} torr after only 2 minutes.

2.4 Lasers

Our experiment uses four lasers to cool, manipulate, and probe ^{87}Rb atoms. The transition frequencies necessary for laser cooling of ^{87}Rb are shown in Figure 2.8, this and much more information on the ^{87}Rb D line transition can be found in the useful online resource paper written by Dan Steck [31].

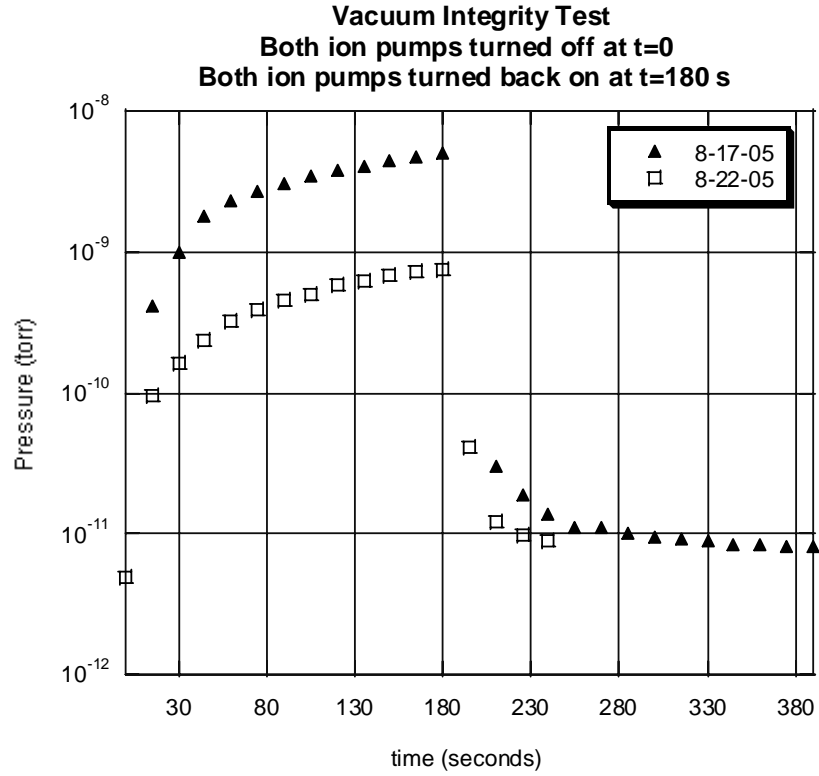


Figure 2.7: Vacuum integrity test. Semi-log plot of the ion gauge pressure [torr] vs. time [seconds]. Data taken on 8/17/2005, immediately after the bake, is shown in solid triangles. Data taken on 8/22/2005, one week after the bake, is shown in open squares. Both ion pumps were turned off at $t = 0$ s, and the pressure on the ion gauge began to rise immediately. At $t = 180$ s, both ion pumps were turned back on, the pressure jumped back down and continued to decrease over time. The eventual rise in pressure (at $t = 180$ s) on 8/22/2005, only 5 days after the original data, is almost an order of magnitude lower in pressure than it was on 8/17/2005.

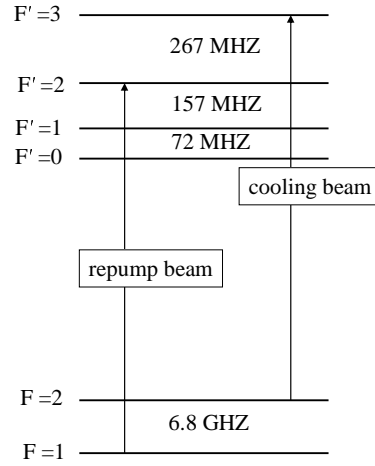


Figure 2.8: ^{87}Rb energy levels

The titanium:sapphire laser used for laser cooling ^{87}Rb atoms will be described in Section 2.4.1. Two home-made diode lasers are used in our experiment; the construction method used for our diode lasers is described in Section 2.4.2. The diode laser used as the repump beam will be described in Section 2.4.3, and the diode laser used as the probe beam will be described in Section 2.4.4. The diode laser used as a beam to create an optical potential in our experiment will be described in Section 5.4.3.

2.4.1 MBR laser and lock

The workhorse laser in our lab is the Coherent Monolithic Block Resonator MBR-110 continuous-wave titanium:sapphire ring laser, pumped by a Verdi V-10. This laser has a maximum output power of 1.5 W, is tunable over 600-1000 nm, and can be locked to an external frequency reference. The MBR laser is locked to a stabilized internal reference cavity; the external lock operates by making the internal reference

cavity mimic an external error signal. In our case, we generate an error signal based on a saturated absorption signal from a ^{87}Rb vapor cell, and the MBR laser locks to this error signal.

Other than the frequency tunability, the principal advantage of using the MBR laser is the large amount of output power in comparison to that of diode lasers; the MBR output is used as the laser cooling beam, and high power is helpful in loading a large MOT. At 780 nm, the MBR has an output of ~ 1.1 W, and after the output beam passes through an 80 MHz double-pass Acousto-optical Modulator (AOM) and a single-mode fiber we still have a total of 450 mW to use for the cooling beams. This laser system is not without its disadvantages; it is large and costly and requires periodic maintenance of the optics in the cavity and electronics in the feedback loops. A detailed description of many of the the optics and electronics problems and solutions associated with the MBR laser is given in Appendix A.

A schematic of the optics and electronics used to atomic lock the MBR laser is shown in Figure 2.9, with laser light shown as a solid line and electrical signals shown as dashed lines³. A small portion of the MBR output light is sent to the atomic laser lock (enclosed within a bold box in Figure 2.9), but the majority of the MBR output light is sent through the 80 MHz double-pass cooling AOM, operating at an upshift. Most of this light is sent to the MOT through the cooling beam fiber, but a small amount is sent to the BEC cell via the near-resonance probe fiber. The atomic laser lock is responsible for keeping the MBR laser in lock; this laser is used simultaneously as the laser cooling beam and a near-resonance probe beam for imaging the BEC.

³For additional information, see the lab notebook entry on 6/10/2004.

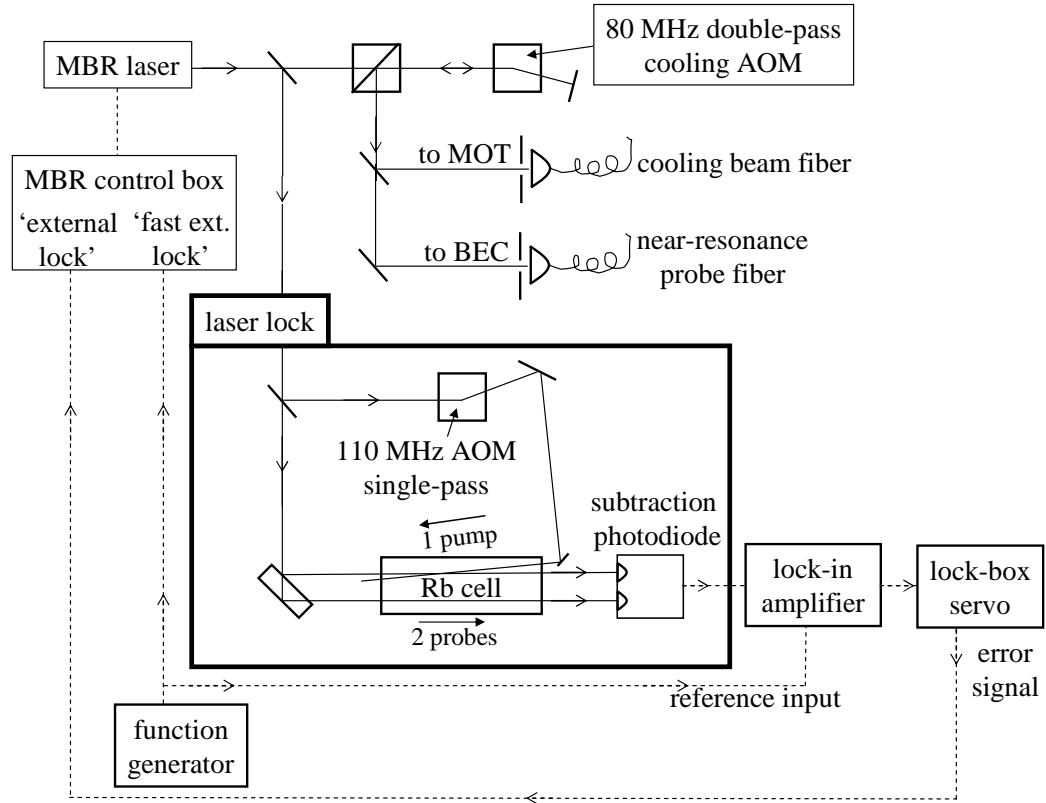


Figure 2.9: Optics and electronics used in the MBR laser lock. Laser light is shown as a solid line and electrical signals are shown as dashed lines. The atomic laser lock is the portion of the schematic enclosed in a bold box. The optical output of the entire apparatus is coupled into the cooling beam fiber and the near-resonance probe fiber. Both AOMs shown operate at an upshift. Mechanical shutters are placed before both optical fibers.

The portion of the light that enters the laser lock gets split into a pump beam and a probe beam using a beamsplitter. The pump beam passes through a single-pass 110 MHz AOM operating at an upshift. The probe beam deflects off a thick plate of plexiglass which provides reflections from both the front and back surfaces, producing two copropagating probe beams that are spatially separated by ~ 4 mm. One of these probe beams interacts with the counter-propagating pump beam in the Rb vapor cell and provides a saturated absorption signal to one of the photodiodes. The other probe beam simply passes through the Rb vapor cell and provides a background Doppler absorption signal.

The signals from the two probe beams in the laser lock get subtracted in the photodiode subtraction circuit [32, 33, 34, 35, 36]; this results in a signal consisting of only the saturated absorption dips. The derivative of this signal is used as the error signal that is applied as feedback to the MBR laser. We differentiate this signal using a lock-in amplifier and function generator. A function generator outputs a sine wave signal at 70 kHz, which provides the modulation that we ‘lock to’ using the lock-in amplifier. This signal inputs into the ‘fast external lock’ input on the MBR control box and directly modulates⁴ the tweeter mirror, mirror M3 of the MBR cavity. The 70 kHz signal is applied both to the MBR control box and to the ‘reference input’ of the lock-in amplifier. The output of the photodiode subtraction circuit is applied to the ‘signal input’ of the lock-in amplifier. The output of the lock-in amplifier will then be a differentiated version of the saturation absorption dips.

⁴This provides a small amount of Frequency Modulation (FM) to the lasing frequency of the MBR laser. The amount of FM is so small that it does not affect our ability to use this laser for the purposes of laser cooling and absorption imaging.

We lock to the crossover dip between the $|F = 2 \rightarrow F' = 2\rangle$ transition and the $|F = 2 \rightarrow F' = 3\rangle$ transition. We use the lock-in output as the error signal that is sent to the ‘lock-box servo’ electronics box. After an appropriate adjustment of the amplitude and offset, this box is responsible for switching on the laser lock by feeding the error signal back to the ‘external lock’ input on the MBR control box. This forces the internal reference cavity of the MBR laser to mimic the error signal coming from the lock-box servo, and locks the laser to the atomic reference.

We have found that using single-mode, polarization maintaining optical fibers to couple light from the lasers to the experiment is a good way of providing a stable, clean beam. Any optical misalignments that occur can usually be fixed by simply optimizing the fiber alignment, and using a single-mode fiber is an excellent way of generating a beam with high mode quality.

2.4.2 Diode laser construction

Two diode lasers have been constructed using a home-made design⁵ and are used as the repump laser and probe laser. The design is a modified version of the Littrow configuration design [37, 38]. A top-down photograph of a diode laser box is shown in Figure 2.10.

The diode laser itself is a Sharp GH0781JA2C 120 mW diode laser, which typically has a free-running wavelength of 784 nm. An external feedback cavity employing an Edmund Optics model 43774 holographic grating is mounted on a Thorlabs Piezo-Electric Transducer (PZT). The laser and external grating are mounted on a modified Newport Ultima U100-P kinematic mirror mount. The laser beam de-

⁵For additional information, see the lab notebook entry on 5/22/2002.

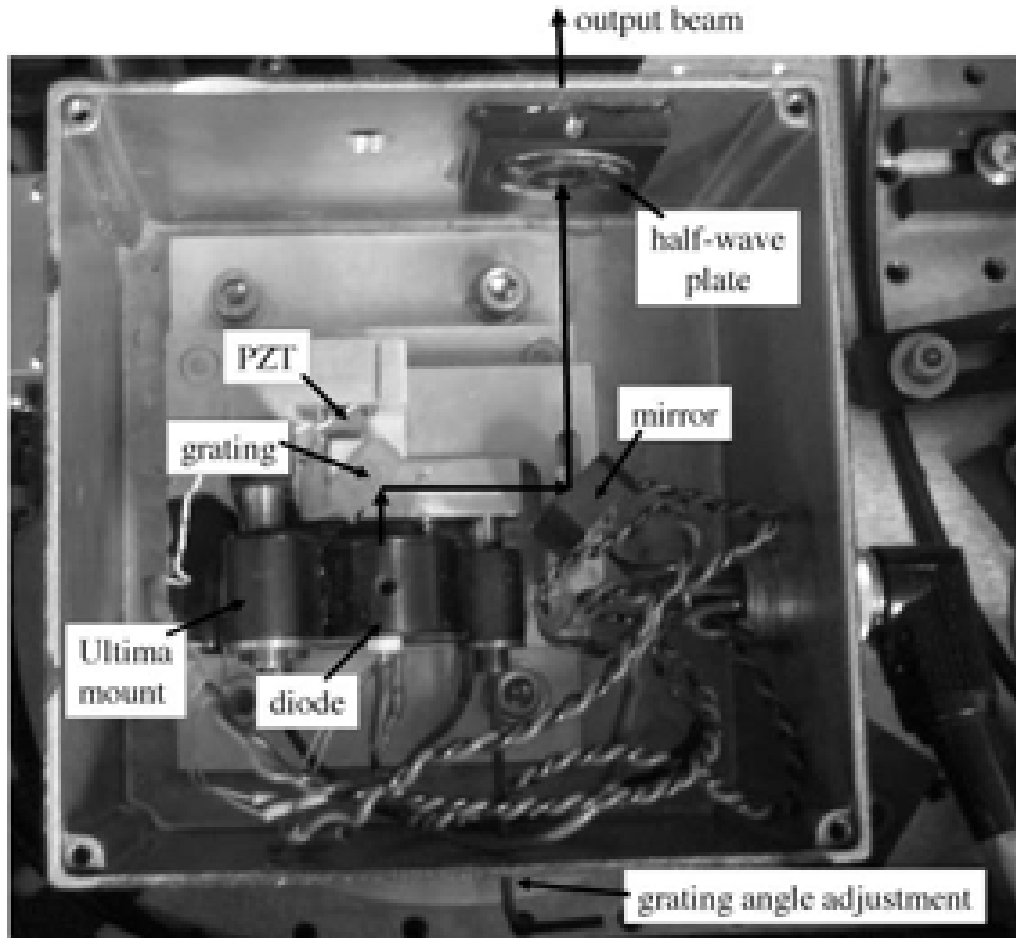


Figure 2.10: Top-down photograph of a diode laser box, showing all the components in the box and the beam path highlighted in black arrows. The laser diode itself is housed within a black Newport Ultima mount, to which is attached an aluminum plate. The grating is glued onto a 45° wedge that is glued onto the PZT; the PZT is glued onto the aluminum plate. The aluminum plate also holds the mirror which deflects the output beam after the grating. The output beam then passes through a half-wave plate before it exits the diode laser box. The thermistor (not visible from the top) is connected to the Ultima mount, very close to the diode laser. The TEC (also not visible) is placed under a different aluminum plate under the Ultima mount. A removable allen key can access the horizontal angle adjustment of the Ultima mount to change the grating angle. The entire box sits on top of a large heat sink.

flects off the grating and an external mirror in such a way that adjustment of the grating angle does not cause a change in the output beam angle. There is a small translational shift in the output beam position, but this is usually negligible. The Ultima mount is placed on top of a Thermo-Electric Cooler (TEC), which sits on top of a large heat sink. Using the TEC, we cool the temperature of the aluminum mount (and hence the laser diode) to approximately 16 °C. We have found that it is essential to place the thermistor as close to the diode laser as possible to prevent oscillations of the temperature controller. Temperature cooling is necessary in order to shift the laser's operating wavelength closer to 780 nm; external grating adjustment is necessary in order to fine-tune the laser to be in resonance with ^{87}Rb . The entire unit is housed within a box to prevent fluctuations due to air currents. There are small holes in the box to allow for light output and external grating adjustment. After leaving the diode laser box, the output beam passes through an anamorphic prism pair to correct the aspect ratio of the beam. The beam then passes through an Optics For Research OFR IO-3C-781VLP optical isolator that prevents optical feedback from returning to the diode laser.

2.4.3 Repump laser and lock

The repump laser is tuned to be in resonance with the $|F = 1 \rightarrow F' = 2\rangle$ transition and is used to optically pump atoms out of $|F = 1\rangle$ and into $|F = 2\rangle$. The repump laser is used while creating a MOT and for pumping atoms into $|F = 2\rangle$ in order to image the BEC using absorption imaging. The repump laser is locked to an atomic transition using a saturated absorption scheme⁶ similar to that of the MBR laser,

⁶For additional information, see the lab notebook entry on 12/1/2005.

shown in Figure 2.11.

A small portion of the repump beam is sent to the laser lock using a beamsplitter. Just like in the MBR lock, a plexiglass plate is used to pick off two probe beams; the transmitted beam becomes the pump beam in this laser lock. The two probe beams pass through the Rb vapor cell and onto the two photodiodes of the subtraction photodiode. The pump beam passes through a double-pass 80 MHz AOM operating at a downshift and then through the Rb vapor cell in the opposite direction of one of the counter-propagating probe beams. Just like in the MBR lock, one of the probe beams interacts with the counter-propagating pump beam and produces the saturated absorption dips, and the solitary probe beam provides a background Doppler signal.

By changing the frequency of this 80 MHz double-pass AOM (i.e. by changing it from 80 MHz to 77 MHz), the frequency of the pump beam relative to the two probe beams changes; this shifts the location of the saturated absorption dips in frequency space. We dither the frequency of this 80 MHz double-pass AOM using a function generator operating at 35 kHz. We change the *frequency* of the pump beam by changing the operating frequency of the AOM by a few MHz, but the light output will also be *frequency-modulated* by a small amount at a *rate* of 35 kHz. This produces a small amount of FM on the pump beam, which dithers the location of the saturated absorption dips by an amount detectable using the lock-in amplifier. When using a scheme like this it is helpful to modulate the pump beam, rather than the probe beam; otherwise one will also provide a small amount of Amplitude Modulation (AM) onto the photodiode signal, which could hinder the operation of the lock-in scheme.

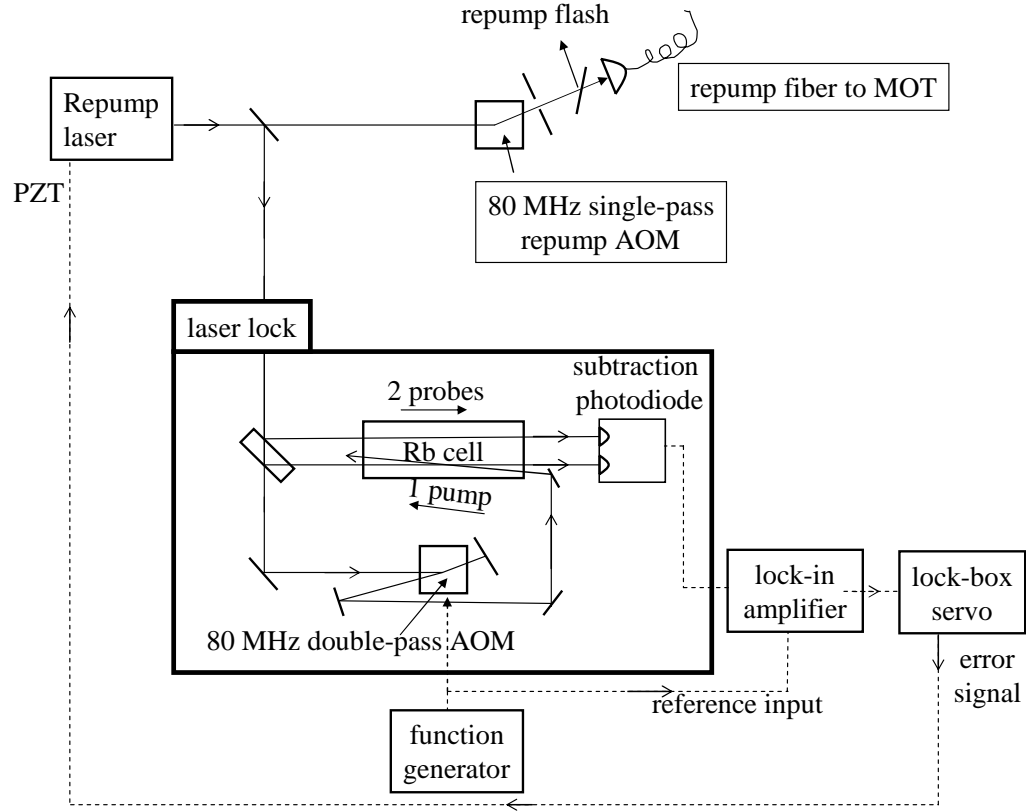


Figure 2.11: Optics and electronics used in the repump laser lock. Laser light is shown as a solid line and electrical signals are shown as dashed lines. The atomic laser lock is the portion of the schematic enclosed in a bold box. Most of the optical output of the entire system goes to the repump fiber, to be sent to the MOT as the repump beam. A small portion of light gets picked off before this fiber and is sent to the science cell as the repump flash beam, these two beams operate on the same AOM and mechanical shutter. Both AOMs shown operate at a downshift.

The lock-in amplifier’s output is a differentiated version of the saturated absorption dips, and is sent to the lock-box servo. The output of the lock-box servo, after an appropriate scaling and offset adjustment, is used as the error signal that is fed back to the PZT of the repump laser to stabilize its frequency.

Most of the light from the repump laser is sent through an 80 MHz single-pass AOM operating at a downshift, a mechanical shutter, and a single-mode fiber before being sent to the MOT cell. This AOM allows for fast switching and also provides an amplitude adjustment for the repump beam, which is necessary in the CMOT stage of the experiment. After the shutter, a small portion of the beam is picked off and sent to the science cell, to be used as the ‘repump flash’ to optically pump atoms into $|F = 2\rangle$ in the science cell.

2.4.4 Probe laser and lock

A probe laser⁷ used specifically for phase-contrast imaging of the BEC was constructed using an identical design as the repump laser. This far-off-resonance probe beam is used to image the trapped atoms in the science cell; this laser is typically 800 MHz red-detuned from the $|F = 1 \rightarrow F' = 2\rangle$ transition. This laser is locked to an atomic transition using a Dichroic Atomic Vapor Laser Lock (DAVLL) [39]; a schematic of the laser lock is shown in Figure 2.12.

Most of the probe laser output light passes through a 125 MHz single-pass AOM operating at a downshift, a mechanical shutter, and a single-mode optical fiber to be used to image the BEC in the science cell. The portion of the light used in the DAVLL lock first passes through a half-wave plate. Rotation of this half-wave

⁷For additional information, see Tim McComb’s lab notebook entry on 4/1/2005.

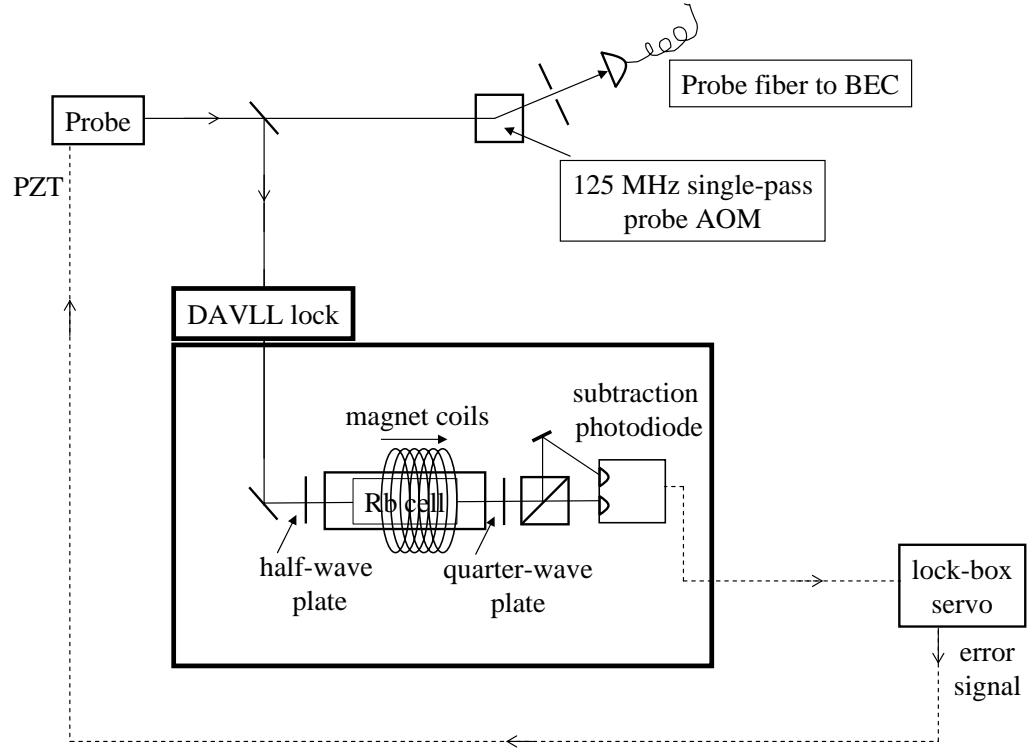


Figure 2.12: Optics and electronics used in the probe laser lock. Laser light is shown as a solid line and electrical signals are shown as dashed lines. The DAVLL laser lock is the portion of the schematic enclosed in a bold box. The optical output of the entire apparatus is sent to the probe fiber to be used for imaging the BEC. A mechanical shutter is placed before the optical fiber. The AOM operates at a downshift.

plate changes the polarization angle of the beam while keeping it linearly polarized. This linearly polarized beam can be thought of as a combination of σ^+ and σ^- polarizations. The DAVLL lock requires a large uniform magnetic field inside the Rb vapor cell. This provides different Zeeman shifts to the atoms interacting with the σ^+ and σ^- components of the beam. We create this magnetic field by wrapping magnet wire around the 1" outer diameter Rb glass vapor cell. We achieve a uniform magnetic field of approximately 100 G inside the vapor cell by running 3 A through the magnet coils. After the vapor cell, the beam passes through a quarter-wave plate, which maps the σ^+ and σ^- components of the beam onto horizontal and vertical linear polarizations. Finally, a polarizing beamsplitter cube separates these horizontal and vertical components and sends them onto two different photodiodes. These signals are subtracted in the photodiode subtraction circuit, and sent to the lock-box servo, which atomic locks the probe laser by applying feedback to the PZT.

A major advantage of using the DAVLL lock is the simplicity of the optical setup, the laser lock does not require any AOMs or lock-in amplifiers and uses a minimum of components. The lock is also easily tunable over a very wide frequency range; we have made measurements using phase-contrast imaging at detunings of -1000 MHz to $+800$ MHz. The major drawback in our implementation of this locking scheme, however, is that the laser is more susceptible to small frequency drifts over the course of the day. This is a technical problem associated with our experimental setup, and it not fundamental to the DAVLL technique.

2.5 MOT

Loading the Magneto-Optical Trap (MOT) is the first stage in a series of sequential steps that we use to create a BEC. This first step collects, cools, and traps atoms from a room-temperature vapor in the MOT cell. Efficient preparation of a large number of trapped atoms at low temperatures sets the stage for the next two major steps in the sequence: transferring the cloud of atoms into the lower-pressure science cell, and then evaporatively cooling the cloud to BEC. The MOT, Compressed MOT (CMOT), and optical pumping stages, which all occur in the MOT cell, play a crucial role in preparation of the cloud in order to optimize the number of atoms in the eventual BEC. Several review articles and books have discussed the general principles underlying laser cooling and trapping [40, 41, 42]; the original MOT was described by Raab *et al.* in 1987 [43]; and a description of achievable MOT size vs. cooling beam parameters was discussed by Gibble *et al.* in 1992 [44].

2.5.1 Magneto-optical trapping using diverging beams

Our MOT differs from a conventional vapor cell MOT in that we use diverging beams as the laser cooling beams, rather than collimated beams. It is more common to use large collimated beams as the cooling beams to ensure efficient sampling of a large capture volume in the MOT cell. One way to generate six independent 2" diameter beams requires the use of six separate 2" lenses, each lens part of an individual beam-expanding telescope. This method requires several 2" diameter optical components on the optical table in the vicinity of the MOT cell, which is a rather inefficient use of space as well as money.

We have instead generated six diverging beams by sending six 2 cm diameter beams into six separate 1" diameter positive lenses that first bring the beams to a focus and then allow the beams to expand. These 100 mm focal length lenses are placed 400 mm from the center of the MOT cell, far enough away to allow the diverging beams to expand to a ~ 10 cm diameter at the location of the MOT. A photograph of the MOT cell and neighboring optics is shown in Figure 2.13.

The diverging beams make the MOT less susceptible to optical misalignment and standing-wave problems caused by counter-propagating collimated beams. Another advantage of using diverging beams is the relative insensitivity to small mirror misalignments, which have a negligible effect on the MOT and on loading the MOT into the initial magnetic trap.

This method of using diverging beams is similar to a technique used to create an atom trap that relies solely on optical pumping and does not require a magnetic field [45], a phenomenon we have observed with our diverging beams as well.

We use a total of 450 mW in the six cooling beams, resulting in an intensity of $2.9 \text{ mW/cm}^2 = 1.8 I_{sat}$ at the location of the MOT. The MOT beams are tuned 4Γ below the $|F = 2 \rightarrow F' = 3\rangle$ transition during MOT loading.

The repump beam travels along the same path as the four horizontal cooling beams, resulting in four diverging beams with a diameter of ~ 10 cm at the MOT location. We use a total of 30 mW in the repump beam, resulting in a total intensity at the MOT of $0.19 \text{ mW/cm}^2 = 0.12 I_{sat}$. The repump beam is tuned to be in resonance with the $|F = 1 \rightarrow F' = 2\rangle$ transition.

A magnetic field gradient is needed to provide a restoring force that traps the atoms cooled by the laser beams; the magnetic field gradient produced by our MOT

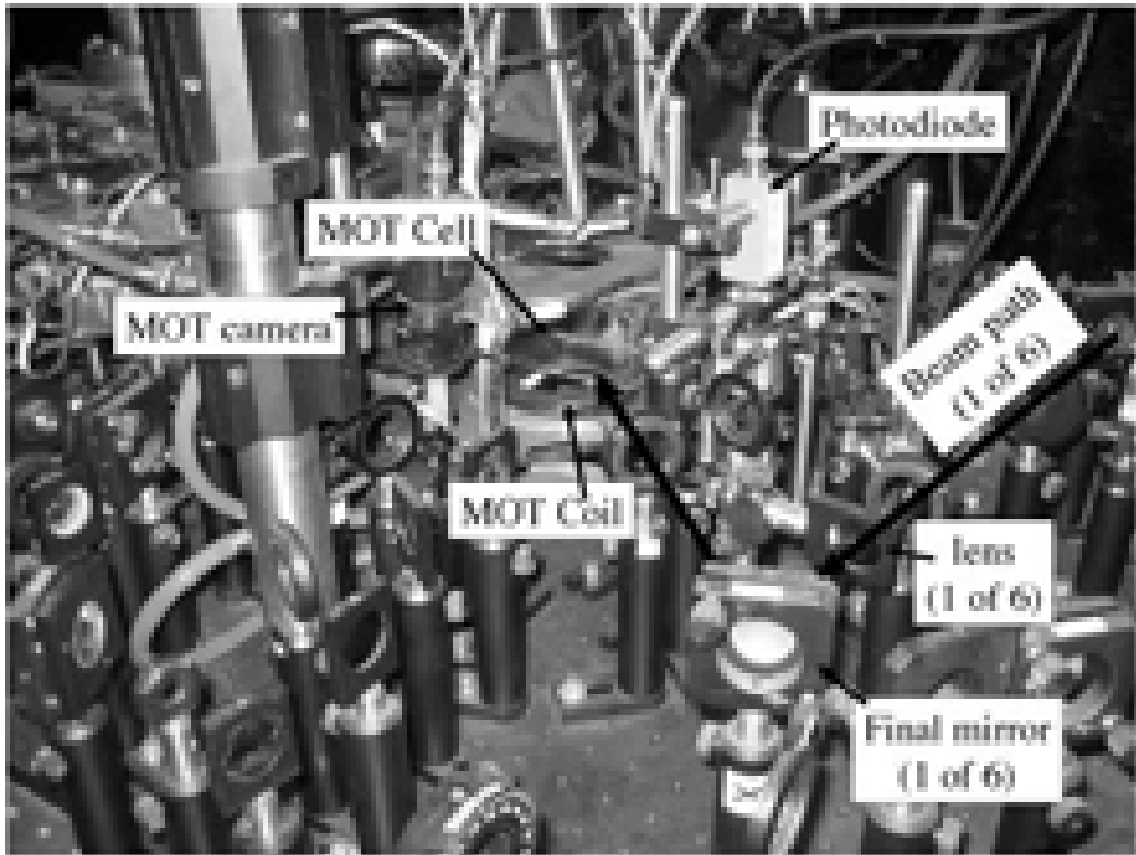


Figure 2.13: Photograph of MOT optics. The MOT cell is highlighted and sits in between two copper plates. Each of the two MOT coils (one is highlighted) are attached to the water-cooled copper plates. The photodiode used for collecting fluorescence from the MOT is highlighted. One of the six beam paths used for the MOT beams is highlighted in bold arrows; the lens used to create a diverging beam and final mirror are shown for this beam path. A CCD camera is mounted vertically to observe the MOT through a reflection off a mirror mounted at 45° .

coils is 8 G/cm axially (vertically) during the MOT loading phase. The basic circuit used to drive the MOT coils makes use of a linearized current-voltage relationship by applying feedback onto the gate of a power MOSFET; a similar circuit will be described in much more detail when describing the magnetic transfer coils in Chapter 3. A schematic of the MOT circuit is shown in Figure 2.14.

Using six independent counter-propagating beams requires the use of six individual 1" diameter quarter-wave plates. Small rotations of these waveplates have a negligible effect on the number of atoms in the MOT, but can affect the loading efficiency into a magnetic trap. We also use three orthogonal magnet coils to null out the background magnetic field, mostly caused by the permanent magnets of the ion pumps. Small adjustments of these nulling coils will shift the position of the MOT and can cause an observable difference in loading into the initial magnetic trap.

A photodiode placed near the MOT cell records fluorescence from the MOT. A collection lens is placed as close to the MOT cell as possible, and focuses the fluorescence from the MOT onto a photodiode. Based on the solid angle subtended by the collection lens, we can calculate the percentage of the total amount of fluorescence given off by the MOT that arrives at the photodiode. Using this and the scattering rate caused by the cooling beams, we can calculate the number of atoms in the MOT. The total power P emitted from the MOT in all directions is equal to the number of atoms N in the MOT multiplied by the scattering rate multiplied by the energy per photon $h\nu_{Rb}$ [42].

$$P = N \frac{1}{2} \frac{I/I_{sat}}{[1 + I/I_{sat} + 4 \cdot (\Delta/\Gamma)^2]} \frac{h\nu_{Rb}}{\tau_{nat}} \quad (2.1)$$

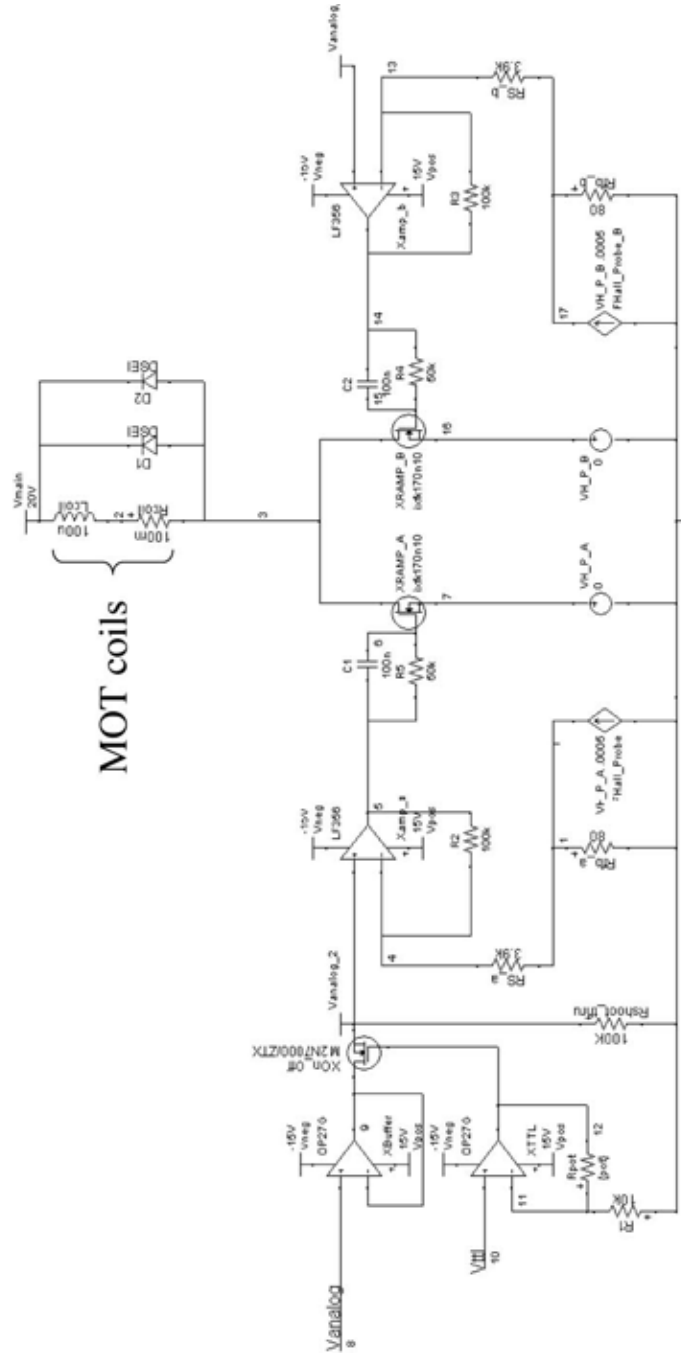


Figure 2.14: Schematic of the MOT circuit. The power supply is shown as V_{main} . The MOT coils are depicted as a resistor in series with an inductor, a fly-back power diode is placed in parallel with the coil. The coil is driven using two load-balanced power MOSFETs and two Hall Probes, described in detail in Chapter 3.

The saturation intensity I_{sat} is defined as

$$I_{sat} = \frac{1}{2} \frac{h\nu_{Rb}}{\sigma_0 \cdot \tau_{nat}} \quad (2.2)$$

where $h\nu_{Rb}$ is the energy of a photon, Δ is the detuning from resonance of the scattering light, Γ is the natural linewidth of the atomic transition, τ_{nat} is the scattering time, and σ_0 is the on-resonance absorption cross-section. This is a convenient definition of the saturation intensity I_{sat} , written as an energy ($h\nu_{Rb}$) per unit area (σ_0) per unit time (τ_{nat}) [31].

Knowing the solid angle of collected light and the intensity and detuning of the cooling beams, we calculate the number of atoms in the MOT to be $N = 3 \cdot 10^9$ atoms. We can fit the observed rise in MOT fluorescence during MOT loading to the following expression:

$$N(t) = N(1 - e^{-t/\tau_{MOT}}) \quad (2.3)$$

This results in a MOT filling time of $\tau_{MOT} = 15$ s with the Rb dispensers running at 3.4 A. The cloud size is ~ 1 cm in diameter, easily visible to the human eye despite the fact that the ^{87}Rb fluorescence given off by the MOT is at 780 nm, in the near-infrared.

2.6 CMOT

The compressed MOT (CMOT [46]) stage of our experiment spatially compresses the MOT and causes a temporary increase in density, which aids in the loading of ultracold atoms into a magnetic trap. Several factors are important in the CMOT stage, and we have noticed that periodic fine-tuning of CMOT parameters aids greatly in the number of atoms in the eventual BEC, a quantity that can be subject to periodic degradation.

The desired compression in the CMOT stage can be achieved by allowing a population of atoms to build up in the $|F = 1\rangle$ state. This allows them to stay out of the $|F = 2 \rightarrow F' = 3\rangle$ absorption events caused by the cooling beams. The dominant player that causes this to occur is the repump intensity; by turning the repump intensity down for a short period of time while keeping the cooling beams on, atoms do not get pumped out of the $|F = 1\rangle$ state. The other major player in this process is the detuning of the cooling beams. By making the cooling beams even more red-detuned from the $|F = 2 \rightarrow F' = 3\rangle$ transition, we decrease the scattering rate and achieve the same result.

The CMOT phase is 40 ms long and consists of ramping the cooling beam detuning from -4Γ to -7Γ over this time (the intensity also decreases by $\sim 35\%$), ramping the magnetic field gradient from 8 G/cm to 0 G/cm, and switching the repump power from 30 mW (full power) to 260 μ W for the duration of the CMOT phase.

As stated previously, optimization of the magnetic field nulling coils can have a major effect on loading atoms into the initial magnetic trap, the step which follows the CMOT stage. This is partly because adjustments of the nulling coils can physically move the MOT into or out of position with the $B = 0$ point, where the center of the magnetic trap exists. This is especially important in the CMOT stage, where the lower magnetic field gradient makes the $B = 0$ point more easily shifted by the fields due to the nulling coils.

Our experiment does not include an optical molasses phase, as we have noticed that any decrease in temperature afforded by a molasses phase is totally offset by an accompanying decrease in density due to the lack of magnetic field gradient in

the molasses phase. The physical expansion of the cloud, even in a short optical molasses phase, has hindered our ability to load cold atoms into a magnetic trap for the preparation of a BEC.

2.7 Optical Pumping

After the CMOT phase, the cooling beams (still at the CMOT detuning) stay on for an additional 1 ms, during which time the repump beam and magnetic field gradient are both off. This forces all the atoms to populate the $|F = 1\rangle$ state. Only one of the three magnetic sublevels, the $|F = 1, m_F = -1\rangle$ state, is magnetically trappable, so when we turn on the magnetic trap in the next stage of the experiment, we can only expect to trap atoms that get projected into this state. Since there is no optical pumping into a particular Zeeman sublevel, we can expect to trap about 1/3 of the atoms.

In the past, we have attempted to install Zeeman-sublevel pumping into the $|F = 1, m_F = -1\rangle$ state by using a linear magnetic bias field, a $|F = 1 \rightarrow F' = 1\rangle$ σ^- optical pumping beam, and a $|F = 2 \rightarrow F' = 2\rangle$ σ^- pumping repumper beam. However, we have found that the small gains in number of trapped atoms is not worth the effort involved in this step.

2.8 Initial Magnetic Trap

After the MOT loading, CMOT, and optical pumping phases of the experiment, the atoms are transferred into the initial magnetic trap formed by the MOT coils. This occurs by turning on the axial magnetic field gradient in the MOT coils to 40 G/cm, and then ramping the strength of the field gradient up to 180 G/cm over 100 ms.

The MOT ‘catch’ value of 40 G/cm, the initial strength of the quadrupole trap, should be relatively low in an attempt to approximately mode-match the initial magnetic trap to the size of the atomic cloud.

This concludes the first major stage in our BEC formation process: loading a MOT and magnetically trapping atoms in the MOT cell. The next major stage, magnetically transferring atoms into the science cell, will be described in Chapter 3.

CHAPTER 3

MAGNETIC TRANSFER OF ATOMS TO SCIENCE CELL

3.1 Introduction

Chapter 2 described the first stage in our BEC formation sequence, loading atoms in a MOT and trapping them in the initial magnetic trap in the MOT cell. The next stage in the BEC formation process, magnetic transfer of atoms into the science cell, is described in this chapter.

The organization of this chapter is as follows: Section 3.2 provides a conceptual overview of the transfer system and components used. Section 3.3 provides a description of all the hardware (magnet coils, power supply, and electronic circuits) used in the transfer process. Section 3.4 provides a description of the calculation used to determine the sequence of current ramps sent to the magnet coils used in the transfer process. Finally, section 3.5 summarizes the transfer system and lists some of the advantages and disadvantages of our method.

3.2 Overview of the Magnetic Transfer System

A pair of coils wired in anti-Helmholtz configuration provide the simplest method for magnetically trapping neutral atoms: a quadrupole magnetic trap [47]. This configuration provides a $|\vec{B}| = 0$ point on-axis in between the coils and a spatially varying magnetic field that increases linearly from the center of the trap.

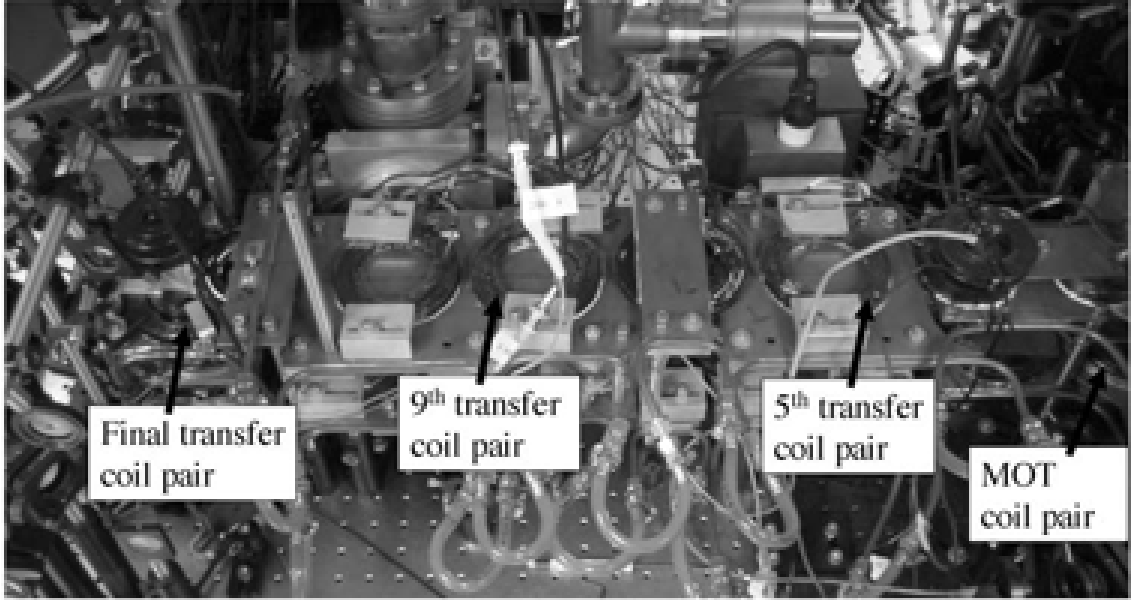


Figure 3.1: Photograph of magnetic transfer coils. The MOT coil pair, 5th, 9th, and final (14th) transfer coil pair are highlighted. The horizontal distance between the center of the MOT coil pair and the center of the final transfer coil pair (BEC location) is 76.2 cm.

In order to magnetically transfer atoms through the transfer tube that connects the MOT cell to the science cell, we have expanded on this idea by operating current through an array of 14 pairs of anti-Helmholtz coils placed above and below the transfer tube. A photograph of the transfer coils is shown in Figure 3.1.

By ramping the array of transfer coils on and off such that the $|\vec{B}| = 0$ point moves down the transfer tube, the magnetically trapped atoms will follow the potential minimum down the transfer tube and into the science cell. This procedure is based upon the magnetic transfer system described by Greiner *et al.* in 2001 [48]. This procedure requires three pairs of coils to be on at a time, creating a magnetic trap that is elongated in the transfer direction. The coils are ramped on and off in sequence such that initially coil pairs 1, 2, and 3 are on; then 2, 3, and 4; then 3, 4,

and 5; etc.

The components involved in the magnetic transfer system can be divided into two categories: (1) the hardware and electronics components that operate to actually control the transfer system on a day-to-day basis, which will be described in Section 3.3; and (2) the calculation that determines the current sequence used for transfer. The results of this calculation, described in Section 3.4, can be used over and over to transfer atoms unless a change in the transfer procedure is desired.

3.3 Hardware Used in the Magnetic Transfer System

3.3.1 Overview of components used

A schematic of all the hardware and electronics components used in the magnetic transfer system is shown in Figure 3.2. This complete schematic shows all the components which together comprise what we refer to as the ‘transfer circuit’, these include many electronics boxes, a power supply, 14 transfer coil pairs, two function generators, and the experiment PC.

To understand the operation of the transfer circuit, first consider the role of the ‘transfer control box’, which is the mastermind behind the entire system. The transfer control box receives three time-varying analog inputs that control the amount of current flow through the three coil pairs that are in operation at any given time. These three signals, labeled A, B, and C in Figure 3.2, are the result of a calculation (described in Section 3.4) that determines the current ramps needed for magnetic transfer. These three analog signals originate from the experiment PC and are loaded onto the arbitrary waveform SRS function generator. We use the sample-and-hold circuit to split up the signal from the SRS into three separate ramps, a

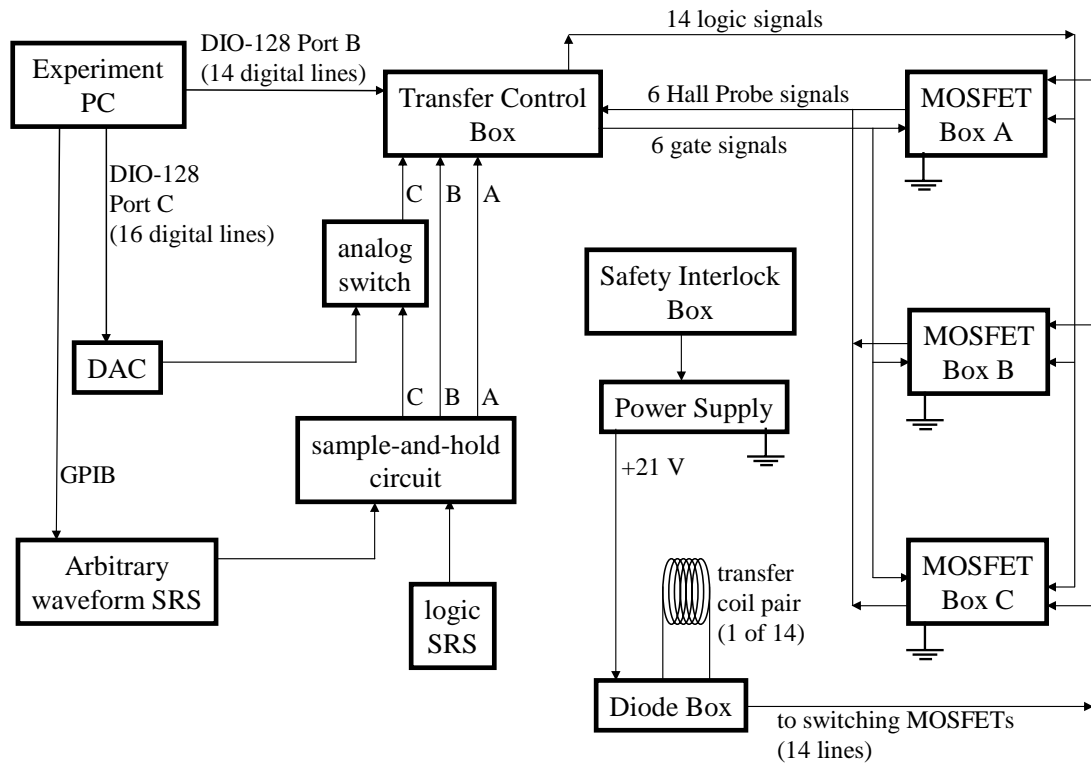


Figure 3.2: Schematic of the overall transfer system. This figure shows all the components that make up the ‘transfer circuit’; this includes many electronics boxes, a power supply, 14 transfer coil pairs, two function generators, and the experiment PC.

process that is described in Section 3.3.4. The transfer control box also receives 14 digital inputs from the experiment PC, which act to turn on and off the coils in sequence.

The transfer control box takes these three analog and 14 digital inputs and uses them to control the 14 pairs of transfer coils. It does this by sending 14 logic signals to the 14 switching MOSFETs which reside in the MOSFET boxes (described in Section 3.3.6); these signals act to turn on and off the individual coils. Two Hall probes reside in each MOSFET box to monitor the amount of current flow through each of the three coil pairs that are operational at any given time. The signals from the Hall probes are then fed back into the transfer control box, which regulates the amount of current flow through each coil group by sending the appropriate voltage to the gate of a ramping MOSFET in the MOSFET boxes. The principles of operation of this feedback loop are described in more detail in Section 3.3.5.

Positive current flows from the power supply, through the transfer coils, and into the MOSFET boxes, which contain a connection to ground. There are fly-back power diodes (described in Section 3.3.7) connected in parallel with each transfer coil pair to dissipate voltage spikes. A safety interlock box will inhibit the power supply and prevent the flow of current if any of the interlock conditions are met, as described in Section 3.3.8.

The following sections describe the individual components of the transfer circuit in more detail, all of the components will be described with reference to how they integrate into the overall system shown in Figure 3.2.



Figure 3.3: Photograph of a single magnet coil. The coil has an inner diameter of 6.5 cm.

3.3.2 Magnet coils and mounts

Magnet coils

All of the magnet coils used in our experimental apparatus are home-made coils constructed by winding magnet wire around a mold and using an epoxy to hold the wire together. For most of our coils, we have used polyurethane coated 12 AWG magnet wire with a diameter of 2.02 mm. We constructed a mold by making a custom-sized disc with 2 plates connected to either end, one of them having a slot to facilitate starting the winding process. The coils are wound on a lathe by connecting the mold to the lathe chuck and having one person manually rotate the lathe slowly while another person winds the coil around the disc. After one layer, MG Chemicals thermally conductive, electrically insulating epoxy, part number 832TC, is applied to the layer, and then another complete layer is wound. After the entire coil is constructed, the epoxy is then cured by either baking at 90 °C for a couple of hours or letting the coils sit at room temperature for a day. A photograph of one of the home-made coils used in the magnetic transfer system is shown in Figure 3.3.

Coil mounts

The transfer coils are mounted on copper plates above and below the transfer tube of the vacuum system, visible in Figure 3.1 on Page 65. Hollow copper tubing soldered to the copper plates allows for the flow of chilled water which cools the plates. Because the transfer coils do not need to switch on and off rapidly, there is no need to protect against eddy currents in these copper plates. This was not the case on the MOT and TOP trap plates, where we cut a slit through the plate to prevent circular eddy current flow. The water-cooled copper plates reach a temperature of $\sim 13^\circ\text{C}$ after running the chiller water for half an hour, which greatly reduces heating of the coils. The coils are clamped onto the plates in such a way that small adjustments of the physical position of each coil, though difficult, is possible. Based on careful measurements, we estimate that we have placed the coils to within ± 3 mm from the positions assumed in the calculation of Section 3.4.

Coil locations

Table 3.1 lists the locations of the transfer coils and various coil parameters. The inner radius of each coil, the x position (the horizontal distance from the center of the MOT coil pair to the center of the coil pair in question), and the z height (the vertical distance from the center of the transfer tube to the closest part of a coil) are tabulated. All of the coils are built out of 12 AWG magnet wire with an electrically insulating polyurethane coating. The plate separation, defined as the closest distance between the upper and lower copper plates on which the upper and lower coils are placed, is also tabulated. Calculated values for the inductance of each coil pair are also shown. Because only three transfer coil pairs are on at any

Coil	Rinner	X position	Z height	N	Config.	Plate Sep.	Group	L
MOT	3.25 cm	0 cm	3.05 cm	32	1	8.3 cm	C	138 μ H
Coil 1	1.5 cm	5.8 cm	4.47 cm	72	2	8.3 cm	A	322 μ H
Coil 2	3.25 cm	10.9 cm	3.05 cm	32	1	8.3 cm	B	138 μ H
Coil 3	1.5 cm	16.0 cm	4.47 cm	72	2	8.3 cm	C	322 μ H
Coil 4	3.25 cm	21.2 cm	2.6 cm	32	1	7.4 cm	A	138 μ H
Coil 5	3.25 cm	26.8 cm	4.02 cm	32	1	7.4 cm	B	138 μ H
Coil 6	3.25 cm	32.3 cm	2.6 cm	32	1	7.4 cm	C	138 μ H
Coil 7	3.25 cm	37.9 cm	4.02 cm	32	1	7.4 cm	A	138 μ H
Coil 8	3.25 cm	43.3 cm	2.6 cm	32	1	7.4 cm	B	138 μ H
Coil 9	3.25 cm	48.7 cm	4.02 cm	32	1	7.4 cm	C	138 μ H
Coil 10	3.25 cm	54.1 cm	2.6 cm	32	1	7.4 cm	A	138 μ H
Coil 11	3.25 cm	59.5 cm	4.02 cm	32	1	7.4 cm	B	138 μ H
Coil 12	3.25 cm	64.9 cm	2.6 cm	32	1	7.4 cm	C	138 μ H
Coil 13	2.2 cm	70.5 cm	4.02 cm	63	3	7.4 cm	A	361 μ H
Coil 14	3.25 cm	76.2 cm	2.0 cm	32	1	3.55 cm	B	138 μ H

Table 3.1: For each coil pair in the magnetic transfer system, the inner radius, x position, z height, number of turns N , coil configuration (see Table 3.2), plate separation, group, and inductance L are shown.

Configuration	Coils	Inner Diameter	Thickness	Turns	Total Turns
1	2,4-12,14	65 mm	11 mm	4 axial x 8 radial	32
2	1,3	30 mm	15 mm	7,6,7,6,7,6,7,6,7	72
3	13	44 mm	17 mm	7 axial x 9 radial	63

Table 3.2: Three different coil configurations were used in construction of the transfer coils. For each coil configuration shown above, the inner diameter of the coil, axial thickness of the coil, number of wraps and turns, and total number of turns are given.

given time, the coils can be divided into three groups, labeled Group A, B, and C, as shown in Table 3.1.

Based on physical constraints, we have used three different configurations for wrapping the coils. A table showing the three different configurations used and the coil properties for each configuration is shown in Table 3.2.

Push coils

During the initial period of testing the transfer system, we attempted to magnetically transfer atoms only a few cm down the transfer tube, transfer them back to the MOT cell, and image them there as a system check. We noticed that we could not transfer any atoms past a particular point in the transfer tube, right where the MOT cell glass met the metal flange of the vacuum system. This is where we installed a 6 mm diameter circular diaphragm into the vacuum system (highlighted in Figure 2.5), with the intention of limiting vacuum conductance from/into the MOT cell. Unfortunately, the diaphragm was not perfectly aligned with the transfer coils' $|\vec{B}| = 0$ point, and axial and transverse push coils were necessary to shift the $|\vec{B}| = 0$ point enough to allow the atoms to pass through the diaphragm.

3.3.3 Power supply and ground

We use an Agilent HP 6682A power supply to supply current to the MOT coil, transfer coils, DC TOP coils, and levitation coil. This power supply operates in constant voltage mode at 21 V, and is capable of supplying up to a total of 240 A. The ground on the supply is connected to the ground on the power line of our building. The optical table, which is electrically connected to a Uni-Strut shelf that is attached to the framework of our building, is connected to the ground of the power supply and serves as the reference ground for our laboratory.

3.3.4 Sample-and-hold circuit

The sample-and-hold circuit¹, visible in Figure 3.2 on Page 67, has two inputs and three outputs. It receives input signals from the ‘arbitrary waveform SRS’ and the ‘logic SRS’ and its three outputs eventually connect to the ‘transfer control box’. The transfer control box requires three input ramps to control the amount of current in coil groups A, B, and C. The purpose of the sample-and-hold circuit is to provide these three current ramps.

The transfer process operates with a digital update rate of $\Delta t = 1.1$ ms; over the 5.9 second transfer process there are over 5,000 digital updates in the current sequence. Because the time constant $\tau = R/L$ governed by the resistance R and inductance L of the transfer coils is on the order of the 1.1 ms update rate, we can approximate a smooth current ramp with a series of current steps updated at the 1.1 ms digital update rate. We were faced with the design problem of creating three different digital arrays of 5,000 updates each at a spacing of 1.1 ms.

One solution to this problem would be to use three different SRS arbitrary waveform function generators, which could be loaded with the three different ramps using a GPIB connection. Instead, we solved this problem by using two SRS function generators (the ‘arbitrary waveform SRS’ and the ‘logic SRS’ of Figure 3.2) and a simple home-made sample-and-hold circuit, thus reducing the potential cost of the project by almost 1/3. The arbitrary waveform SRS is used to send a combined version of the three current ramps to the sample-and-hold circuit, and the logic SRS controls the sampling rate. The details of this process are described in the following paragraphs.

¹For additional information, see the lab notebook entry on 10/27/2004.

The calculation that determines the appropriate current ramps for each transfer coil pair (which will not be described until Section 3.4) produces 14 individual current ramps, each describing the necessary current sequence for each individual coil pair. In software these 14 ramps are grouped into three waveforms corresponding to coil Groups A, B, and C. This is done by simply adding the non-overlapping current ramps (i.e. the non-overlapping ramps for coils 1, 4, 7, 10, and 13 are added together to form the sequence for Group A). These three waveforms corresponding to the three different groups are further combined in such a way that only *one* arbitrary waveform is loaded into the ‘arbitrary waveform SRS’. The three different waveforms are multiplexed together so that the array output reads (Group A value 1, Group B value 1, Group C value 1, Group A value 2, Group B value 2, etc). The sample-and-hold circuit then splits this combined input into three outputs. An example of this technique, illustrating how the sample-and-hold circuit separates one input into three outputs, is shown in Figure 3.4.

The combined waveform (the input of Figure 3.4) is created in software on the Experiment PC and loaded into the ‘arbitrary waveform SRS’ function generator using GPIB; this waveform is sent to the sample-and-hold circuit at an update rate of $f = 3/(\Delta t)$. Another function generator, the ‘logic SRS’ is programmed with a square wave at a frequency of $f = 1/(\Delta t)$.

The sample-and-hold circuit splits that square wave into three separate pulsetrains, each with a frequency of $f = 1/(\Delta t)$ and separated in time by $1/3$ of the sampling period Δt . The circuit employs NE555 timer chips to do this. These three pulsetrains are then sent to three different LF398 sample-and-hold chips, which all sample the same input array but output the three distinct current ramps required

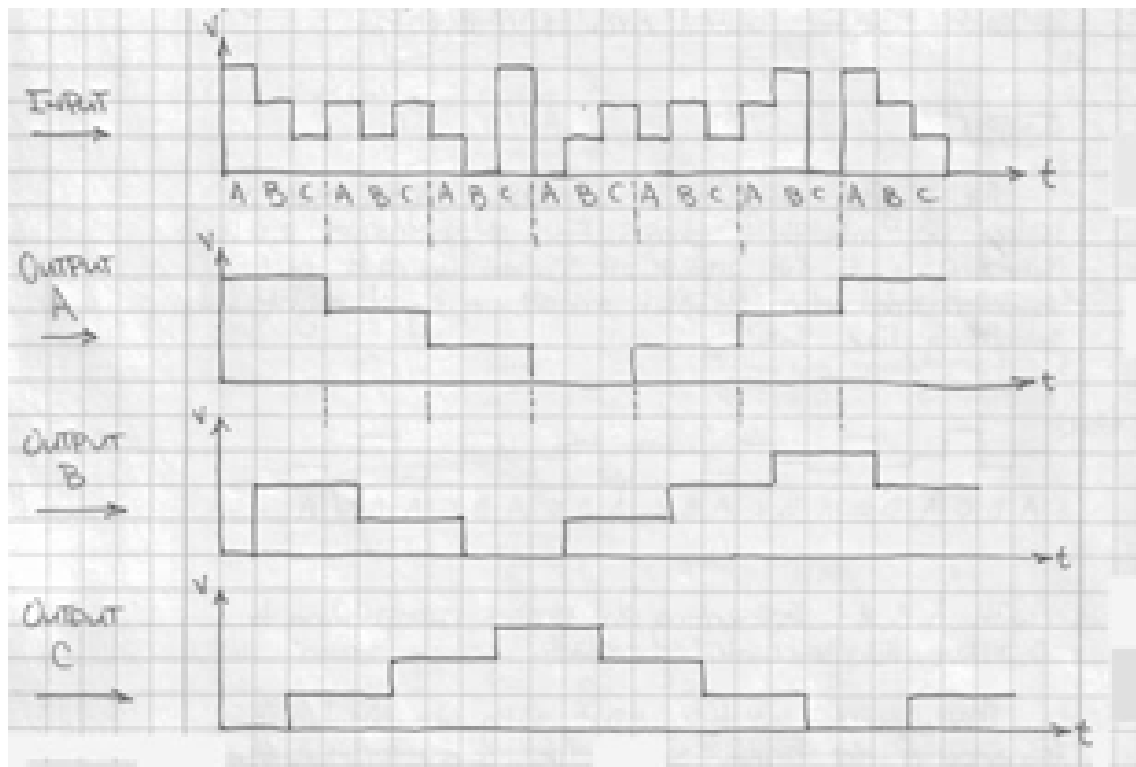


Figure 3.4: Illustration of sample-and-hold technique. The input signal is a combined version of the signals that will be sent to coil groups A, B, and C. The sample-and-hold circuit separates one input signal into three output signals, which will be sent to the 'transfer control box'. Drawing by David Kaz.

by the transfer control box, shown in Figure 3.4.

An additional sophistication is required on Group C because this group controls both the MOT coil and the DC TOP coils. The signal to the Group C input on the transfer control box is switched between two inputs using a Vishay DG419 analog switch. The analog switch connects either the output of the sample-and-hold circuit or the DAC output to the transfer control box. During the transfer process (i.e. when the MOT coil pair, coil pair 1, and coil pair 2 are on) the input to Group C comes from the sample-and-hold circuit, which controls the transfer process. During MOT loading or RF evaporation the input to Group C comes from the DAC, which controls the timing events before and after the transfer sequence.

3.3.5 Transfer control box

The ‘transfer control box’, shown in Figure 3.2 on page 67, has been described as the mastermind behind the entire transfer process. The transfer control box controls the amount of current flow through each of the transfer coil pairs. It does this by: (1) individually turning on and off the current flow through each of the 14 transfer coil pairs; and (2) controlling the variable amount of current through each transfer coil pair by monitoring and regulating its amount of current flow.

The complete electronics circuit used to drive the transfer coils includes not simply the transfer control box, but also the power supply, the coils themselves, and the MOSFET boxes, as described in Section 3.3.1. However, the operation of the entire system will be described in this section, with reference to the circuit diagram shown in Figure 3.5². This circuit diagram includes the electronics used

²This and all the circuit diagrams included in this dissertation were generated by M. David Henry in TOP Spice using the PSPICE 3f5 engine.

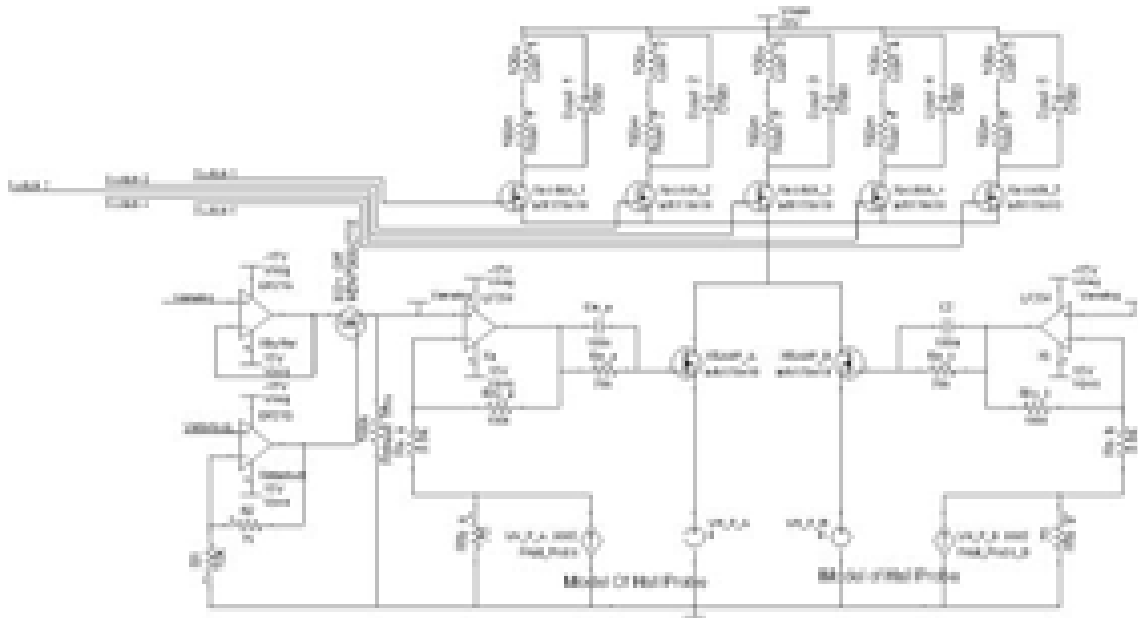


Figure 3.5: Circuit diagram showing the electronics components used to drive one group of five transfer coils. This circuit diagram will be repeated in Figure 3.6

to drive one group of five transfer coils, and includes elements physically situated within the MOSFET boxes, diode boxes, and transfer control box, as well as the coils themselves.

In order to better understand how the individual pieces of Figure 3.5 fit into the black-box components of Figure 3.2, three sections of Figure 3.5 are highlighted in Figure 3.6. These sections demarcate which portions of Figure 3.5 comprise the ‘transfer control box’ and ‘MOSFET box’; the transfer coils and diodes are also highlighted.

Operation of transfer circuit

This section provides an explanation of the circuit shown in Figure 3.6 by tracing the path of positive current flow from Vmain (the positive end of the power supply

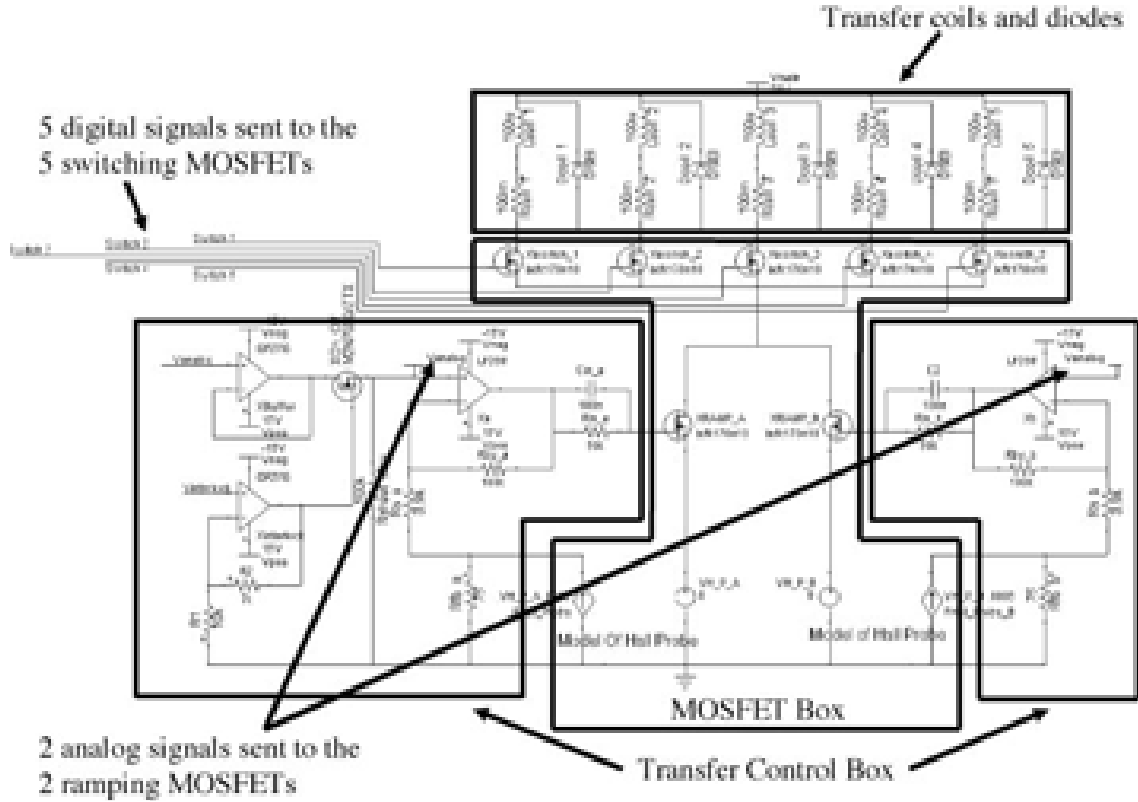


Figure 3.6: Circuit diagram showing the different sections of the circuit used to drive one group of five transfer coils. The box at the top of the schematic contains both the coils (situated on the optical table) and the diodes (housed in the diode box described in Section 3.3.7). Each transfer coil pair is modeled as an inductor (a coil) and a resistor in series. The two sections on either side of the schematic contain all the electronics in the transfer control box, described in Section 3.3.5. The section in the middle of the schematic contains all the power electronics in one of the MOSFET boxes, described in Section 3.3.6. The connections to the five switching MOSFETs (labeled Xswitch_1 through Xswitch_5) and two ramping MOSFETs (labeled XRAMP_A and XRAMP_B) are also shown. The Hall probes are modeled as voltage-dependent current sources.

at the top of the diagram) to ground. Current first flows through a transfer coil, modeled as an inductor in series with a resistor in Figure 3.6. There is a power diode placed in parallel with each transfer coil to prevent current spikes; the role of this diode will be discussed in more detail in Section 3.3.7.

Current then flows through one of the five switching MOSFETs, labeled as Xswitch_1 through Xswitch_5 in Figure 3.6. The switching MOSFETs used are Advanced Power Technology APT10M07JVR power MOSFETs; there is one individual switching MOSFET per coil pair that acts as an on/off switch for each coil pair.

The sources of the five switching MOSFETs are connected to the drains of the two ramping MOSFETs, labeled as XRAMP_A and XRAMP_B in Figure 3.6. Two ramping MOSFETs, IXYS model IXYS180N10, are used in each MOSFET box. These two ramping MOSFETs are placed in parallel and act as variable resistors, modifying how much resistance there is between the power supply and ground, and therefore, how much current flows through the coils. We use two ramping MOSFETs in parallel because of the high power demand on these MOSFETs; using two MOSFETs means that only half as much current will flow through each one compared to using only one MOSFET.

In each MOSFET box an electrical cable passes from the drain of each ramping MOSFET, through a Hall Probe, and connects to ground, as shown in Figure 3.7. However, for the purposes of circuit modeling, the Hall Probe is modeled as a voltage-controlled current source in Figure 3.6. Each ramping MOSFET is on a separate feedback loop and uses its own Hall Probe to monitor current. The Hall probes used, FW-Bell model CLN-200, are zero-resistance probes that measure the

amount of actual current flowing through the device by monitoring the induced magnetic field around the current-carrying wire. The feedback loop in the ‘transfer control box’ compares the amount of actual current (the signal send from the Hall Probe) to the desired amount of current (indicated as V_{analog} in Figure 3.6) with an LF356 op amp. The output of this op amp connects to the gate of the ramping MOSFET to make the actual amount of current equal to the desired amount of current.

Without this feedback loop, if a MOSFET were to heat up because of high current flow, the current through the coil would increase. The feedback loop prevents this thermal runaway by continually monitoring the amount of current flow and applying the proper voltage to the gate of the ramping MOSFET. Another advantage of the feedback loop is that we avoid having to use a voltage/current lookup table that would have to be generated for every MOSFET used. The feedback loop automatically adjusts the ramping MOSFETs’ gate voltage until the current is at the specified value.

Connections on transfer control box

The transfer control box, shown in black-box form in Figure 3.2 on Page 67, has 20 outputs and 23 inputs. On the back of the transfer control box there are 14 digital outputs that act to turn on and off individual coil pairs. These digital outputs originate from Port B on the DIO-128 and get amplified in the transfer control box to a logic high of 24 V to turn on the individual switching MOSFETs associated with each coil pair. The reason they need to be at such a high voltage is that the drain of each switching MOSFET is connected (through the coils) to the 21 V power supply,

and the gate-source voltage of these MOSFETs needs to be higher than the drain voltage to prevent these MOSFETs from operating in the triode region. There is an amplifier circuit inside the transfer control box that, after appropriate opto-isolation of the logic lines as shown in Figure 2.2, amplifies the logic high to 24 V.

There are six analog outputs on the back of the transfer control box, labeled ‘Gate signals’ in Figure 3.2, that are applied directly to the gates of the two ramping MOSFETs in each of the three MOSFET boxes. These signals control the resistance of each ramping MOSFET, regulating the time-varying amount of current through each coil.

There are six analog inputs on the back of the transfer control box, labeled ‘Hall Probe signals’ in Figure 3.2, that come from the six Hall Probes in the MOSFET boxes. These current signals get dropped across a resistor in the transfer control box to provide a voltage that is proportional to the actual amount of current flowing through each Hall Probe.

There are three analog inputs on the front of the transfer control box labeled Group A, B, and C. These are analog signals that come from the sample-and-hold circuit and provide the current ramps to be sent to the coils. Finally, there are 14 digital inputs on the back of the transfer control box that originate from Port B of the DIO-128.

3.3.6 MOSFET boxes

The role of the components in the MOSFET boxes within the overall scheme of the magnetic transfer system has already been described in the previous section. This section describes the physical layout and hardware of each MOSFET box.

Three identical boxes house the MOSFETs used to control coil Groups A, B, and C. These three MOSFET boxes are depicted in a black-box diagram in Figure 3.2 on Page 67, the power electronics within a MOSFET box are highlighted in Figure 3.6 on Page 78, and a photograph of one of the MOSFET boxes is shown in Figure 3.7.

As seen in Figure 3.7, each MOSFET box has seven BNC inputs and two BNC outputs on the front of the box, one 4 AWG connection to the power supply ground on the right side of the box, and five 8 AWG connections to the diode box (and hence the transfer coils themselves) on the left side of the box. Each MOSFET box contains five switching MOSFETs, two ramping MOSFETs, and two Hall Probes. The MOSFETs are mounted on a large copper plate that is water cooled with chiller water. On the front of the box, five logic signals from the ‘transfer control box’ connect directly to the gates of each of the five switching MOSFETs; two gate signals from the ‘transfer control box’ connect directly to the gates of the two ramping MOSFETs; and two Hall Probe signals originate from each MOSFET box and are sent to the ‘transfer control box’. The three MOSFET boxes are grounded together as well as connected to the power supply ground.

3.3.7 Diode box

The diode box is shown in the black-box diagram of Figure 3.2 on Page 67. The diode box contains 14 IXYS DSEI 2X101-06A power diodes that are each placed in parallel with a transfer coil pair and oriented such that the cathodes of these diodes connect to the positive end of the power supply. These fly-back power diodes act to dissipate large voltage spikes, such as what would occur if there was a large amount of current flowing through a coil and a switching MOSFET was suddenly turned

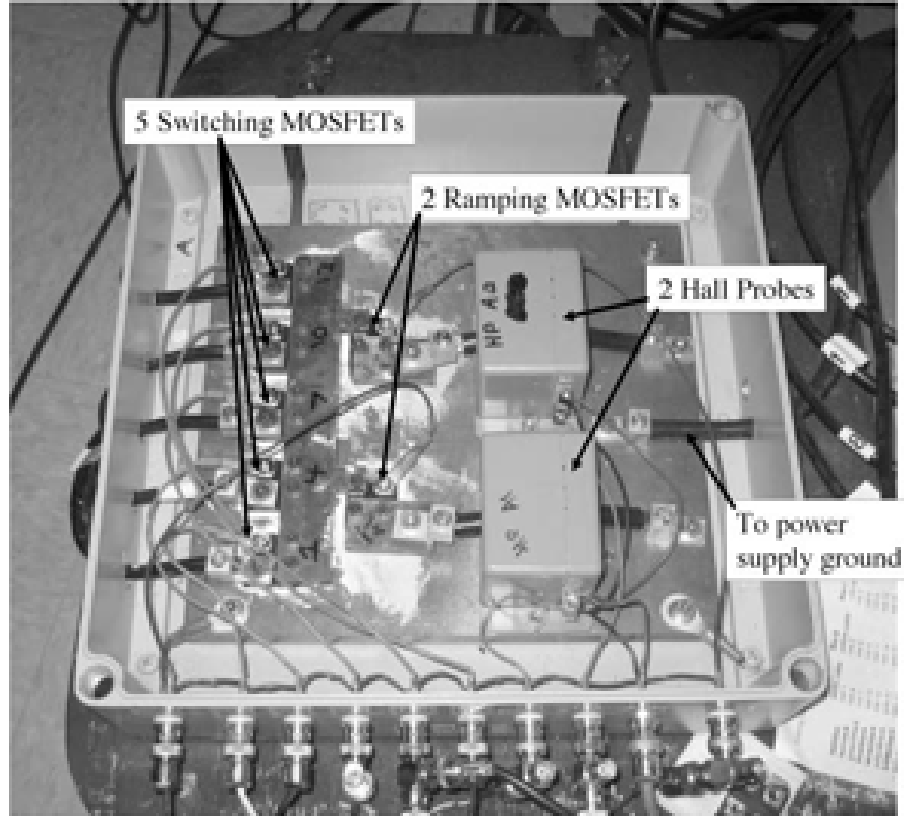


Figure 3.7: Photograph of one of the 3 MOSFET boxes, MOSFET Box A. MOSFET Box A controls transfer coil pairs 1, 4, 7, 10, and 13. The 5 cables on the left side of the box connect the transfer coils (through the diode box) to the 5 switching MOSFETs. The 5 switching MOSFETs connect to the 2 ramping MOSFETs through a copper plate. The current passing through each of the 2 ramping MOSFETs passes through a Hall Probe before connecting to a large water-cooled copper plate at the bottom of the MOSFET box. This copper plate is electrically connected both to the power supply ground and the optical table. The BNC connections on the front of the MOSFET box connect to the gates of the switching and ramping MOSFETs, and the power and output signals of the 2 Hall Probes.

off. Based on the relationship

$$V = L \frac{\partial I}{\partial t} \quad (3.1)$$

there would be a huge voltage on the drain of the switching MOSFET, potentially causing device failure. By installing a fly-back diode that operates only when the voltage on its anode is large enough (as in this situation), that transient current will flow back up through the diode instead of destroying the MOSFET.

As shown in Figure 3.2, the diode box contains the one and only connection to the positive end of the power supply, this connects to the cathodes of all the diodes and one end of each transfer coil pair. The other end of each coil pair is connected to the anode of its respective diode, and there is a 4 AWG wire connecting this point to the drain of the corresponding switching MOSFET in the MOSFET boxes.

3.3.8 Safety interlock box

There have been several times when an accident has occurred in lab and we found ourselves in a situation where 100 A or more was flowing steady-state through a coil, once heating the DC TOP coils to the point where epoxy melted onto the surface of the science cell. This usually occurs when a MOSFET blows up or when the computer crashes and sends an erroneous value to the transfer circuit. For this reason, we have installed several hardware safety interlocks that will automatically disable the Agilent power supply until a front-panel button is depressed, inhibiting the flow of current. The safety interlock box receives so many input signals from different parts of the experiment that they are not shown in Figure 3.2, rather, they are explained in the subsequent paragraphs.

Two of the safety interlock conditions are based on the flow of chiller water, through two separate flow meters that monitor water flow. Three of the safety interlock conditions are based on the temperatures of coils used in the transfer process, these are based on temperature readings using thermistors epoxied to the coils. The temperature trip points were set by recording the maximum temperatures of the monitored coils, and setting the trip point to be ~ 5 °C above that.

Three of the safety interlock conditions monitor the integrated amount of current through various coils. To set the trip point on the integrators, we adjusted the R and C values of the integrator circuits to operate on a timescale of several seconds and trip a comparator if the integrated value of current is $\sim 10\%$ larger than normal. Two of the safety interlock conditions are based on the instantaneous amount of current through particular coils. Both the integrated current interlocks and temperature interlocks operate slowly (on the timescale of a few seconds), but the chiller water and instantaneous current interlocks operate right away. The power supply will automatically enter into inhibit mode if any of the following conditions occur:

1. If the flow of the chiller water cooling the transfer coils' copper plates stops.
2. If the flow of the chiller water cooling the MOSFETs in the MOSFET boxes stops.
3. If the temperature of the MOT coil gets too hot and reaches its trip point.
4. If the temperature of the DC TOP coils get too hot.
5. If the temperature of the AC TOP coils get too hot.

6. If the integrated amount of overall current is too large and reaches its trip point. In addition to the several Hall probes that monitor current through the MOT coil, transfer coils, DC TOP coils, and levitation coil (used for BEC imaging), we have installed a Hall Probe directly to the output of the Agilent power supply to monitor the total amount of current flow. A voltage proportional to the total instantaneous amount of current flow is sent to an integrator circuit. The output of this integrator circuit rises slowly over the course of the transfer sequence and will trip a comparator and inhibit the power supply if the total integrated amount of current is too high.
7. If the integrated amount of current in the MOT coil is too high.
8. If the integrated amount of current in the DC TOP coils is too high.
9. If the instantaneous amount of current in the DC TOP coils is too high. At the beginning of the evaporation sequence, the DC TOP coils operate at their highest value of 20 A. If the amount of instantaneous current in the DC TOP coils exceeds 30 A, the safety interlock circuit will inhibit the power supply.
10. If the instantaneous amount of current through the levitation coil is greater than 15 A.

If any one of the above conditions is met, that portion of the interlock circuit sends a TTL low signal to a multi-input AND gate in the safety interlock box. A TTL low signal at the output of the AND gate will inhibit the power supply. If we lose power to the safety interlock box or if one of its internal components fails, the logic output will also be low, inhibiting the power supply. One consequence of using integrators in the safety interlock circuit is that we need to wait ~ 30 seconds between each

run of the experiment, or the integrated values from running the transfer sequence too frequently will inhibit the power supply. This is usually a good idea, however, because running too frequently, though possible, will tend to decrease the lifetime of the power MOSFETs due to overheating.

3.3.9 Direction of current flow

Positive current flows from the power supply (under the optical table) to the cathode of a diode in the diode box (under the optical table) through a transfer coil pair (mounted around the vacuum system on the optical table), and back to the anode of a diode in the diode box. Current then flows through a switching MOSFET and a pair of ramping MOSFETs and Hall Probes, all of which are located in one of the MOSFET boxes (under the optical table). The current path terminates at the ground in the MOSFET box, which itself is connected to the power supply ground. The DAC, arbitrary waveform SRS, logic SRS, sample-and-hold circuit, analog switch, and transfer control box are all located on the 19" equipment rack.

3.4 Calculation of the Current Sequence

The previous sections have described the hardware, electronics, and principles of operation of the magnetic transfer system. The only things that have been left out are: (1) a description of the calculation that produces the three current ramps that are sent to the ‘transfer control box’; and (2) a description of the center-of-mass velocity of the atoms as they move down the transfer tube. Both of these topics are addressed in this section.

The following paragraphs describe the calculation that produces the current ramps that are sent to the transfer control box. We will use the convention that z is the vertical (gravity) direction, x is the longitudinal (along the direction of the transfer tube) direction, and y is the transverse direction. The magnetically trapped atoms start in an axially symmetric quadrupole trap in the MOT cell with $\partial B/\partial z = 180$ G/cm, $\partial B/\partial x = -90$ G/cm, and $\partial B/\partial y = -90$ G/cm. Because three pairs of coils are on during the transfer process, the magnetic trap gets elongated in the transfer direction to form a 3-dimensional trapping potential with $\partial B/\partial z = 180$ G/cm, $\partial B/\partial x = -65$ G/cm, and $\partial B/\partial y = -115$ G/cm.

A 3-dimensional calculation was performed to determine the current ramps necessary to produce the desired magnetic field gradients. The calculation used the Biot-Savart law to determine the magnetic field and magnetic field gradient along the transfer tube in all 3 orthogonal directions as a function of the amount of current through the transfer coils. For a single coil of radius R perpendicular to the z axis and centered at $z = A$, the transverse magnetic field component B_ρ and the axial magnetic field component B_z as a function of axial and radial position z and ρ are [49]

$$B_z = \frac{\mu I}{2\pi} \frac{1}{[(R + \rho)^2 + (z - A)^2]^{1/2}} \cdot \left[K(k^2) + \frac{R^2 - \rho^2 - (z - A)^2}{(R - \rho)^2 + (z - A)^2} E(k^2) \right] \quad (3.2)$$

$$B_\rho = \frac{\mu I}{2\pi\rho} \frac{z - A}{[(R + \rho)^2 + (z - A)^2]^{1/2}} \cdot \left[-K(k^2) + \frac{R^2 + \rho^2 + (z - A)^2}{(R - \rho)^2 + (z - A)^2} E(k^2) \right] \quad (3.3)$$

where μ is the Bohr magneton, I is the current through the coil, and

$$k^2 = \frac{4R\rho}{(R + \rho)^2 + (z - A)^2} \quad (3.4)$$

is the argument of the complete elliptic integrals K and E [50]. From the preceding equations it is straightforward to determine the magnetic field at two neighboring

points in order to construct a field gradient. With three coils on at a time, it is also straightforward to set up a matrix of three equations and three unknowns. This matrix equation is solved at one particular point in space, starting at the center of the MOT cell, to determine what currents are necessary to produce the desired field gradients at that point. Then the matrix equation is solved again at each subsequent point in space along the transfer tube along a linear grid of spacing $\Delta x = 0.165$ mm. The inputs to the matrix equation are the three known quantities:

1. $|\vec{B}| = 0$ at that particular point in space (therefore atoms are magnetically trapped there).
2. $\partial B/\partial x$ (along the transfer direction) equals the desired longitudinal gradient.
3. $\partial B/\partial z$ (along the vertical direction) equals the desired axial gradient.

The three unknowns are the three currents (I_1 , I_2 , and I_3) in the three neighboring coil pairs that happen to be on at a given time. The 3×3 matrix M is determined from the Biot-Savart Law, which determines the resultant magnetic fields from input currents and specified coil locations.

$$\begin{pmatrix} |\vec{B}| \\ \partial B/\partial x \\ \partial B/\partial z \end{pmatrix} = \begin{pmatrix} 0 \\ -65 \text{ G/cm} \\ 180 \text{ G/cm} \end{pmatrix} = \begin{pmatrix} M_1 & M_2 & M_3 \\ M_4 & M_5 & M_6 \\ M_7 & M_8 & M_9 \end{pmatrix} \cdot \begin{pmatrix} I_1 \\ I_2 \\ I_3 \end{pmatrix} \quad (3.5)$$

To understand how the values of the matrix M are determined, consider the following example: when the atoms are at position $x = 3$ cm down the transfer tube, transfer coil pairs 1, 2, and 3 are on. The calculation determines the three currents I_1 , I_2 , and I_3 through transfer coil pairs 1, 2, and 3 required to make

$|\vec{B}| = 0$, $\partial B/\partial x = -65$ G/cm, and $\partial B/\partial z = 180$ G/cm at the position $x = 3$ cm. Matrix values M_1 , M_2 , and M_3 are the large prefactors in Equations 3.2 and 3.3 that set up the equation

$$|\vec{B}| = 0 = B_z + B_\rho = M_1 \cdot I_1 + M_2 \cdot I_2 + M_3 \cdot I_3 \quad (3.6)$$

which is the top row of the matrix equation 3.5. The other values of the matrix, M_4 through M_9 , relate the currents in coil pairs 1, 2, and, 3 to the field gradients along x and z at this position in space, and are determined from taking a spatial derivative of Equations 3.2 and 3.3.

The required current ramps and resultant magnetic field gradients, plotted alongside the coil locations, are shown in Figure 3.8. Figure 3.8 (a) is a side view of the 15 coil pairs (the MOT coil and 14 transfer coils), showing their to-scale positions and widths along the transfer (x) direction and vertical (z) direction.

The thin vertical lines in Figure 3.8 (a) indicate ‘breakpoints’, additional adjustable parameters in the calculation. These user-adjustable breakpoints are the position locations where one coil turns off and another turns on. For example, the breakpoint position of $x = 39.4$ cm is the longitudinal position of the moving atom cloud where transfer coil pair 6 turns off and transfer coil pair 9 starts turning on. The breakpoint locations were adjusted to optimize the current ramps for smooth field gradients. After this optimization, we noticed that coil pairs farthest from the transfer tube in the z direction operate over a longer range in x than coil pairs closer to the tube.

Figure 3.8 (b) shows the result of the simulation, the current ramps required for each coil pair in order to produce the desired field gradients. The breakpoints

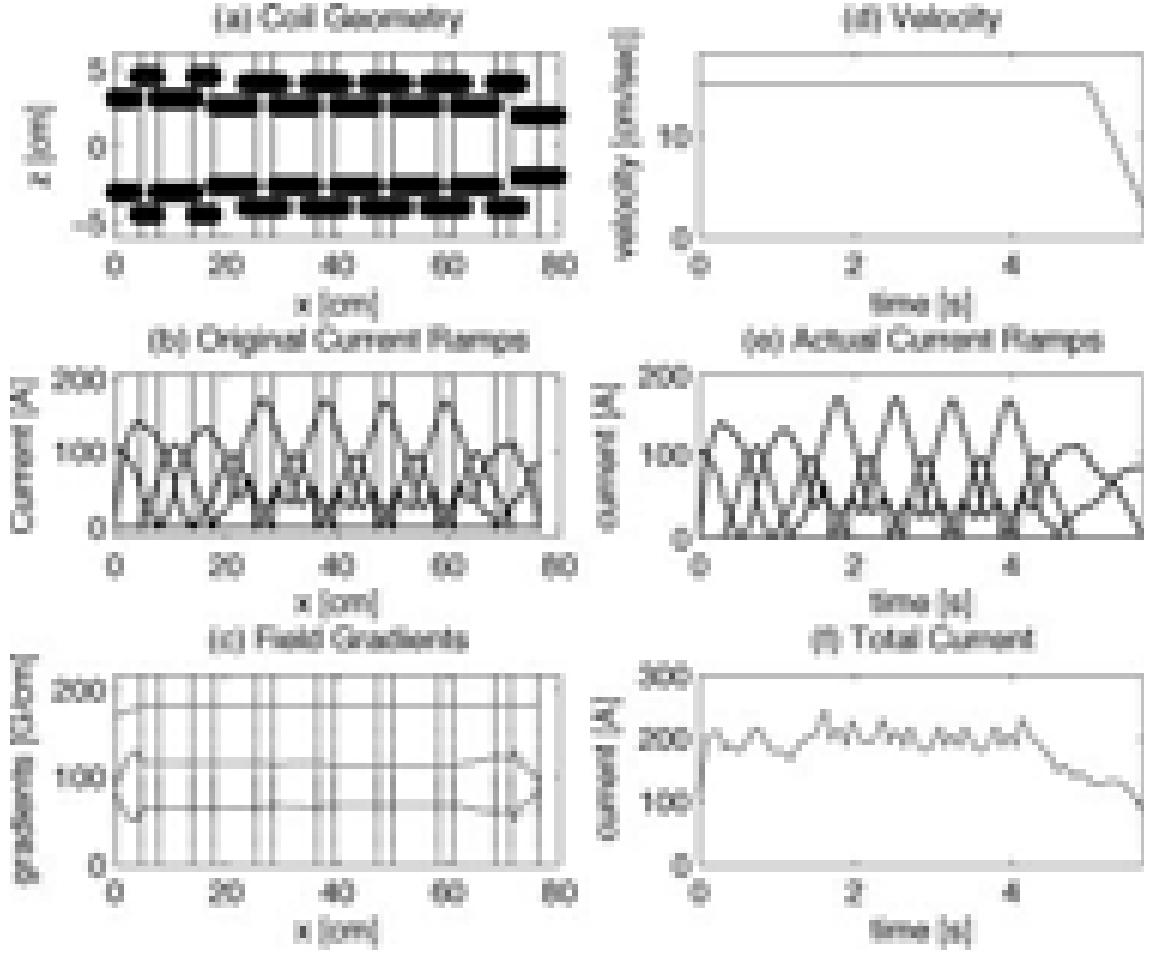


Figure 3.8: Coil locations, current ramps, and field gradients for magnetic transfer system are shown. (a) Shown are the locations of the MOT coil pair and all 14 transfer coil pairs. This is a to-scale rendering of all the coil positions, outer diameters, and heights. Also shown are the breakpoints, the positions in space where one coil turns off and another turns on. (b) Shown are the original current ramps (the result of the calculation) with current [A] plotted as a function of position x [cm]. Each coils' current ramp is plotted directly beneath the coil position. (c) Shown are the magnetic field gradients resulting from the current ramps shown in (b); the largest magnetic field gradient is $|\partial B/\partial z|$, the intermediate magnetic field gradient is $|\partial B/\partial y|$, and the weakest field gradient is $|\partial B/\partial x|$. Figures (a), (b), and (c) are plotted on the same spatial horizontal axis. (d) Shown is the atomic velocity vs. time [s] over the transfer time, reflecting the final deceleration stage. (e) Shown are the actual current ramps used for transfer, which differ from (b) in that the final portion of transfer reflects the deceleration. (f) Shown is the total amount of current used for transfer vs. time [s]. Figures (d), (e), and (f) are plotted on the same temporal horizontal axis.

are still shown, and it is clear that these are the position locations where one coil pair turns off and another starts ramping on. Figure 3.8 (c) shows the magnitude of the magnetic field gradients produced while using the above current ramps. The largest field gradient is in the axial (z) direction, while the weakest field gradient is in the transfer (x) direction. The field gradients vary at the beginning and end of the transfer sequence, these are the regions where only one or two transfer coil pairs are operational. Figures 3.8 (a), (b), and (c) plot the coil locations, current ramps, and field gradients as a function of position x (in cm) along the transfer direction, but do not provide any information on the timescale of the transfer process, which is dependent on the velocity of the moving $|\vec{B}| = 0$ point.

In order to optimize the number of atoms transferred from the MOT cell to the science cell, the velocity and acceleration of the moving magnetic trap was adjusted. We originally thought we would need to increase the initial velocity of the atoms up from zero to the nominal velocity of 15 cm/s and then decrease the velocity back to zero at the end of the transfer process in order to keep the atomic motion as adiabatic as possible. We initially thought that these acceleration/deceleration steps would be rather important in optimizing transfer efficiency; however, we have observed that the transfer efficiency is not very dependent on these steps or the nominal velocity. After optimizing the process, we discovered that the initial acceleration phase actually decreased the number of transferred atoms, presumably because the slower initial speeds meant that trapped atoms spent a longer time in the MOT cell, the highest-pressure region of the chamber, and underwent more collisions with background atoms. We did notice, however, that a small amount of deceleration at the end of the transfer process increased the transfer efficiency slightly.

After optimization, we found that it is best to start the transfer process with an initial velocity of 15 cm/s and include a deceleration phase to 3 cm/s over the final 1 second of the 5.9 second transfer process. A plot of the calculated center-of-mass atomic velocity vs. time is shown in Figure 3.8 (d). A plot of the actual current ramps used vs. time is shown in Figure 3.8 (e). These current ramps differ only slightly from the ramps shown in Figure 3.8 (b) in that they are plotted as a function of time and the last 1 second is a visibly lengthened version of the original current ramps, indicating a slower atomic velocity. Figure 3.8 (f) shows a plot of the total current used through all the coils vs. time.

3.5 Transfer Revisited

Based on the amount of time involved in the design and implementation of the magnetic transfer system, it is easily the most complex part of our laboratory. Successful operation of the transfer system took one B.S. thesis in Electrical Engineering by M. David Henry [51], over two years of work, a lot of software and hardware, and many blown-up MOSFETs. One might ask if all this trouble was really worth it.

To our knowledge, there have been two varieties of successful approaches to magnetic transport of ultracold atoms in a vacuum system over a large distance (not including BEC on a chip experiments, which are different altogether). Our approach, using a series of coils run in sequence, was first developed in the group of Ted Hänsch in 2001 [48]. This experiment involved magnetic transfer of atoms over 33 cm and around a 90° bend using a series of nine transfer coil pairs.

Another approach, developed in Eric Cornell's group at JILA, involves using a track-based system that physically moves a coil pair along a track on the optical

table [25]. A hybrid approach is used in the group of Carl Wieman at JILA, which includes a moving track, a 90° bend, and a series of transfer coils [52].

The track-based moving coil system has its merits and is worth comparing and contrasting to our system. We have heard that the moving coil system is easy to use, robust, and simple to set up. At JILA, it worked on the first attempt [25]. The ease of use of the moving coil system makes it appear rather advantageous compared to our machine. However, the moving coil system is not without its disadvantages. It places a moving mechanical system on the optical table, which can potentially have repercussions for vibration-sensitive equipment such as laser locks. It is also large, bulky, and restricts optical access to the MOT cell and science cell. Finally, because the same coil pair and associated mount need to translate from the MOT cell to the science cell, optical access to the science cell will be particularly blocked in this design.

One of the main advantages of our design is the large amount of optical access to the science cell from five directions, which will be highlighted in the description of the TOP trap in Section 4.2.1. Setting up complex experiments such as 3-D optical lattices while imaging from multiple directions and using an optical trapping beam is possible with our open geometry design. The biggest disadvantage to our current system is the MOSFET lifetime. We continue to blow up MOSFETs, particularly the DC TOP MOSFET and occasionally one of the switching MOSFETs. This is something that can possibly be alleviated by increased or more efficient cooling, waiting longer between runs, or, in the case of the DC TOP MOSFET, distributing the power dissipation over two MOSFETs.

CHAPTER 4

BEC FORMATION AND IMAGING

4.1 Introduction

Chapters 2 and 3 describe the first two steps in our BEC formation process: (1) laser cooling and magnetic trapping in the MOT cell; and (2) magnetic transfer of atoms from the MOT cell to the science cell. This chapter describes the final step in the BEC formation process: evaporative cooling of atoms in the science cell. After transfer into the science cell, the atoms are held in a Time-averaged Orbiting Potential (TOP) trap, described in Section 4.2. The atoms are then evaporatively cooled in the TOP trap until a BEC is formed; this process is described in Section 4.4. The methods used for imaging the condensate and techniques used for image processing are described in Section 4.5. The final characteristics of our BEC are presented in Section 4.6; and Section 4.7 summarizes our complete BEC formation sequence.

4.2 TOP Trap

In order to evaporatively cool atoms to the BEC transition in a magnetic trap, the atoms cannot be held in a quadrupole magnetic field. This is because as atoms get colder during the evaporation process, more atoms will occupy the region of the potential minimum (the $|\vec{B}| = 0$ point) and be ejected from the trap by Majorana losses [47]. In order to prevent this problem, two main approaches are most commonly used to create a BEC in a magnetic trap, the Time-averaged Orbiting

Potential (TOP) trap [16, 20, 53] or the Ioffe-Pritchard (IP) trap [17, 54, 55].

We use a TOP trap consisting of a pair of anti-Helmholtz coils with an axis of symmetry along the vertical direction, referred to as the DC TOP coils, and two orthogonal pairs of Helmholtz coils with an axis of symmetry in the horizontal plane, referred to as the AC TOP coils. The TOP trap provides a simple method for creating an axially symmetric trapping potential. Also, it is relatively straightforward to elongate the TOP trap in one of the radial directions and rotate this elongated trap. This is one way of nucleating a vortex lattice in the BEC, a procedure that will be described in Section 5.4.6. We have chosen to use a TOP trap because of its vertical axial symmetry, and the fact that the most tightly confining axis is in the vertical direction. This makes it easier to make ‘pancake-shaped’ condensates that can easily be manipulated with light in a 2-dimensional plane.

4.2.1 Physical layout of TOP trap

The TOP trap is an axially symmetric trap created by the addition of the fields from the two DC TOP coils and the four AC TOP coils. The DC TOP coils are concentric with the final transfer coils and held on the same copper mount, but lie closer to the science cell. The AC TOP coils are mounted to aluminum plates on all four sides of the science cell. A photograph of the TOP trap showing a side view and top view is shown in Figure 4.1. A table showing the locations and other relevant information about the coils surrounding the science cell is shown in Table 4.1.

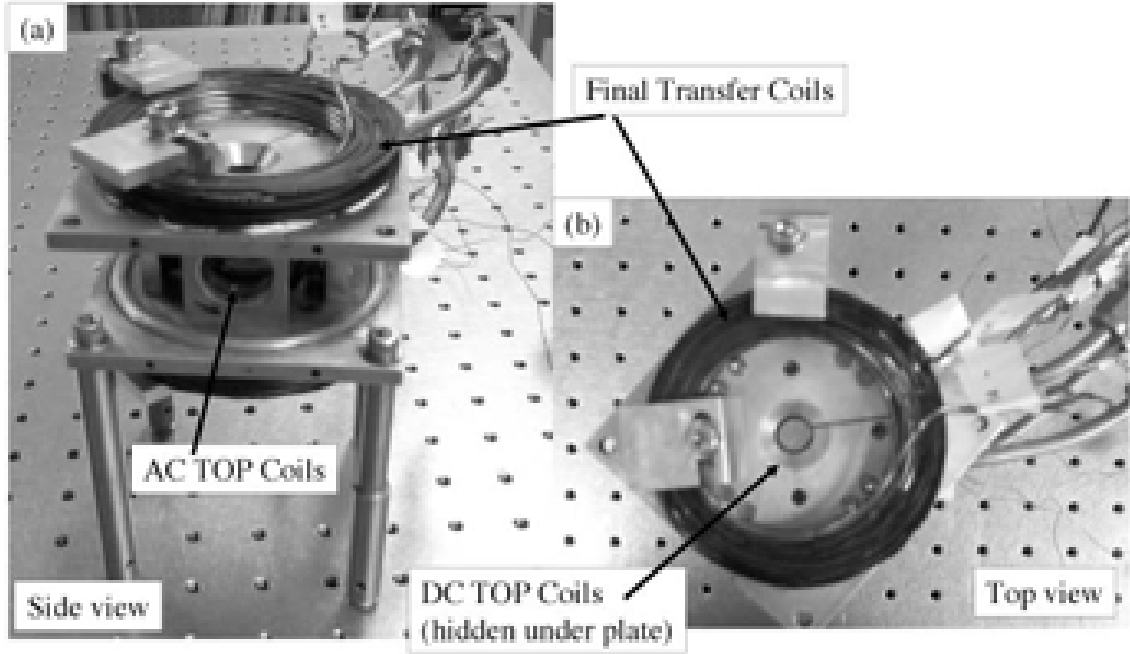


Figure 4.1: Photograph of TOP trap. (a) Side view of the TOP trap and mount. (b) Top view of the TOP trap. The final transfer coils are mounted above and below the water-cooled copper plates, and are indicated by arrows. Four aluminum plates with holes for horizontal optical access to the science cell join the upper and lower copper plates. On the inside of each of these four aluminum plates sits one of the AC TOP coils, one of these is indicated with an arrow. Two of these four aluminum plates are electrically isolated from the upper copper plate, and the other two are electrically isolated from the lower copper plate; this provides us with four (rather than eight) contact points between the four aluminum plates and the two copper plates, allowing for cooling of the aluminum plates but minimizing eddy currents. The slot through the upper copper plate that prevents eddy current flow around the central hole is visible in (b). The DC TOP coils, obscured from view, are epoxied to the inside of the upper and lower copper plates around a hole used for vertical optical access to the science cell. The electrical connections for the final transfer coils, the DC TOP coils, the AC TOP coils, the RF coils, and the copper tubing connections for the water cooling all point off in the same direction. The entire mount fits around the science cell.

QUADRUPOLE COILS	Rinner	Router	zclose	zfar	AWG	Turns		N	R (pair)	L (pair)	Calibration G/cm/A at BEC
						axial x radial					
coil 13	2.2 cm	4.05 cm	4.02 cm	5.46 cm	12	7x9		63	127 m Ω	503 μ H	
coil 14	3.25 cm	4.89 cm	2 cm	2.82 cm	12	4x8		32	83 m Ω	166 μ H	69 A \leftrightarrow 150 G/cm
DC TOP coils	0.6 cm	1.5 cm	1 cm	1.65 cm	16	5x7		35	60 m Ω	53 μ H	20.1 A \leftrightarrow 300 G/cm

BIAS COILS	Rinner	Router	xclose	xfar	AWG	Turns		N	R (pair)	L (pair)	Calibration G/A at BEC
						axial x radial					
AC TOP coils	1.1 cm	1.51 cm	1.86 cm	2.47 cm	24	12x8		96	1.3 Ω	493 μ H	3.85 A \leftrightarrow 50 G

Table 4.1: Information about the coils surrounding the science cell is tabulated in two sections. The ‘QUADRUPOLE COILS’ section describes transfer coil pair 13, transfer coil pair 14 (the final transfer coil pair), and the DC TOP coils. The ‘BIAS COILS’ section describes the AC TOP coils. The inner radius R_{inner} and outer radius R_{outer} of each coil are tabulated, as are z_{close} and z_{far} , defined as the z distance from the center of the trap to the closest and farthest part of the coil. The wire gauge AWG, axial and radial number of turns, total number of turns N , resistance R , inductance L , and coil calibrations are given. Similar information is provided for the AC TOP coils, where the coil axis of symmetry is now along the x axis, and the calibration is in G/A for these Helmholtz coils.

Because of the long evaporation times, typically around 70 seconds, the DC TOP coils heat up to a temperature that is hotter than any other coils used in the transfer process. This could pose a problem with overheating of the BEC cell, since the coils lie only a few mm from the glass cell. However, forced air cooling from a directed fan alleviates the overheating.

Optical access to the science cell

Because we believe that the large amount of optical access to the science cell is one of the principal advantages of our experimental system, it will be described in detail in this section. To highlight this, a to-scale rendering of the TOP trap mount and nearby coils is shown in Figure 4.2.

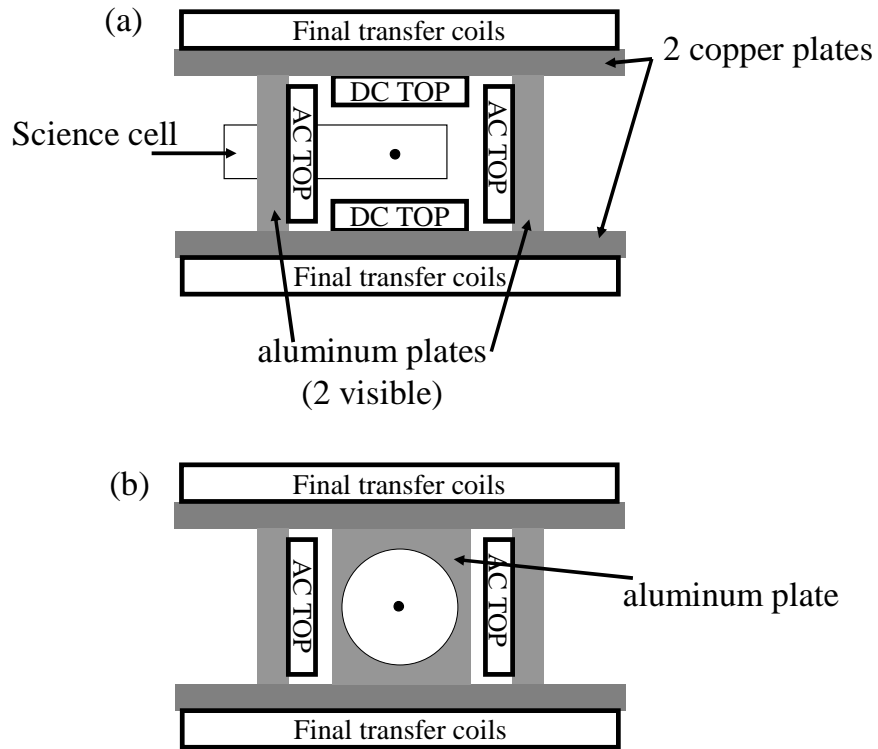


Figure 4.2: Schematic of the TOP trap mount and nearby coils, highlighting optical access to the science cell. (a) Side view of the final transfer coils, DC TOP coils, AC TOP coils, science cell, and BEC location. The two copper plates and two of the four aluminum plates are shown in gray. (b) A side view of the aluminum plate, with a hole cut for optical access, is shown.

The DC TOP coils have an inner radius of 6 mm, an axial thickness of 7.9 mm, and the closest part of the coils lie 4 mm from the top and bottom of the science cell. The DC TOP coils are epoxied to a copper plate around a 12.7 mm diameter hole that allows for vertical optical access to the science cell. The distance from the BEC to the copper plate is 18 mm. The AC TOP coils have an inner radius of 11 mm, an outer radius of 16 mm, and a thickness of 6.9 mm. They are epoxied to an aluminum plate around a 22 mm diameter hole that lies 18.6 mm from the BEC.

A useful figure of merit that characterizes the amount of light collected by an optical system is the $f/\#$, conventionally defined as $f/\# = f/D$ where f is the focal length of a collecting lens that is placed a distance f from an object and D is the diameter of the lens [56]. This is the traditional definition given for infinite-conjugate imaging systems, and is a useful measure for determining the light-collection efficiency of an optical system. We will modify this definition somewhat for our finite-conjugate system in order to quantify it. We will use $f/\# = z/D$, where z is the distance from the object (the BEC) to the limiting aperture in object space (in theory we could place a lens there but in practice it is usually a few mm behind this aperture) and D is the diameter of that aperture. Using this expression, the $f/\#$ from the top and side are:

$$f/\#_{top} = \frac{18 \text{ mm}}{12.7 \text{ mm}} = 1.417 \quad (4.1)$$

$$f/\#_{side} = \frac{18.6 \text{ mm}}{22 \text{ mm}} = 0.85 \quad (4.2)$$

With our open geometry system we achieve $f/0.85$ imaging from three horizontal directions and $f/1.417$ imaging from two vertical directions. Despite the fact that the sixth direction faces the transfer tube, we still make use of it by sending the horizontal absorption imaging beam to the BEC from that direction. There is also

the possibility of using laser beams to access the science cell that are oriented in the horizontal plane at 45° to the TOP trap mount. Although the $f/\#$ here is too poor to use these axes for imaging, beams can access the science cell through one of the ~ 3 mm wide gaps in between the four aluminum plates.

4.2.2 Electronics used in TOP trap

DC TOP coils

The DC TOP coils operate on a circuit conceptually similar to the transfer circuit, described in Section 3.3.5. The coils use the same power supply, there is one IXYS 180N10 MOSFET, a fly-back diode, and Hall Probe in the DC TOP MOSFET box. A schematic of the circuit is shown in Figure 4.3. This circuit differs from the transfer circuit of Figure 3.5 in three ways: (1) this circuit controls only one pair of coils (the DC TOP coils), rather than five; (2) only one power MOSFET is used, rather than using one switching MOSFET and two ramping MOSFETs to operate each coil pair; and (3) there is an additional inductor in series with a feedback resistor, as shown in Figure 4.3. Other than these differences, the principles of operation of the circuit are similar to those of the transfer circuit, described in Section 3.3.5.

Using only one MOSFET in this circuit is the principal drawback in this design, as the DC TOP MOSFET is the most frequently blown-up MOSFET in our experiment, despite the fact that it is the only MOSFET that receives forced air cooling by a directed fan. We are currently installing a new circuit that includes two power MOSFETs, two Hall Probes, and two separate feedback loops to operate the DC TOP coils. There are numerous safety interlocks on the DC TOP coil temperature, integrated current, and instantaneous current, as described in Section 3.3.8.

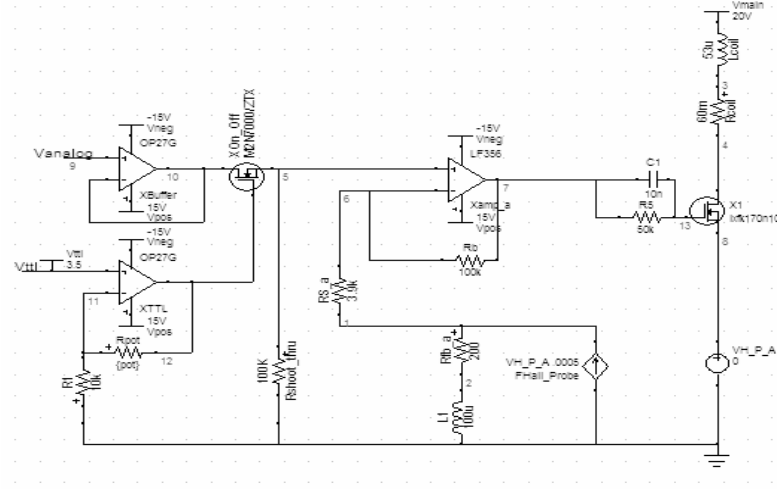


Figure 4.3: Schematic of the DC TOP circuit.

AC TOP coils

The AC TOP coils provide a rotating radial bias field that acts to shift the $|\vec{B}| = 0$ point away from the origin to a circle in the horizontal plane referred to as the circle of death R_{cod} [20].

$$R_{cod} = \frac{B_{bias}}{\partial B / \partial r} \quad (4.3)$$

The time average of this effect is the creation of an harmonic potential with a minimum at the origin. Atoms that have enough total energy to access the outer reaches of this time-averaged potential will experience a $|\vec{B}| = 0$ point and be ejected from the trap due to Majorana losses.

A schematic showing the hardware and electronics used to operate the AC TOP coils is shown in Figure 4.4. A Crown XLS402 power amplifier is used to drive the AC TOP coils, and an SRS function generator is used to create the 2 kHz sine wave that is sent to the Crown amplifier.

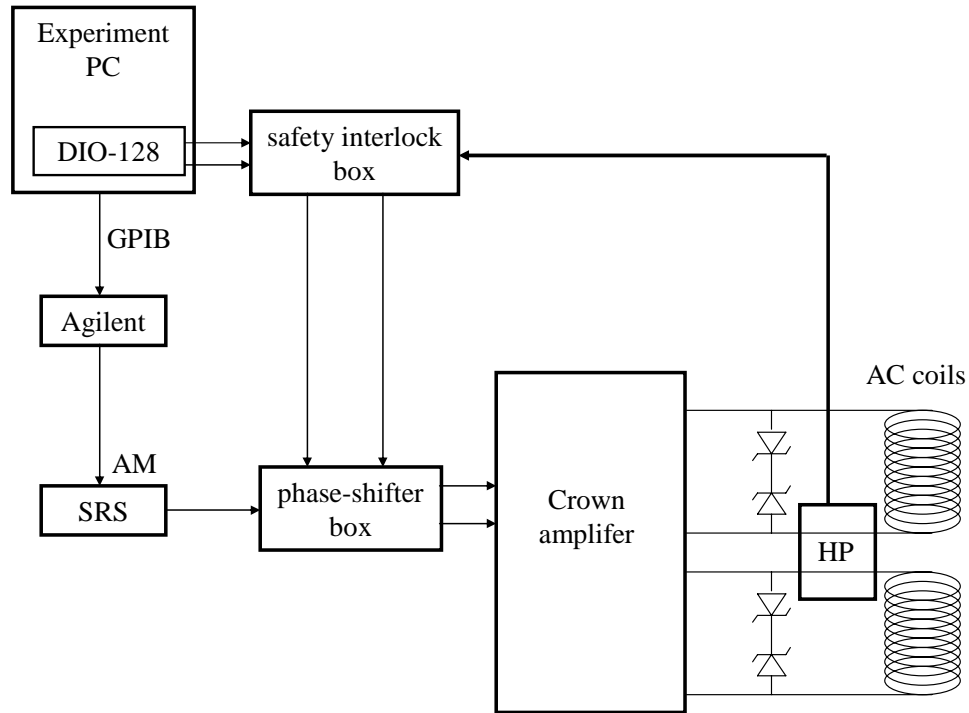


Figure 4.4: Schematic of the AC TOP coils driving circuit. Two orthogonal pairs of coils are connected to the output of the Crown amplifier. There are two pairs of oppositely-oriented Zener diodes placed in parallel with each of the two pairs of coils. A hall probe (HP) reads the amount of AC current flowing simultaneously through both pairs of coils, and sends this signal to the safety interlock box. If the amount of current is too high, the safety interlock box will switch off the two TTL signals going to the phase-shifter box, shutting off the current flow from the Crown.

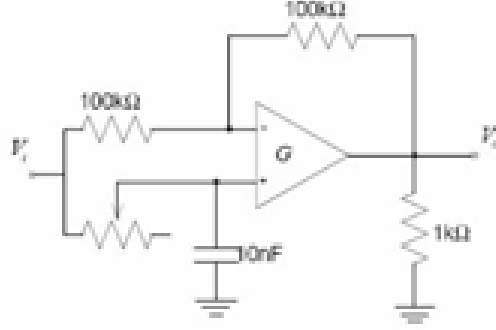


Figure 4.5: Schematic of the phase-shifter circuit. The circuit uses an OP27 op amp and produces an output V_o that is a phase-shifted version of the input V_i , based on the resistance of the 20 k Ω potentiometer.

Over the ~ 70 second evaporation process, the amplitude of the rotating radial bias field decreases from 41 G to 5 G. The amplitude of this waveform is created in software on the experiment PC and loaded onto an Agilent 33120A arbitrary waveform generator through a GPIB connection. The Agilent output signal is applied to the Amplitude-Modulation (AM) input of an SRS DS345 function generator to produce an AM-modulated 2 kHz sine wave.

The role of the phase-shifter box is to convert its sine wave input into two outputs: an identical version of the sine wave input, and a 90° phase-shifted version of its input. The phase-shifter circuit operates on a circuit similar to that shown in Figure 4.5.

The phase-shifter box has one analog input (from the SRS) and two logic inputs, one for each channel of the Crown. When both logic inputs are high, the phase-shifter box outputs a sine wave identical to its input on one channel, and a 90° phase-shifted version of this signal on the other channel. These signals are sent to the two inputs on the Crown amplifier. The two connections on each channel of the

Crown's output are connected to either end of each of the two pairs of AC TOP coils.

There are two kinds of safety interlocks on the Crown amplifier, but neither are as robust as the safety interlocks on the Agilent power supply, where an external TTL signal can instantly disable the supply. Because the Crown does not have this function, we had to invent ways of preventing unwanted current from flowing in case of a computer or electronics error. The first thing we did was to apply two back-to-back -68 V zener diodes across the output of each channel of the Crown, in parallel with the AC TOP coils. These act to protect the amplifier from a voltage spike, such as what would occur if the power were suddenly lost. If a voltage spike of more than 68 V is generated, the zener diodes turn on and shunt current through the diodes instead of back into the amplifier.

The second safety interlock monitors how much current is flowing through the AC TOP coils with a Hall Probe and disables the two logic inputs to the phase-shifter box if the current is too high. AC current through both pairs of coils passes through the same Hall Probe, which sends a signal to the safety interlock box. The safety interlock box rectifies this signal, integrates it, and if the integrated value is too high, turns off the two logic signals sent to the phase-shifter box, stopping current flow. There is a relay in the safety interlock box that prevents further current flow until a front-panel switch is depressed.

4.2.3 Transfer into TOP trap

Immediately after transferring atoms into the science cell, we apply a short pulse of light near-resonant with the $|F = 2 \rightarrow F' = 3\rangle$ transition to drive away any wayward

atoms that are still magnetically trapped in the $|F = 2\rangle$ state in the science cell due to imperfect optical pumping into $|F = 1\rangle$ in the MOT cell. This pulse, referred to as the ‘kill pulse’, is 5 ms long and the process is not very dependent on laser intensity or detuning. Using the kill pulse will increase the number of atoms in the final $|F = 1, m_F = -1\rangle$ BEC by removing any $|F = 2\rangle$ atoms, which only provide collisions that are deleterious to the evaporative cooling process.

After the kill pulse, the $|F = 1\rangle$ atoms are still trapped in a quadrupole field created by the final transfer coil pair, coil pair 14, at an axial field gradient of 180 G/cm. The atoms are then transferred into a quadrupole field created by the DC TOP coils, concentric with coil pair 14. This is done by ramping the current in coil pair 14 down to zero while ramping up the DC TOP coils from zero to 180 G/cm over 100 ms. The atoms are then transferred into the TOP trap by switching the axial field gradient in the DC TOP coils from 180 G/cm to 300 G/cm and simultaneously turning on the 2 kHz rotating radial bias field to 41 G.

We have held atoms in the 180 G/cm quadrupole trap in the science cell for as long as 8 minutes, and were limited in a measurement of the TOP trap lifetime due to heating of the DC TOP coils.

4.3 RF Coils

We use a radio-frequency (RF) magnetic field in the region from 4 – 70 MHz for the primary evaporative cooling of the atomic cloud; this occurs in addition to the TOP-induced evaporation caused by decreasing the radius of the circle of death. This RF field causes transitions from the magnetically trapped $|F = 1, m_f = -1\rangle$ level to the untrappable $|F = 1, m_f = 0\rangle$ and $|F = 1, m_f = 1\rangle$ levels, thereby ejecting

atoms from the TOP trap. The two RF coils are each made up of one single loop of magnet wire, above and below the BEC cell, wired in Helmholtz configuration. The RF coils, which are wrapped around the outside of the DC TOP coils, have a diameter of 3 cm and lie ~ 1 cm from the plane of the BEC; only the glass surface of the science cell lies between the RF coils and the BEC.

The desired RF frequencies are created with an Agilent E4400B RF synthesizer. This signal is then sent through a Mini-Circuits ZYSW-2-50DR RF switch before being amplified by an OPHIR 5303055 RF amplifier, then sent to the RF coils.

4.4 Evaporative Cooling

Evaporative cooling is the process by which the hottest atoms are ejected from the trap and the remaining atoms are allowed to rethermalize at a lower temperature [57, 58, 59]. This process occurs while the atoms are held in the TOP trap in the science cell. The evaporative cooling process will eventually eject $\sim 99\%$ of the atoms from the TOP trap, but is the process by which the remaining atoms are cooled to the critical temperature necessary to reach the BEC transition.

The evaporation process occurs in two phases, described in the following two sections. In brief, Phase I occurs in the tight TOP trap and cools the atoms to a point just above the BEC critical temperature. Then, the axial field gradient is reduced, placing the atoms in a weakly confining potential that allows us to generate spatially larger BECs. The Phase II evaporation, which cools the atoms through the BEC critical temperature, occurs in this weakly-confining TOP trap.

4.4.1 Initial evaporation in the tight TOP trap

Phase I evaporation occurs over a period of 72 seconds in the tight TOP trap with a magnetic field gradient of 300 G/cm. In the first 2 seconds the bias field is held constant at 41 G and the RF frequency is reduced from 70 MHz to 57 MHz. This fast sweep acts to eject the hottest atoms from the trap. Over the next 58 seconds the RF frequency ramps down from 57 MHz to 7 MHz, and the amplitude of the rotating bias field ramps down from 41 G to 5 G. During this part of the evaporation sequence, the RF frequency changes along with the bias field in such a way that the RF frequency is always ejecting atoms that lie directly at the circle of death. All of the ramps used in our evaporation scheme are exponentially decreasing ramps with an adjustable time constant. The 58 second ramps described above follow an exponential decay with a 100 second time constant.

For the rest of the evaporation sequence the bias field is left at 5 G and all additional evaporation is done solely with the RF frequency. In the next 12 seconds the RF frequency is brought from 7 MHz to 4.5 MHz, this cools the atoms to a point just above the BEC critical temperature. This 72 second sequence concludes the Phase I evaporation sequence in the tight TOP trap.

4.4.2 Evaporative cooling in a weakly-confining TOP trap

The atoms are then moved to the gravity-sagged TOP trap by reducing the axial magnetic field gradient from 300 G/cm to 55 G/cm over 2 seconds, decreasing the radial trapping frequency from 40 Hz to 7.4 Hz. This reduction in field strength uses a nonlinear current ramp that approximates a linear shift in the $|\vec{B}| = 0$ point over the 2 second sag time. The atoms sag 0.6 mm due to the larger role played by

the gravitational potential in the weak TOP trap compared to the tight TOP trap [20]. During the sag process the RF frequency is increased to 5 MHz to prevent unwanted additional evaporative cooling.

Phase II evaporation occurs in the gravity-sagged TOP trap with an axial field gradient of 55 G/cm and radial bias field of 5 G. Because the atoms no longer lie at the center of the TOP trap coils, the Zeeman shifts are different at the top and bottom of the cloud, and evaporation occurs primarily closer to the bottom (the south pole) of the atomic cloud [60]. This reduced-dimension evaporation is less efficient than the 2-D (around the equator) evaporation afforded by evaporation in a tight TOP trap. Phase II evaporation reduces the RF frequency from 5 MHz to 4.7 MHz over 10 seconds, using a 2 second exponential decay time constant, after which a pure BEC is observed.

Plots of the bias field strength and RF frequency vs. time used in the above evaporation sequence are shown in Figure 4.6. Figure 4.6 (a) shows the bias field ramp vs. time over the course of the Phase I and Phase II evaporation steps. Figure 4.6 (b) shows the RF frequency ramp vs. the same time. Figure 4.6 (c) shows the bias field and RF frequency plotted together, with the RF evaporation point converted to G to show both the RF evaporation point and the TOP-induced evaporation point on the same scale.

To understand how to plot both quantities on the same scale, consider the following example¹. If the instantaneous $|\vec{B}| = 0$ point happens to be at $x = R_{cod}$, the point in the cloud that experiences the largest magnetic field will be at $x = -R_{cod}$, where the magnitude of the field is $B_{max} = 2 \cdot \partial B / \partial r \cdot R_{cod} = 2B_{bias}$. Knowing that

¹For addition information, see the lab notebook entry on 3/25/2005.

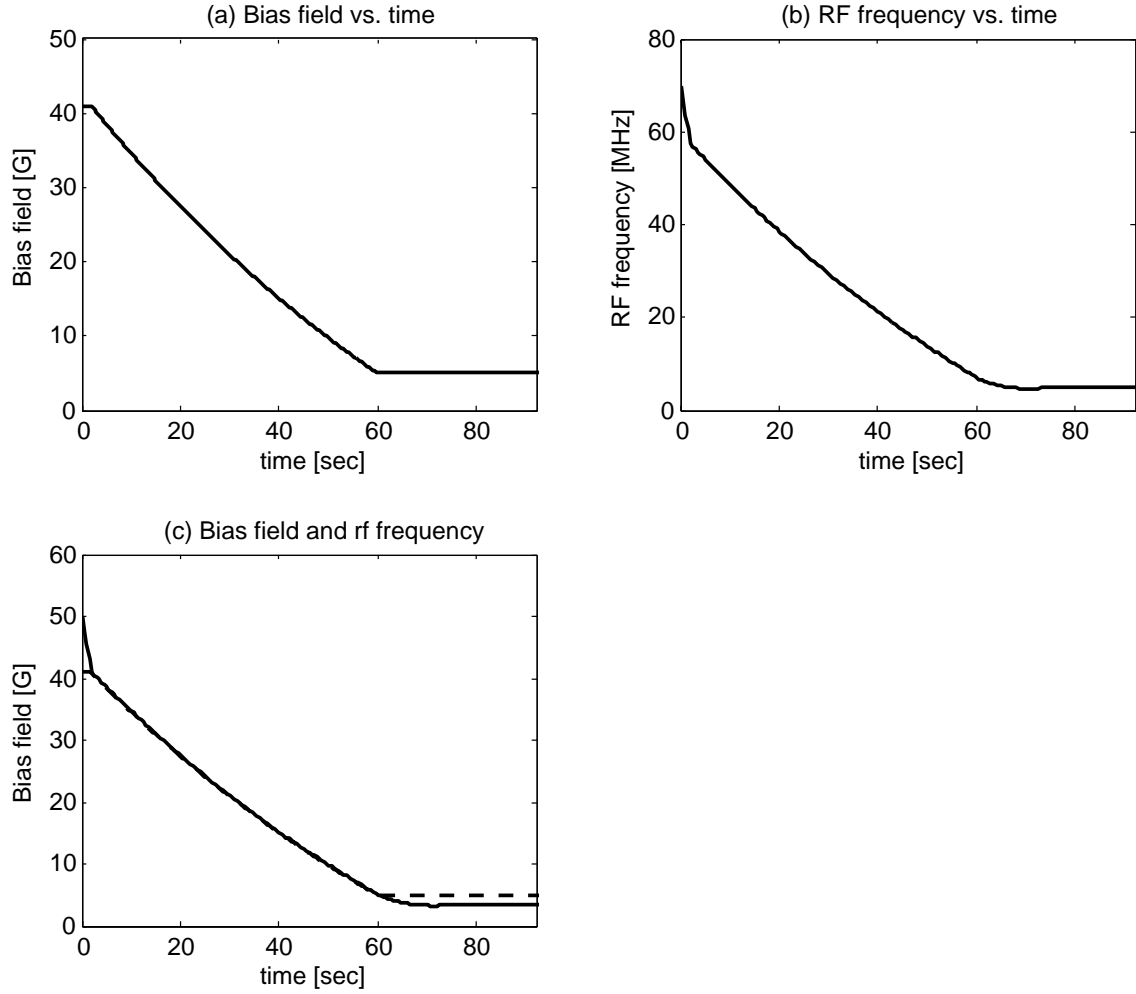


Figure 4.6: Evaporative cooling sequence. (a) Shown is the bias field [G] vs. time [s]. (b) Shown is the RF frequency [MHz] vs. time [s]. (c) Shown is the bias field and RF frequency plotted together, with the RF frequency shown as a solid line and the bias field shown as a dashed line. The gradient field from the DC TOP coils is 300 G/cm until time $t = 72$ s, after which it ramps down to 55 G/cm over 2 seconds.

the Zeeman splitting between the $|F = 1, m_f = -1\rangle$ and $|F = 1, m_f = 0\rangle$ states is 0.7 MHz/G for ^{87}Rb [42], the appropriate RF frequency f needed to evaporate away atoms based on the bias field B_{bias} is $f = 2 \cdot B_{bias} \cdot 0.7 \text{ MHz/G}$. In Figure 4.6 (c) it is clear that the RF frequency keeps pace with the TOP-induced evaporation point for most of the evaporation sequence, until the end of the sequence when it alone continues to decrease and acts to evaporate atoms from the trap.

4.5 Imaging

100% of the data that comes from our experiment results from the analysis of images of atomic clouds. Because of this, the ability to take images of these atomic clouds and extract useful information from them is a major component of our experiment. We have one computer dedicated to image acquisition and analysis. This imaging PC (shown in Figure 2.1) communicates with a Princeton Instruments/Acton PIXIS 1024BR CCD camera via a USB connection, and the camera receives a TTL trigger from the experiment PC via a digital line the DIO-128 board's Port A. The following sections describe the design and layout of our imaging systems, a description of absorption and phase-contrast imaging, and a summary of our image processing routine.

4.5.1 Overview, physical layout of imaging systems

Atoms are trapped in the science cell in a TOP trap that is axially symmetric with the axis of symmetry aligned along the direction of gravity. The vortices created in our experiment are a signature of orbital angular momentum about this axis, and will thus be visible only by imaging along the vertical direction. Our experiment

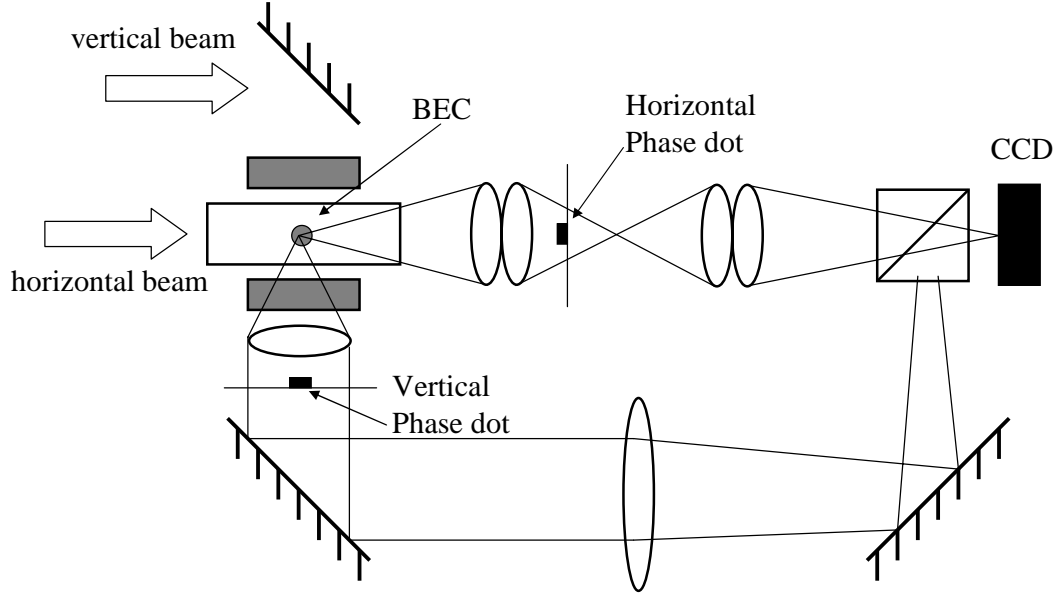


Figure 4.7: Layout of horizontal and vertical imaging systems. The horizontal imaging system contains two sets of paired achromats, and includes an intermediate focal plane between the achromat pairs. The horizontal probe beam focuses onto the plane of the horizontal phase dot. The vertical imaging system contains two imaging achromats, and has a collimated intermediate image space. The vertical probe beam focuses onto the plane of the vertical phase dot. Both imaging systems have an optical magnification of 5.36.

includes a vertical and horizontal imaging system, for reasons described below.

Imaging along multiple axes

A schematic showing the layout of the vertical and horizontal imaging systems is shown in Figure 4.7. The BEC is imaged onto the CCD camera via the four lenses that comprise the horizontal imaging system, and is also imaged onto the CCD camera via the two lenses of the vertical imaging system.

The horizontal system uses an imaging beam that passes through the MOT cell, travels 80 cm down the transfer tube, and exits through the end port of the science

cell, passing through two pairs of paired achromats on its way to the CCD camera. The vertical imaging beam passes through the two 1 mm thick glass surfaces of the science cell, which are separated by 10 mm. Because these glass surfaces are close to parallel, the beam undergoes multiple reflections within the science cell that put visible interference fringes on the beam. When imaging a small BEC using phase-contrast imaging, these fringes can significantly degrade image quality. The horizontal axis does not suffer from any of these multiple reflections due to the glass science cell. Additionally, the use of only two achromats on the vertical imaging system rather than the two pairs of paired achromats (four total) on the horizontal axis produces a slightly larger diffraction-limited spot size on the vertical system. The sum total of these effects has meant that the images on the vertical system have never been as high in image quality as those achievable on the horizontal system. We typically use the horizontal system for in-trap phase-contrast imaging of the cloud to characterize the BEC, and the vertical imaging system for absorption imaging of the cloud after ballistic expansion.

For phase-contrast imaging on either axis, a phase dot is slipped into or out of the focus of the probe laser beam in order to shift the phase of the laser light by $3\pi/2$ relative to the BEC image light, which is spatially much larger than the 100 μm diameter phase dot. The 100 μm diameter phase dot was made using the Maskless Lithography Tool at the College of Optical Sciences; this machine will be described in Section 5.4.3 on Page 140.

Both imaging systems have an optical magnification of 5.36, which was measured experimentally on the horizontal axis by calibrating the distance a cloud of atoms fell vertically due to gravity when released from the trap. The vertical axis was then

cross-calibrated against the horizontal axis by ensuring that the cloud sizes on both axes were the same when both systems were in focus. Each system was focussed by using on-resonance absorption imaging to image as small a cloud as possible immediately after release from a tight TOP trap. On both axes the first lens in the imaging system (lens pair on the horizontal system) was placed on a translation stage. The lens position was optimized to produce the smallest size atom cloud in the image plane. By tuning a few linewidths on either side of resonance, lensing of the probe laser beam by the BEC is visible (see Ref. [23] Section 4.1.1). The high optical depth of a small BEC can cause an off-resonant probe beam to refract through the BEC, which acts like a lens. The sign of the lensing caused by the BEC will change on either side of the focus position, and analysis of the defocussed clouds can help to set the focus position correctly.

Optical design

Both the horizontal and vertical imaging systems were designed using the optical design software ZEMAX, which allowed us to design diffraction-limited optical systems. The layout for the horizontal imaging system is shown in Figure 4.8. A spot diagram showing the rays traced through the horizontal system for a $100\text{ }\mu\text{m}$ diameter BEC is shown in Figure 4.9.

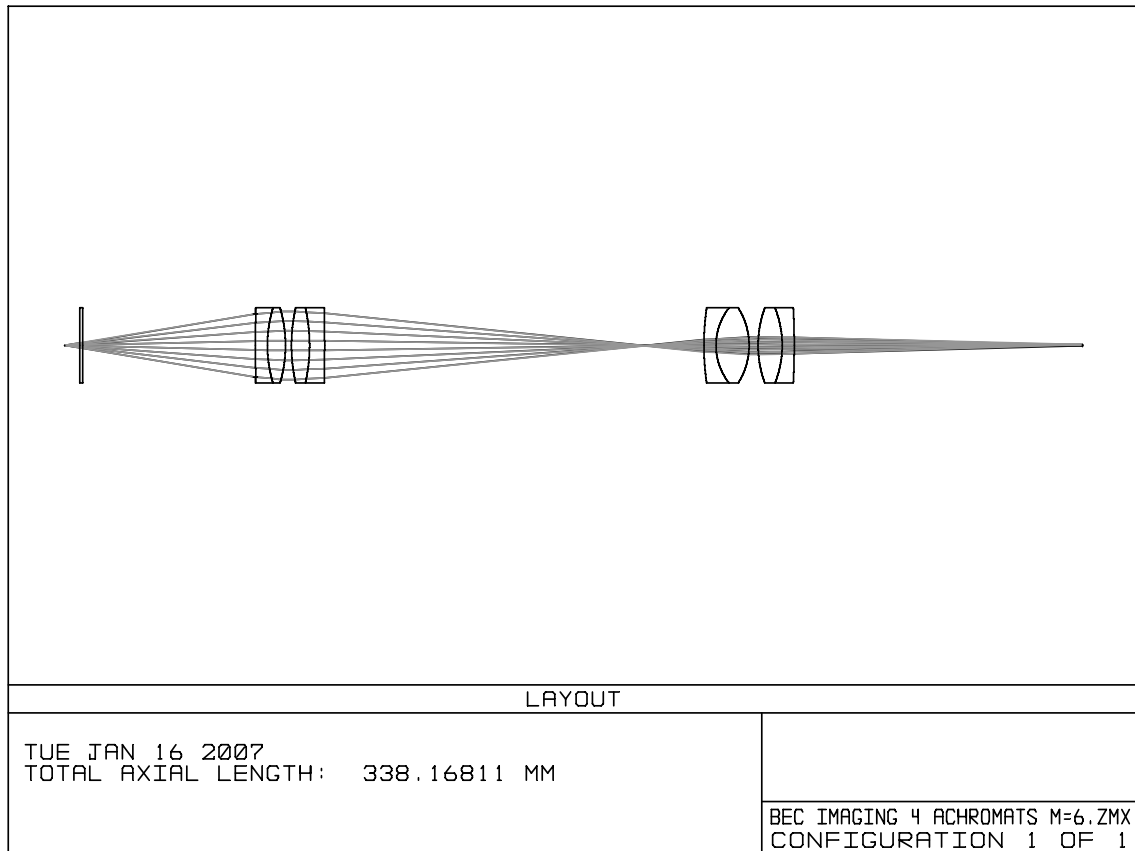


Figure 4.8: Layout of horizontal imaging system, generated using ZEMAX. The BEC is imaged through a 1 mm thick plate of glass (a simulation of the glass science cell), through 4 achromats, and onto the CCD camera. The lenses used are all Edmund Optics TECH-SPEC Near-Infrared Achromats with focal lengths of $f = 75$ mm, $f = 100$ mm, $f = 35$ mm, and $f = 60$ mm, from left to right.

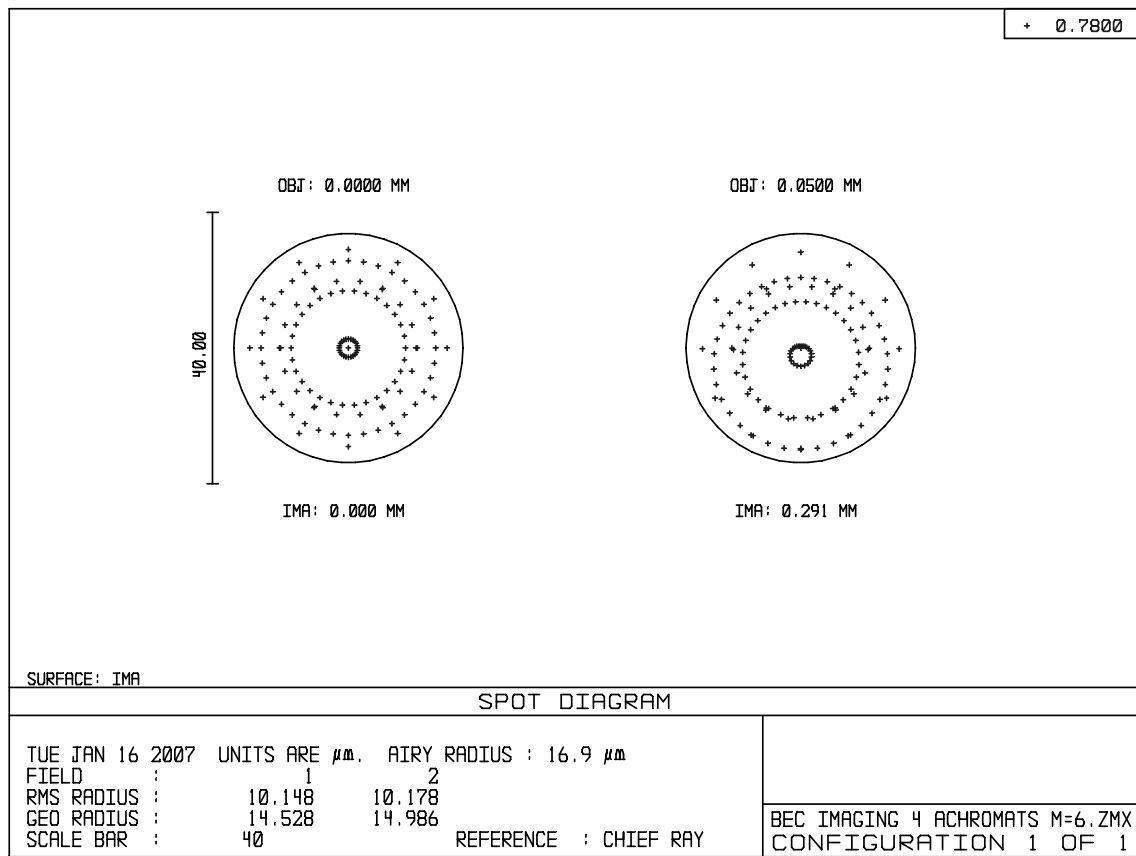


Figure 4.9: Spot diagram of the horizontal imaging system, generated using ZEMAX. The spots from the marginal and chief rays all fall clearly within the Airy disk of radius 16.9 μm , indicating a diffraction-limited optical system.

4.5.2 Absorption imaging

We use absorption images taken on the vertical axis to image the cloud after a period of expansion, as described below. It is necessary to allow the cloud to expand in order to optically resolve vortex cores, which would not be visible using in-trap phase-contrast images because they are smaller than the optical diffraction limit.

In order to image the vortex cores in our experiment we need to allow the cloud to expand in size by a factor of ~ 5 . The atomic cloud can only fall in free space for about 30 ms before it hits the bottom of the science cell 5 mm away; this is not enough time for the cloud to expand enough for vortex cores to be observable. In addition to the fact that using a short ballistic expansion time would not allow the cloud to expand enough, it would also place the cloud at a different vertical position, requiring a change in lens position to focus the expanded cloud on the CCD camera. We needed to find a way of allowing for ballistic expansion times of up to ~ 70 ms while keeping the cloud in place. We solved this problem by using a levitation coil during the expansion phase.

Levitation coil

Our absorption imaging expansion scheme incorporates a levitation coil² that operates in conjunction with the DC TOP coils to provide a field gradient that is similar to that obtained in a QUIC trap [61]. The difference is that in our case the single levitation coil is oriented along the axis of symmetry of the DC TOP coils rather than orthogonal to it. The basic idea of operation is that the combined field gradient provides a very weak harmonic trapping potential in the axial (gravity)

²For additional information, see the lab notebook entry on 6/5/2006.

direction centered at the position of the trapped BEC. In our case, the trapped BEC is initially held in a gravity-sagged weakly-confining TOP trap. The radial field can be very weakly trapping or anti-trapping. This is achieved when the DC TOP coils operate at a field gradient near 55 G/cm, the levitation coil produces a field near 32.4 G, and the AC TOP coils are off. After 56 ms of hold time in the combined magnetic fields of the DC TOP coils and the levitation coil, the center of the atomic cloud will not have changed in vertical position, making it still in-focus in the vertical imaging system, whereas the cloud will expand by a factor of ~ 5 radially.

The levitation coil has an inner diameter of 39 mm and is made from 18 AWG magnet wire, with 8, 8, 7, 7, 8, and 7 turns, for a total of 45 turns. We have measured experimentally that the coil calibration is 2.7 G/cm/A when the closest part of the coil is placed 2 cm from the BEC. The levitation coil operates on the same power supply and circuit topology as the MOT, transfer, and DC TOP coils. A Hall Probe monitors how much current is flowing through the levitation coil, and will inhibit the power supply if the instantaneous amount of current is greater than 15 A.

Absorption imaging sequence

The formation of a BEC occurs in a weak TOP trap in the science cell as previously described. After BEC formation, a period of 56 ms of expansion occurs with the AC TOP coils off, the levitation coil at 32.4 G, and the DC TOP coils at 55 G/cm. We create a condensate in the $|F = 1, m_F = -1\rangle$ state, but the near-resonant light used for absorption imaging drives the $|F = 2 \rightarrow F' = 3\rangle$ transition, so we

optically pump the atoms from $|F = 1\rangle$ into $|F = 2\rangle$ by using a short pulse of light, referred to as the ‘repump flash’, in resonance with the $|F = 1 \rightarrow F' = 2\rangle$ transition. The repump flash occurs in free space, using a pulse of $10\ \mu\text{s}$ duration and $\sim 1\ \text{mW}/\text{cm}^2$ intensity. We have found that longer or more intense repump flash pulses can significantly degrade the quality of absorption images, and can cause an increase in size of the atomic cloud by a factor of 2 to 3. Immediately after the repump flash pulse, we take an image by using a $20\ \mu\text{s}$ exposure with an intensity on the order of I_{sat} .

Absorption image processing

A typical vertical absorption image taken after 56 ms of expansion using the levitation coil expansion scheme is shown in Figure 4.10.

Three frames on the CCD camera are taken per data run, one with the atoms present, one without atoms, and a dark frame with no light present. Figure 4.10 (a) shows the *shadow* and Figure 4.10 (b) shows the *background*, where *shadow* and *background* both have the dark frames already subtracted off. Figure 4.10 (c) shows the raw transmission T , defined as $T = \text{shadow}/\text{background}$. Figure 4.10 (d) shows the processed transmission, which is just a centered and zoomed-in version of the raw transmission. Figure 4.10 (e) shows the raw optical depth OD_r , defined as

$$OD_r = -\ln(T) \quad (4.4)$$

for near-resonant absorption imaging. Figure 4.10 (f) shows the processed optical depth, which differs from the raw optical depth due to two nonlinear corrections.

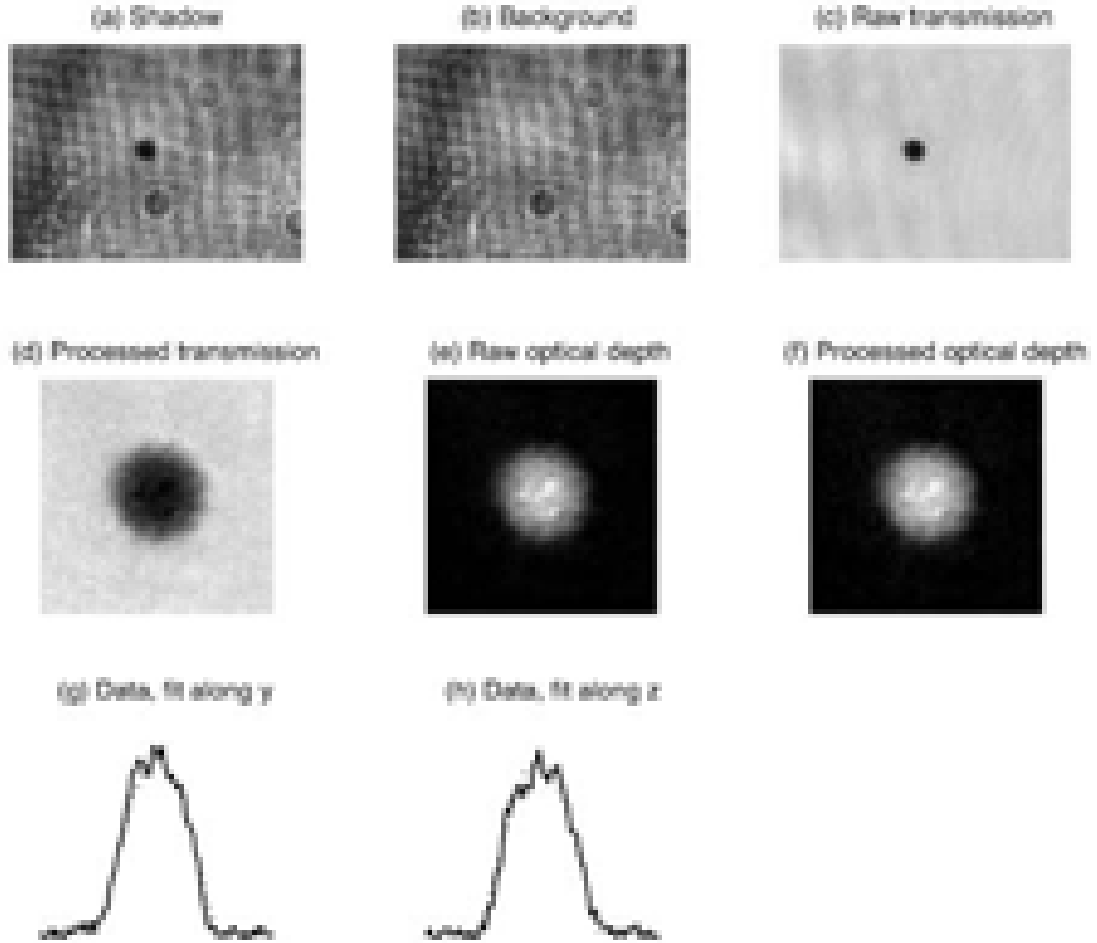


Figure 4.10: Vertical absorption image. (a) Shown is the *shadow* frame, taken with the atoms present. (b) Shown is the *background* frame, taken without atoms present. (c) The raw transmission, where the black dot represents atoms. (d) The processed transmission, where the black hole represents atoms. (e) The raw optical depth, where the white hole now represents atoms. (f) The processed on-resonance optical depth. Images (g) and (h) show the data (black line) and a corresponding fit to a Thomas-Fermi distribution (dashed line) along the y (horizontal) and z (vertical) directions, respectively. The scale on images (d) - (h) is $121 \times 121 \mu\text{m}$.

We first apply a correction to account for the maximum optical depth measurable in our system³, which we have determined to be $OD_{max} \cong 4$. Defining $\alpha = e^{-OD_{max}}$, the new value for the OD is

$$OD_a = \frac{shadow - \alpha \cdot background}{background - \alpha \cdot background} \quad (4.5)$$

The second correction accounts for saturation effects and finite detuning⁴.

$$\beta = \frac{I/I_{sat}}{1 + 4 \cdot (\Delta/\Gamma)^2} \quad (4.6)$$

$$OD_b = [OD_a + (1 - e^{-OD_a}) \cdot \beta] \cdot [1 + 4 \cdot (\Delta/\Gamma)^2] \quad (4.7)$$

We then use an image processing routine that spatially filters the value for OD_b to remove the effects of interference fringes at specific spatial frequencies. Figures 4.10 (g) and (h) show the data (from the processed optical depth) in solid lines and a Thomas-Fermi fit to the data in dashed lines along the y and z axes.

4.5.3 Phase-contrast imaging

We use phase-contrast images of the BEC taken along the horizontal axis to determine BEC characteristics such as number, temperature, and size. Because of the better image quality on this axis, we almost exclusively use the horizontal system for characterization of the atomic cloud in the science cell.

Phase-contrast imaging sequence

We typically image the atoms in the weak TOP trap or immediately after release from the trap in order to characterize the number, size, and temperature of the

³This is discussed in Ref. [23] section 4.1.

⁴This is discussed in Ref. [20] eq. 5.6.

cloud. For phase-contrast images, we use light from the probe laser that is 800 MHz red-detuned from the $|F = 1 \rightarrow F' = 2\rangle$ transition, and optical pumping is not necessary. We use a 20 μs pulse of light with an intensity of $\sim 1 \text{ mW/cm}^2$ for imaging.

Phase-contrast image processing

A typical horizontal phase-contrast image taken immediately after release from the weak TOP trap is shown in Figure 4.11.

Figure 4.11 (a) shows the *shadow* frame and Figure 4.11 (b) shows the *background*. Figure 4.11 (c) shows the raw transmission T , defined as $T = \text{shadow}/\text{background}$. Figure 4.11 (d) shows the processed transmission, which is just a centered and zoomed-in version of the raw transmission. Figure 4.11 (e) shows the raw optical depth OD_r , defined as

$$OD_r = - \left[\frac{\Gamma}{2\Delta} + \frac{I}{I_{sat}} \frac{2\Delta}{\Gamma} \right] (T - 1) \quad (4.8)$$

for far-off-resonant phase-contrast imaging. Figure 4.11 (f) shows the processed optical depth, in this case this is only a filtered version of OD_r . We use an image processing routine that spatially filters the image to remove the effects of interference fringes. Figures 4.11 (g) and (h) show the data (from the processed optical depth) in solid lines and a Thomas-Fermi fit to the data in dashed lines along the y and z axes.

4.5.4 Image processing and analysis

Images are taken by triggering a Princeton Instruments/Acton PIXIS 1024BR CCD camera. The camera has a BNC input that accepts a TTL signal to trigger the

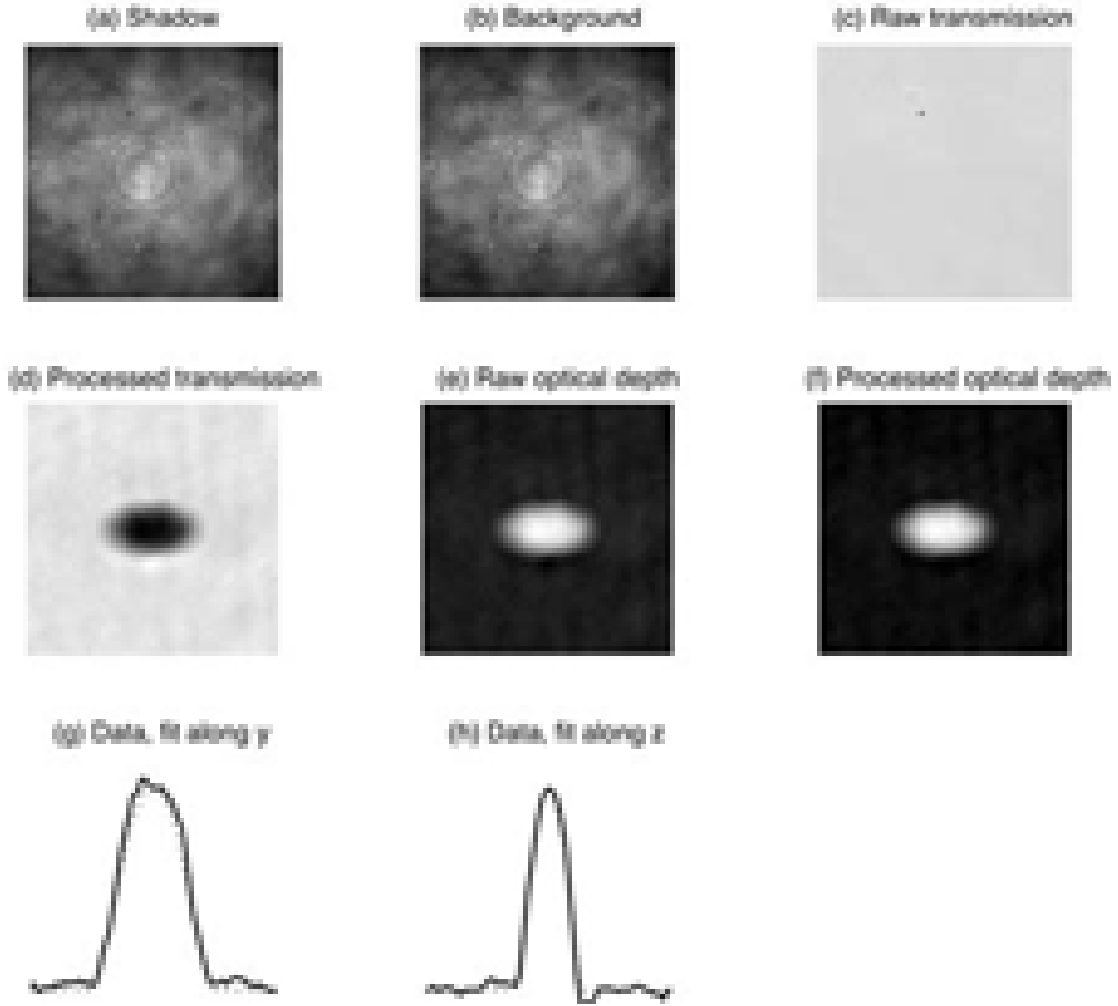


Figure 4.11: Horizontal phase-contrast image. (a) Shown is the *shadow* frame, taken with the atoms present. (b) Shown is the *background* frame, taken without atoms present. (c) The raw transmission, where the black dot represents atoms. (d) The processed transmission, where the black hole represents atoms. (e) The raw optical depth, where the white hole now represents atoms. (f) The processed optical depth. Images (g) and (h) show the data (black line) and a corresponding fit to a Thomas-Fermi distribution (dashed line) along the y (horizontal) and z (vertical) directions, respectively. The scale on images (d) - (h) is $73 \times 73 \mu\text{m}$.

camera. The software program that controls the camera is set to capture three frames, and the LabVIEW program on the experiment PC sends three triggers to the CCD camera. Three frames are taken for each data run: a shadow, background, and dark frame. The shadow frame consists of the probe laser beam passing through the BEC and onto the camera, the background consists of the same probe laser beam shining directly onto the CCD camera, and the dark frame consists of an image exposure with no light present. The dark frame is subtracted from the shadow and background frames to get rid of the effects of room lights, stray light, and bad pixels.

We have constructed an image processing program using Matlab that will process images of thermal, bimodal, or BEC clouds and provide relevant parameters. The program is adaptable for either absorption or phase-contrast imaging, and is variable for use with either the horizontal or vertical imaging systems. The basic algorithm is as follows: a 2D array labeled ‘optical depth’ is constructed, based on either the absorption or phase-contrast imaging scenarios, corrections for detuning or saturation effects are applied to the optical depth array, the array gets smoothed and/or filtered, then the array is fit to either a Bose-enhanced Gaussian distribution, Thomas-Fermi distribution, or a combination of the two to extract relevant parameters [28].

In everyday operation, we normally take one image at the start of the day at a baseline RF evaporation frequency to ensure that BEC formation is normal, comparing the number of atoms in the BEC and the size of the cloud to the baseline values. It is also often useful to take a series of images through the BEC transition to determine at what RF frequency a pure BEC is formed, as we have noticed that this value can change slightly from day-to-day.

4.6 Final BEC Characteristics

We have measured the trap frequencies in the tight TOP trap to be $\omega_r = 2\pi \cdot 39.8$ Hz radially and $\omega_z = 2\pi \cdot 110$ Hz axially, and the trap frequencies in the gravity-sagged weak TOP trap to be $\omega_r = 2\pi \cdot 7.4$ Hz radially and $\omega_z = 2\pi \cdot 14.1$ Hz axially⁵.

The final RF evaporative cooling stage in the weak TOP trap produces condensates of up to $2 \cdot 10^6$ atoms, with condensate fractions above 65% and thermal cloud transition temperatures of ~ 35 nK. The chemical potential of the BEC is $\sim k_B \cdot 8$ nK. A typical BEC has an axial Thomas-Fermi radius of $a_z \approx 18 \mu\text{m}$ and a radial Thomas-Fermi radius of $a_r \approx 34 \mu\text{m}$.

A series of four images showing the atomic cloud undergo the Bose-Einstein condensation transition is shown in Figure 4.12. Images were taken at four different times in the 20 second Phase II evaporation process, using the horizontal phase-contrast imaging system with a probe detuning of -900Γ . For each of the four images, the optical depth is shown on a $121 \times 121 \mu\text{m}$ scale. A horizontal slice of the data as well as the data overlaid with the fit are also shown. Figure 4.12 (a), taken at the start of the Phase II evaporation scheme, shows a thermal cloud that fits well to a Gaussian distribution. In Figure 4.12 (b), taken after 5 seconds, evidence of the nascent BEC starts to appear as the strong density peak in the middle of the cloud. This image was fit to a bimodal (Thomas-Fermi + Bose-enhanced Gaussian) distribution, the condensate fraction is 42%. Figure 4.12 (c), taken after 10 seconds, shows a bimodal distribution with even less of a thermal component visible; the condensate fraction here is 74%. Figure 4.12 (d), taken at the end of a longer-than-usual 20 second evaporation process, shows a nearly pure BEC with an undetectable

⁵For additional information, see the lab notebook entry on 4/11/06.

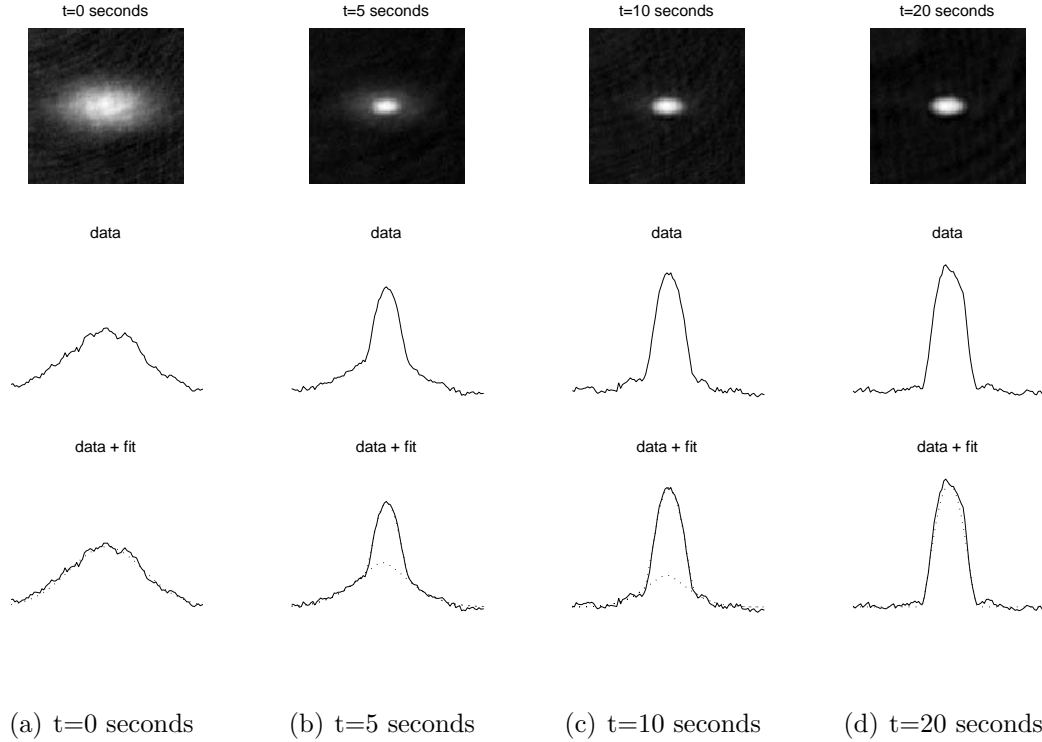


Figure 4.12: A series of four in-trap, phase-contrast images of the atomic cloud at progressive times in the RF evaporative cooling process. For each of the four times, the processed optical depth, a horizontal slice of the data, and a horizontal slice of the data alongside the appropriate fit are shown in columns. Image (a) is taken at $t = 0$ s and the data is fit to a Gaussian distribution. Image (b) is taken at $t = 5$ s and the data is fit to a bimodal (Thomas-Fermi + Bose-enhanced Gaussian) distribution. Image (c) is taken at $t = 10$ s and the data is fit to a bimodal distribution. Image (d) is taken at $t = 20$ s and the data is fit to a Thomas-Fermi distribution. The Thomas-Fermi fits are difficult to see, as they line up so well with the data. The scale on the images is $121 \times 121 \mu\text{m}$.

thermal component. This image is fit to a Thomas-Fermi distribution.

4.7 Complete Timing Sequence

The complete timing sequence used to create a BEC is shown in Figure 4.13. The numbers at the bottom of the figure correspond to the following stages:

1. All the lasers and magnetic fields are turned off momentarily prior to MOT loading.
2. The cooling beam, repump beam, and MOT magnetic field are turned on to load a new MOT for about 20 seconds. We load the MOT until a MOT of $\sim 3 \cdot 10^9$ atoms is obtained.
3. The CMOT phase occurs for 40 ms by ramping the cooling beam detuning from -4Γ to -7Γ , switching the repump power from 30 mW to 260 μ W, and ramping the MOT magnetic field gradient from 8 G/cm to 0 G/cm.
4. The optical pumping phase occurs for 1 ms with only the cooling beam on.
5. The magnetic field ‘catch’ occurs by turning on a 40 G/cm magnetic field using the MOT coils. We then ramp up the magnetic field to 180 G/cm over 100 ms.
6. Magnetic transfer from the MOT cell into the science cell occurs by employing the series of current ramps through the 14 transfer coil pairs, taking a total of 5.9 seconds.

7. Atoms are transferred from a quadrupole trap created by the final transfer coil pair into a quadrupole trap created by the DC TOP coils by simultaneously ramping the final transfer coils off and the DC TOP coils on over 100 ms.
8. A 5 ms ‘kill pulse’ eliminates any stray $|F = 2\rangle$ atoms that have made it into the science cell.
9. Atoms are transferred into the TOP trap by switching the DC TOP coils’ field strength from 180 G/cm to 300 G/cm and turning the amplitude of the AC TOP coils on to 41 G at 2 kHz. Phase I evaporation occurs in the tight TOP trap over a period of 72 seconds by ramping the bias field from 41 G to 5 G and ramping the RF frequency from 70 MHz to 4.5 MHz.
10. The atoms are transferred to a gravity-sagged TOP trap by ramping the DC TOP coils’ field strength from 300 G/cm to 55 G/cm over 2 seconds, while increasing the RF field.
11. Phase II evaporation occurs over 10 seconds by ramping the RF frequency from 5.0 MHz to 4.7 MHz, forming a BEC.
12. (*Absorption imaging only*) The atomic cloud is allowed to expand for 56 ms with the DC TOP coils on at 55 G/cm, the levitation coil on at 32.4 G, and the AC TOP coils off.
13. (*Absorption imaging only*) A $10\ \mu\text{s}$ ‘repump flash’ pulse pumps the atoms into the $|F = 2\rangle$ state before imaging.
14. The imaging pulse (using either phase-contrast or absorption light) occurs, followed by a background and dark exposure.

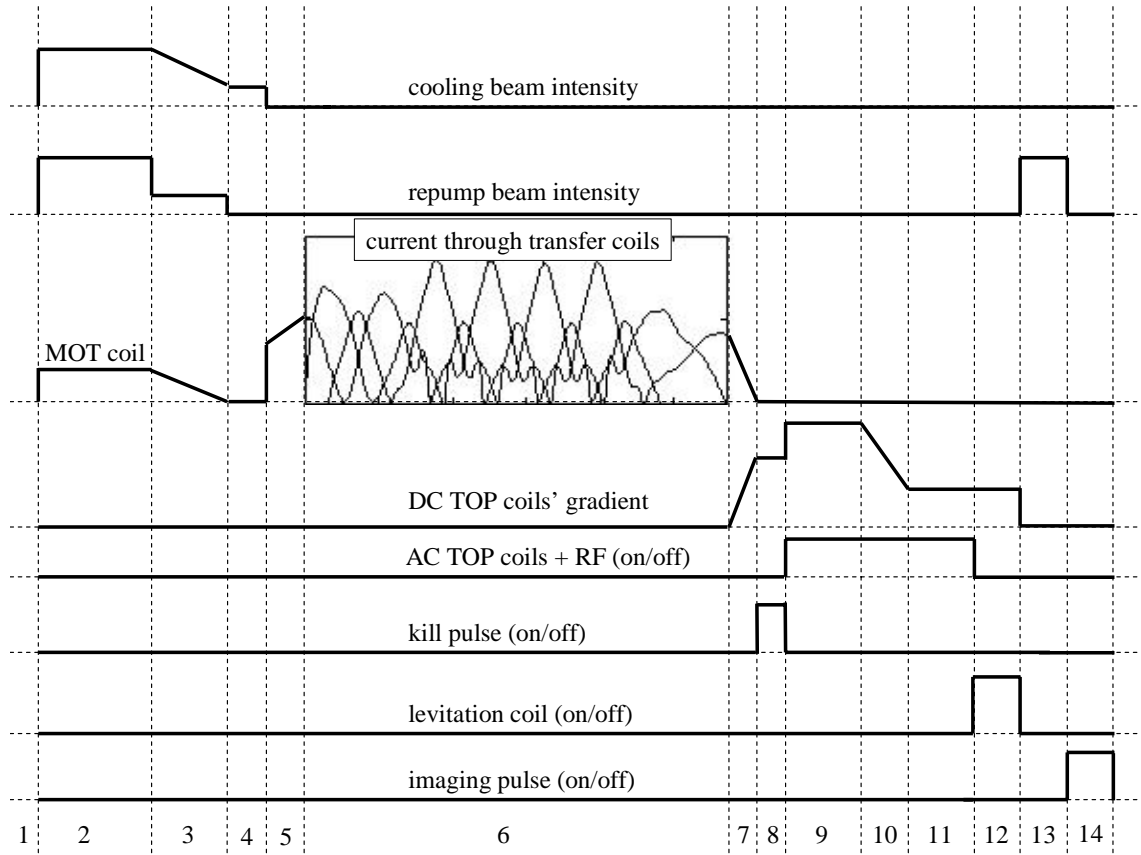


Figure 4.13: Complete BEC formation sequence vs. time. Not to scale on the time or amplitude axes. The different segments of the BEC formation process, described in the text, are: (1) all beams are turned off; (2) MOT loading; (3) CMOT; (4) optical pumping; (5) initial magnetic trap; (6) magnetic transfer to science cell; (7) transfer into quadrupole trap formed by DC TOP coils only; (8) kill pulse; (9) transfer into TOP trap and Phase I evaporation; (10) transfer into gravity-sagged weak TOP trap; (11) Phase II evaporation; (12) (*absorption imaging only*) expansion; (13) (*absorption imaging only*) repump flash pulse; and (14) imaging pulse.

CHAPTER 5

VORTEX FORMATION

5.1 Introduction

Questions such as “*How do vortices form in superfluids? Why is it important to study new mechanisms for vortex generation in superfluids?*” have motivated our experimental search for a new mechanism of vortex formation that relies of the interference between BECs as they are merged. The results of our investigation, published in “Vortex Formation by Merging of Multiple Trapped Bose-Einstein Condensates” [15], are presented in this chapter along with a more detailed description of the background information and concepts relevant to our experiment.

The outline of this chapter is as follows: the background information and concepts relevant to the experiment will be presented, paying particular attention to the notion of phase in a BEC. Then, the specific *research question* will be posed and an explanation of why this research project is novel, important, and unanswered will be given. Finally, the experimental details, procedure, results, and discussion will be presented.

5.2 The Concept of Phase in a BEC

An atomic-gas BEC is a macroscopic occupation of a single quantum state by an ensemble of atoms, and can be described by a macroscopic wavefunction, or order

parameter, $\Psi(\vec{r})$, given by

$$\Psi(\vec{r}) = \sqrt{n(\vec{r})}e^{i\phi(\vec{r})} \quad (5.1)$$

where $n(\vec{r})$ and $\phi(\vec{r})$ are a spatially varying density and phase, respectively [5, 6]¹. This usage of $\Psi(\vec{r})$ is derived from a quantum field theory approach, where formally $\Psi(\vec{r})$ is the expectation value of an atomic field annihilation operator [62]. In the interpretation of $\Psi(\vec{r})$ as a complex wavefunction, one can think of $\sqrt{n(\vec{r})}$ as the amplitude and $\phi(\vec{r})$ as the phase of a complex function within the bounds of mean-field theory. This $\Psi(\vec{r})$ is a solution to the Gross-Pitaevskii equation, which governs the dynamics of the wavefunction $\Psi(\vec{r})$ in an external trapping potential [5]. One fundamental consequence of this description is that the addition of a constant, overall phase a to the wavefunction to make

$$\Psi_2(\vec{r}) = \sqrt{n(\vec{r})}e^{i(\phi(\vec{r})+a)} \quad (5.2)$$

does not alter the physical properties of the wavefunction [63].

5.2.1 The superfluid velocity and quantized vortices

One consequence of the above description is the derivation of the superfluid velocity $\vec{v}(\vec{r})$ as

$$\vec{v}(\vec{r}) = \frac{\hbar}{m}\nabla\phi(\vec{r}), \quad (5.3)$$

where \hbar is Planck's constant and m is the atomic mass. The superfluid velocity $\vec{v}(\vec{r})$ satisfies the following two constraints. First, because it can be written as the gradient of the scalar field $\phi(\vec{r})$, $\vec{v}(\vec{r})$ is an irrotational vector field that satisfies

$$\nabla \times \vec{v}(\vec{r}) = 0. \quad (5.4)$$

Second, by taking the integral of Equation 5.3 around a closed loop, it can be seen that there is a quantization condition on the flux around a closed loop, referred to as the Onsager-Feynman quantization condition:

$$\oint \vec{v}(\vec{r}) \cdot d\vec{l} = n \frac{h}{m} \quad (5.5)$$

where n is an integer [6].

The consequences of the above superfluid formulation are myriad for the case of BEC. First, although the addition of a constant overall phase to the wavefunction carries no physical significance, it is clear from Equation 5.3 that the phase gradient $\nabla\phi(\vec{r})$ determines the rate and direction of superfluid flow given by $\vec{v}(\vec{r})$. Second, the quantization condition of Equation 5.5 has important implications for the existence of quantized vortices within BECs. The phase of the wavefunction $\Psi(\vec{r})$ can be spatially varying, but must be single-valued at any point in space. A situation where the phase increases azimuthally is shown in Figure 5.1. If the phase at a particular point is 0 and increases azimuthally, the phase must be 0, 2π , or some integer multiple thereof upon returning to the original point. This 2π phase winding corresponds to a circulation of $n = 1$ in the quantization condition, and corresponds to the phase winding of a singly-charged vortex. The vorticity or circulation n of Equation 5.3 is the number of 2π phase windings around a central point, referred to as the vortex core. This phase profile results in circular atomic flux around the hollow vortex core, where the density drops to zero and there is a phase singularity.

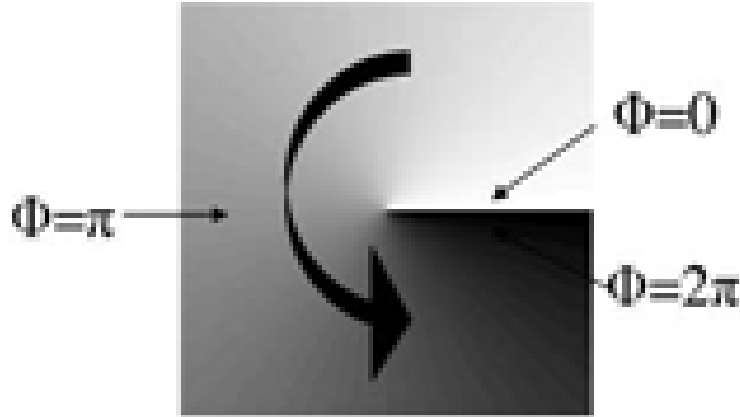


Figure 5.1: 0 to 2π phase winding, corresponding to the phase profile of a singly-charged vortex in a superfluid.

5.2.2 On the relative phase of independent superfluids

A famous *gedanken* experiment of P. W. Anderson proposed the following scenario [64]: imagine that two separate, independent buckets of superfluid He are brought together. When the two superfluids are brought together, will there be superfluid flow? And in which direction? If one had *a priori* knowledge of the relative phase between the superfluid in bucket 1 and the superfluid in bucket 2, one could calculate the direction of fluid flow $\vec{v}(\vec{r})$.

However, a relative phase does not exist until a phase measurement has been made [64, 65, 66]. Upon each realization of the experiment, a direction of fluid flow will be observed, from which a relative phase can be calculated. Repeated trials of the experiment will produce different results. It is the quantum measurement process of interfering the two superfluids that produces a relative phase. It should be emphasized that the *relative* phase is the only physically meaningful variable here, individual overall phases are not physical. We will discuss this *gedanken* experiment in the context of BECs in the following sections.

5.2.3 Example case: interference between two BECs

In this section, we consider the case of two interfering BECs as an example to show how the direction of fluid flow depends on their relative phase. Consider a wavefunction that is a superposition of two Gaussian density distributions, centered at $x = x_0$ and $x = -x_0$, having phases ϕ_1 and ϕ_2

$$\Psi(\vec{r}) = A \cdot [e^{-(x-x_0)^2+i\phi_1} + e^{-(x+x_0)^2+i\phi_2}] \quad (5.6)$$

where A is a normalization coefficient and x is a dimensionless spatial variable. An elementary consequence of the formalism of quantum mechanics shows that the probability current $\vec{J}(\vec{r})$ can be written as

$$\vec{J}(\vec{r}) = \frac{\hbar}{2mi} [\Psi^*(\vec{r}) \nabla \Psi(\vec{r}) - \Psi(\vec{r}) \nabla \Psi^*(\vec{r})] \quad (5.7)$$

for a wavefunction $\Psi(\vec{r})$ [63]. By inserting Equation 5.6 into Equation 5.7, it can be shown that the current at $x = 0$ is proportional to $\sin(\phi_1 - \phi_2)$. In this case, with a wavefunction that can be written as the superposition of two overlapping but otherwise uncorrelated BECs, the direction of fluid flow depends on the sine of the phase difference between the two states. This idea will be expanded upon in Section 5.4.4 to explain the direction of fluid flow in our experiment, which involves three interfering BECs.

5.2.4 Matter-wave interference between two expanding BECs

A experiment similar to the proposed *gedanken* experiment described above was performed in the group of Wolfgang Ketterle at MIT in 1997 [11]. In this experiment, interference between two independent BECs was observed by looking at interference

fringes between two spatially overlapped condensates after a period of ballistic expansion. This experiment was the first to experimentally investigate matter-wave interference between BECs, an idea that will be expanded upon in the experiments reported in this dissertation. In the MIT experiment, two independent BECs were created in a double-well potential and then the two BECs were allowed to expand (and hence overlap) during a period of ballistic expansion. High-contrast interference fringes were observed, providing the initial experimental evidence that BECs are coherent [9] and capable of displaying ‘laser-like’ matter-wave interference. In this experiment, the phase of the interference fringe pattern, a physical quantity that is the result of the relative phase of the two BECs upon interference, would theoretically vary with each trial of the experiment based on the preceding description. However, mechanical instabilities in the experimental setup would have made even a fixed relative phase appear as random in this experiment.

In a later publication, the MIT group continued to explore atom interferometry in a double-well potential [67]. A BEC was formed in a single-well potential that was coherently split into a double-well potential, separating one BEC into two spatially distinct components. The two BECs were then held in the double-well potential for a variable amount of time before being released. As before, in the ballistic expansion process the separate clouds will overlap and interfere, producing visible interference fringes. In this experiment, however, the interference fringe pattern was stable and reproducible from shot-to-shot. A deliberate phase shift could then be applied to one of the condensates, producing a detectable shift in the spatial location of the center of the interference fringes. Reproducible interference patterns between condensates separated for up to 5 ms were measured; this measurement of the coherence time of

the separated condensates was limited to 5 ms due to technical difficulties.

In a third experiment, the MIT group observed interference of BECs split with an atom chip [68]. A BEC was formed in a magnetic potential using a microfabricated atom chip, and the BEC was split into two parts by deforming the trapping potential into a double-well potential. As in the experiment above, the trap was turned off and the separated condensates were allowed to expand and overlap. Interference fringes were again observed, and, surprisingly, in some experimental runs, a fork dislocation appeared in the interference fringe pattern, this fork shape represents the phase winding around a vortex core [69]. The vortex generation mechanism was not fully understood, but it was hypothesized that it was due to the BEC splitting procedure.

These experiments set the stage for an understanding of the basic concepts of matter-wave interference between BECs. It should be pointed out that in these experiments the spatial overlap (and hence interference) of separate BECs was facilitated by a period of ballistic expansion, and that the interference was always between two initially isolated BECs.

5.3 Research Question: *Can vortices be made by merging and interfering independent superfluids?*

In the preceding sections we reviewed two concepts that are fundamental to the understanding of our experiment: (1) the relationship between a 2π phase winding and the existence of quantized vortices in superfluids; and (2) the ability of independent BECs to interfere, with a direction of fluid flow that depends on their relative phase, a quantity that is indeterminate prior to BEC interference. These two concepts will

be combined in an original way in order to answer the research question posed in this dissertation. The purpose of this section is to provide some motivation for our interest in this research project.

The existence of quantized vortices is one of the signature features of superfluid systems [13, 70], and atomic-gas BECs have been a fruitful playground in which to explore superfluid vortex properties since their original observation in BEC in 1999 [71]. Due to the relative ease of microscopic manipulation and detection techniques, BECs are well-suited to address open questions regarding superfluid mixing and associated vortex generation [14, 72, 73]. Vortices were originally created in BEC using quantum phase manipulation [71, 74], and have also been created using methods more analogous to those in classical fluid dynamics [75], namely through rotating traps [76, 77, 78, 79], turbulence [69], and dynamical instabilities [80, 81]. Yet in contrast with classical fluid dynamics, vortex generation via the mixing of initially isolated superfluids has been an unexplored research area.

In this chapter we describe our experiments demonstrating that merging together three condensates in a trap can lead to the formation of quantized vortices in the merged BEC. We ascribe the vortex generation mechanism to matter-wave interference between the initially isolated BECs, and show that vortices may be induced for both slow and fast merging rates. While it is now well-known that matter-wave interference may occur between BECs [11], and that condensates can be gradually merged together into one larger BEC [12], our experiment demonstrates a physical link between condensate merging, interference, and vortex generation, providing a new paradigm for vortex formation in superfluids. We emphasize that no stirring or quantum phase engineering steps are involved in our work; the vortex formation

process is stochastic and uncontrollable, and partially depends on relative quantum phases that are indeterminate prior to condensate merging. This vortex formation mechanism may be particularly relevant for developing further understanding of the roles of potential-well defects, roughness, and disorder on establishing a superfluid state. Furthermore, this work may be viewed as a model for studies of spontaneous symmetry breaking and topological defect formation during phase transitions [82, 83, 84, 85, 86, 87].

5.4 Experimental Details

This section describes some of the technical details of our experimental procedure. Our BEC formation process is reviewed in Section 5.4.1. Use of our three-well atom trap is described in Section 5.4.2, and our method for creation of the three-well trap is described in Section 5.4.3. When the three condensates created in our three-well trap are merged, there will be an atomic fluid flow between the initially independent BECs. The direction of fluid flow is discussed in Section 5.4.4 and the timescale for merging is discussed in Section 5.4.5. As a separate, test experiment, a deliberate method for creating vortices in our BEC is discussed in Section 5.4.6.

5.4.1 BEC formation

Our basic single BEC creation technique was described in detail in Section 4.7. In brief, we first cool a thermal gas of $|F=1, m_F=-1\rangle$ ^{87}Rb atoms to just above the BEC critical temperature in an axially symmetric TOP trap with radial and axial trapping frequencies of 39.8 Hz and 110 Hz, respectively. We then ramp the TOP trap magnetic fields such that the final trap oscillation frequencies are 7.4 Hz

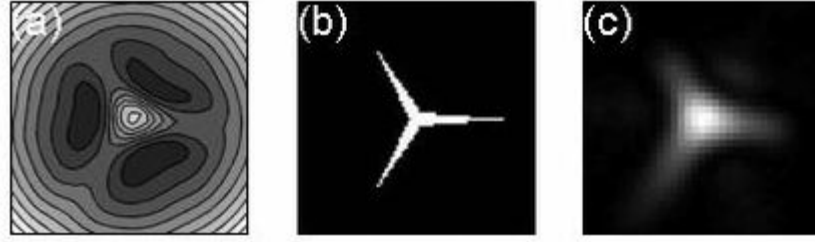


Figure 5.2: (a) Potential energy contour showing a horizontal slice through the center of our three-well trap, representing the addition of the harmonic TOP trap with the measured intensity profile of the optical barrier beam, scaled to a potential energy. (b) The binary mask profile used to create the optical barrier, where white represents the transmitting area. (c) An image of the actual optical barrier profile in the plane of the BEC. The size of images (a) and (c) are $85\ \mu\text{m} \times 85\ \mu\text{m}$.

(radially) and 14.1 Hz (axially). A final 10 second stage of RF evaporative cooling produces a BEC of $\sim 4 \times 10^5$ atoms, with a condensate fraction near 65% and a thermal cloud temperature of ~ 22 nK. The BEC chemical potential is $k_B \times 8$ nK, where k_B is Boltzmann's constant.

5.4.2 Three-well atom trap

To illustrate the basic concept underlying our experiment, we first describe our atom trap, which is formed by the addition of a TOP trap and a central repulsive barrier of axially (vertically) propagating blue-detuned laser light shaped to segment the harmonic oscillator potential well into three local potential minima. Figure 5.2 (a) shows an example of potential energy contours of our three-well potential.

We will assume throughout the ensuing descriptions that the energy of the central barrier is low enough that it has negligible effect on the thermal atom cloud; such is the case in our experiment. However, the central barrier does provide enough potential energy for an independent condensate to begin forming in each of the three

local potential minima from the original thermal cloud. If the central barrier is weak enough, condensates with repulsive interatomic interactions will grow together during evaporative cooling; this is because the individual chemical potentials of each condensate will grow to be greater than the barrier height, thus enabling direct above-barrier transport. If the barrier is strong enough, the condensates will remain independent. In this latter case, the central barrier height may be lowered while keeping the condensed atoms held in the TOP trap. Overlap and interference between the heretofore independent condensates would then be established as the condensates merge together into one.

5.4.3 Making a custom-shaped optical potential

An experiment like this would not have been possible had it not been for our ability to make custom-shaped optical potentials such as that shown in Figure 5.2 (c). We have been able to create such light fields by using the Maskless Lithography Tool (MLT), part of the Laboratory for Diffractive and Micro-Optics run by Dr. Tom Milster at the College of Optical Sciences, Tucson, AZ. The MLT uses a micro-positioned optical beam to etch off chrome from a glass slide. By removing the chrome from specific points on the slide, we can create an arbitrary binary pattern on the mask, such as that shown in Figure 5.2 (b). By focussing a beam through the binary transmission mask, we can create a light beam that looks very similar to the transmission profile of the mask, differing in shape from the mask due to beam quality and the effects of diffraction. The versatility of this tool for experiments in ultracold atomic physics cannot be underestimated, as one can use this tool to create binary masks, and hence light fields, in arbitrary shapes for myriad uses in

atom interferometry and quantum state engineering.

The barrier that partitions our harmonic trap into three wells is formed by illuminating the binary mask shown in Figure 5.2 (b) with a focused blue-detuned Gaussian laser beam of wavelength 660 nm (Mitsubishi model 101J27-01 laser diode). After passing through the mask, the beam enters our vacuum chamber along the vertical trap axis. The mask is imaged onto the center of the atom cloud with a single lens. Due to diffraction, the beam has an intensity profile as shown in Figure 5.2 (c), with a maximum intensity and thus barrier energy aligned with the center of the TOP trap. The barrier's potential energy decreases to zero over $\sim 35 \mu\text{m}$ along three arms separated by azimuthal angles of approximately 120° . A schematic showing the imaging system used for the optical barrier beam is shown in Figure 5.3.

5.4.4 Direction of fluid flow for given relative phases

Our experiment involves BEC formation in a three-well potential formed by the addition of the central repulsive optical barrier beam and the TOP trap potential. In the case of a weak barrier, the condensates will merge together during the final stages of RF evaporative cooling, or, in the case of a strong barrier, will only merge together when the intervening barrier's strength is ramped down to zero while the atoms are held in the TOP trap. Depending on the relative phases of the three condensates and the rate at which the condensates merge together, the final merged BEC may have nonzero net orbital angular momentum about the vertical trap axis.

To demonstrate this, we first envision two condensates in two potential minima merged slowly enough that although interference occurs between the condensate pair, interference *fringes* do not. As merging begins, a directional mass current

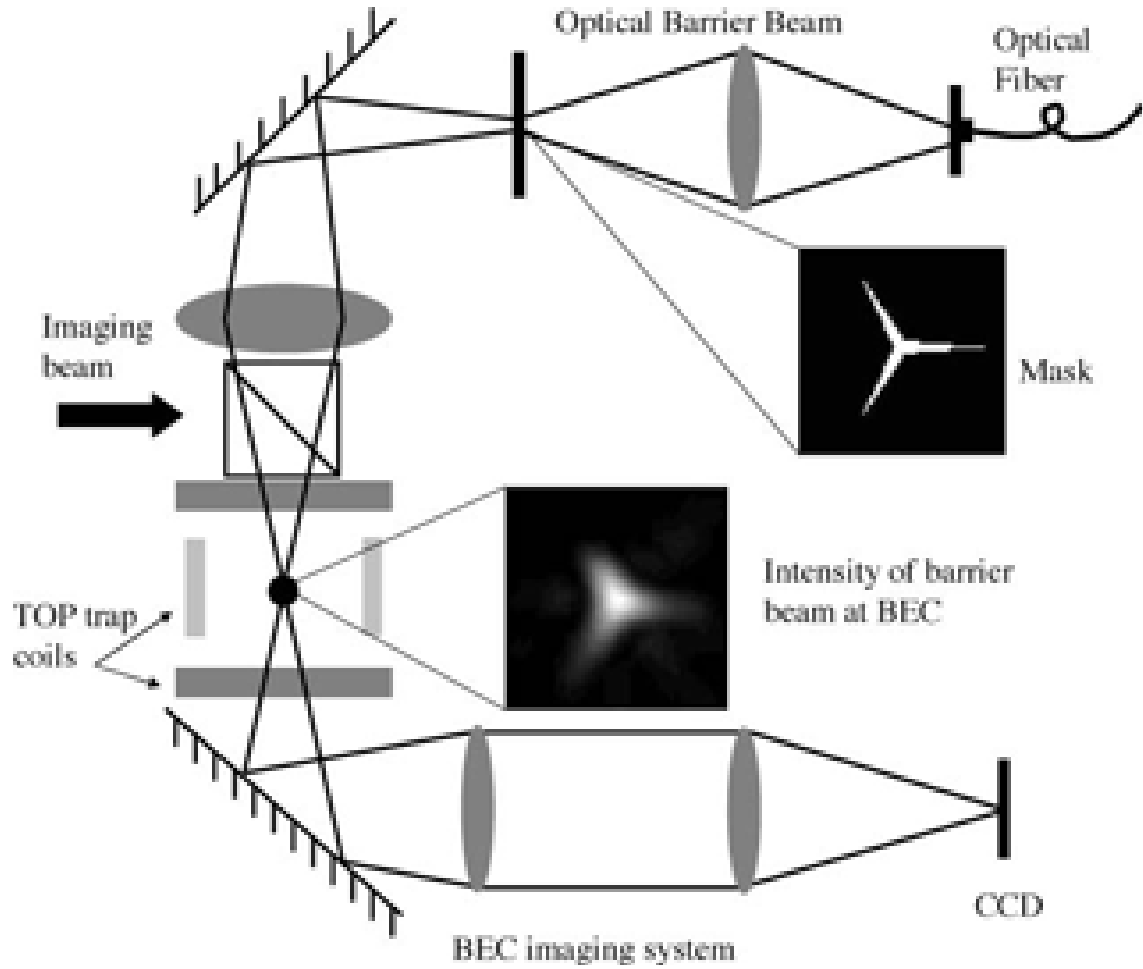


Figure 5.3: Schematic of the experimental setup. The optical barrier beam is coupled from an optical fiber and focussed onto the binary transmission mask. The beam that passes through the binary transmission mask then passes through a polarizing beam-splitter cube and gets imaged by one focussing lens onto the plane of the BEC; the intensity of the optical barrier beam at the plane of the BEC is shown. The vertical imaging beam passes through the other port of the polarizing beam-splitter cube and passes through the BEC vertically, then gets imaged onto the CCD camera. The horizontal imaging system is not shown.

between the pair is established, with the initial direction of above-barrier fluid flow depending on the sine of the phase difference between the overlapping states (as also occurs in the Josephson Effect [88, 89] for the case of tunneling). Recalling that the relative phase between two independent condensates is indeterminate until it is measured via interference, the relative phase and hence fluid flow direction will vary randomly upon repeated realizations of the experiment.

When the three condensates of our experiment are merged together while remaining trapped, a net fluid flow over the barrier arms may occur that is simultaneously either clockwise, counter-clockwise, or neither, relative to the trap center. Recalling that the direction of fluid flow depends on the phase differences between the individual condensates, one can label the condensates formed in the three local minima of Figure 5.2 (a) as $j=1, 2$, and 3 in clockwise order. Upon merging of the three condensates, a value of the relative phases $\Delta\phi_{ij}$ will be established, which we will write as $\Delta\phi_{12}$, $\Delta\phi_{23}$, and $\Delta\phi_{31}$, where $\Delta\phi_{ij} = \phi_i - \phi_j$.

Upon merging of the three condensates, if it turns out that for example, $\Delta\phi_{12} = 0.7\pi$ and $\Delta\phi_{23} = 0.8\pi$ (thus necessarily $\Delta\phi_{31} = 0.5\pi$ since the phase everywhere must be single valued), then some finite amount of clockwise-directed fluid flow will be established between each pair, hence also for the entire fluid. More generally, if the three merging condensates have relative phases $\Delta\phi_{12}$, $\Delta\phi_{23}$, and $\Delta\phi_{31}$ that are each simultaneously between 0 and π , or each between π and 2π , the resulting BEC will have acquired nonzero net orbital angular momentum after the merger, which will be manifest as a vortex within the BEC.

To understand which conditions in the relative phases can produce vorticity, consider Figure 5.4, which examines the full range of phase difference possibilities,

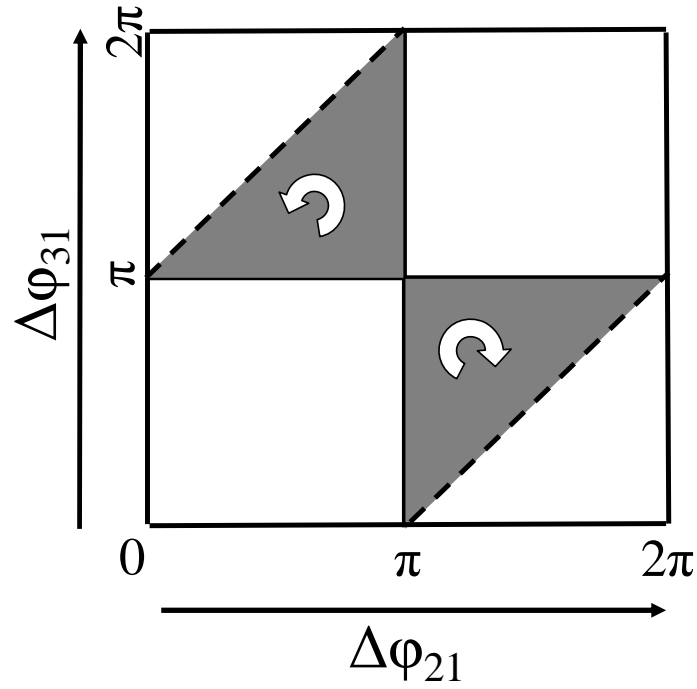


Figure 5.4: Illustration showing which relative phases can lead to a vortex, $\Delta\phi_{21}$ is plotted on the horizontal axis from 0 to 2π , and $\Delta\phi_{31}$ is plotted on the vertical axis over the same range. The phase conditions necessary for clockwise fluid flow over all three barrier arms are contained in the shaded gray region in the lower right-hand corner. A similar region corresponding to counter-clockwise fluid flow is shown as the shaded region in the upper left-hand corner. Given random initial phases between the three condensates, the necessary phase conditions for vortex formation will occur 25% of the time.

plotted as a function of $\Delta\phi_{21}$ and $\Delta\phi_{31}$ over their full range of values from 0 to 2π . The condition for a clockwise fluid flow over all three intervening barriers is $\phi_2 - \phi_1 \geq \pi$, $\phi_3 \geq \phi_2 + \pi$, and $\phi_3 - \phi_1 \leq \pi$, which corresponds to a region occupying $1/8$ of all the possible values of $\Delta\phi_{21}$ and $\Delta\phi_{31}$, shown as a shaded gray region in the lower right-hand corner of Figure 5.4. Another $1/8$ of the chart is occupied by the region allowing for three counter-clockwise fluid flows, therefore there will be a net probability of $P_v = 0.25$ for either direction of fluid flow, given uniformly random relative phases of the condensates upon merging. Because our experiment is not set up to detect the difference between a clockwise and counter-clockwise fluid circulation, P_v is the probability for a singly-charged vortex to form as the three condensates merge together.

This relationship between vortex trapping and relative phases is an application of the so-called geodesic rule [90, 91]. Related work includes a theoretical investigation of three Josephson-coupled BECs [92], yet the geodesic rule also applies to a wider range of topics including spontaneous defect formation in liquid crystals [93, 94].

5.4.5 Timescale for merging

For faster merging rates and correspondingly steeper phase gradients, interference *fringes* may develop as the condensates merge. To estimate the longest time scale τ_f over which two merging condensates can support a single dark interference fringe, we envision two condensates that are initially atomic point sources separated by a distance d , and that each expands to a radius of d over a time τ_f such that the condensates overlap in the intervening region. The condensate expansion speed

$v \sim d/\tau_f$ corresponds to a phase gradient at the side of each condensate of

$$\nabla\phi = \frac{v \cdot m}{\hbar} \sim \frac{d \cdot m}{\tau_f \cdot \hbar} \quad (5.8)$$

where m is the atomic mass. To create a single interference fringe in the overlap region, $\nabla\phi \sim \pi/d$. With $d \sim 35 \mu\text{m}$, appropriate for our experiment, $\tau_f \sim 550 \text{ ms}$; shorter merging times would produce more interference fringes, while longer times correspond to slow merging and no fringes. Each dark fringe will be subject to the same dynamical instabilities as dark solitons and decay to vortices, antivortices, and possibly vortex rings over times on the order of 50 ms [80, 81, 95]. Similar decay has been seen in recent numerical simulations [96]. For condensates merged together over times of τ_f or shorter, we may thus expect to find multiple vortex cores in a BEC, or to find a value of P_v exceeding 0.25.

5.4.6 Making a vortex lattice by rotating an asymmetric TOP trap

Before attempting to produce vortices by merging and interfering multiple BECs, which would only produce vortices with a finite probability, we performed a basic system check to determine if vortex cores using our novel method of generation would be visible. We performed this system check by creating a vortex lattice by placing a BEC in a rotating asymmetric TOP trap; this method was first described by Arlt *et al.* in 1999 [97] and used to create a vortex lattice shortly thereafter [78]. Successful generation of vortex lattices using this method ensured that we were allowing enough time for expansion using the levitation coil scheme and that the vertical imaging system was in focus.

This method ‘squeezes’ the TOP trap along one axis of the $x - y$ (radial) plane, and rotates the axis of trap asymmetry at a frequency that is resonant with the

trap's quadrupolar mode, adding orbital angular momentum to the condensate. The asymmetric trap is characterized by three harmonic oscillator frequencies $\omega_x < \omega_y < \omega_z$. The amount of 'squeezing' of the trap in the $x - y$ plane is characterized by the deformation parameter ϵ , given by

$$\epsilon = \frac{\omega_y^2 - \omega_x^2}{\omega_y^2 + \omega_x^2}, \quad (5.9)$$

where the situation $\epsilon = 0$ corresponds to an axially symmetric TOP trap.

We create this asymmetry in the two horizontal trapping frequencies by combining the signals from two function generators operating at frequencies $\omega_1 = \omega_{TOP} + \omega_{spin}$ and $\omega_2 = \omega_{TOP} - \omega_{spin}$. By letting $\omega_2 = \omega_1$, we can turn off the rotating asymmetry. These signals are both phase-shifted and summed to produce a signal that consists of a slow rotation (the spinning asymmetry at ω_{spin}) superimposed on a fast rotation (the TOP trap rotation at $\omega_{TOP} = 2$ kHz), yielding radial components of the magnetic field that oscillate according to

$$B_x(t) = B_0 \cos(\omega_1 t) + \epsilon \cdot \cos(\omega_2 t) \quad (5.10)$$

$$B_y(t) = B_0 \sin(\omega_1 t) - \epsilon \cdot \sin(\omega_2 t). \quad (5.11)$$

The amount of spinning is characterized by ϵ and ω_{spin} , the amplitude and frequency of the rotating asymmetry, respectively. The average radial trapping frequency ω_\perp is defined as

$$\omega_\perp = \sqrt{\frac{\omega_x^2 + \omega_y^2}{2}}. \quad (5.12)$$

Resonant excitation of the quadrupolar mode of the asymmetric trap will occur when the spinning frequency $\omega_{spin} = \frac{1}{\sqrt{2}} \cdot \omega_\perp$ [98].

The procedure for creating a vortex lattice using this method involves creating a condensate, allowing for a few seconds of spinning in the asymmetric trap at the

resonant spinning frequency, turning off the spinning and letting the cloud equilibrate into a stable triangular vortex lattice in a symmetric TOP trap, and then allowing for a period of expansion before imaging. We have created vortex lattices using this method in the weak gravity-sagged TOP trap with radial trapping frequency of 7.4 Hz, as well as in the tight TOP trap with radial trapping frequency 40 Hz, albeit at a different spinning frequency. In order to generate a high-contrast lattice, it was necessary for us to begin with as pure of a BEC as possible, as even a small amount of thermal component greatly reduced the vortex lattice visibility. However, a small thermal component was still present, enabling damping of the vortex array into an ordered lattice.

Conditions to produce a regular lattice are the following: atoms are transferred into the weak TOP trap with radial trapping frequency of 7.4 Hz. A pure condensate is produced in a 10 second Phase II evaporation step by decreasing the RF evaporation frequency to 4.7 MHz. By instantaneously turning on the rotating trap asymmetry, spinning was induced in the asymmetric trap for 4 seconds, with an amplitude of 0.026 V (peak-to-peak) on the function generator that controls spinning. The frequency of the function generator used for spinning is 11.5 Hz, which corresponds to an actual spinning frequency of 5.75 Hz, or $\sim 0.78 \omega_{\perp}$. During this spin time, the RF frequency was increased to 8 MHz.

After this spinning time, the rotating trap asymmetry was turned off and 6 seconds of equilibration time occurred in the symmetric TOP trap with the RF frequency at 6.5 MHz. It is essential that the RF shield remain on and at a higher than normal value during the spinning and equilibration periods, otherwise the atoms will heat up during these long hold times. We have found that it is necessary to let the

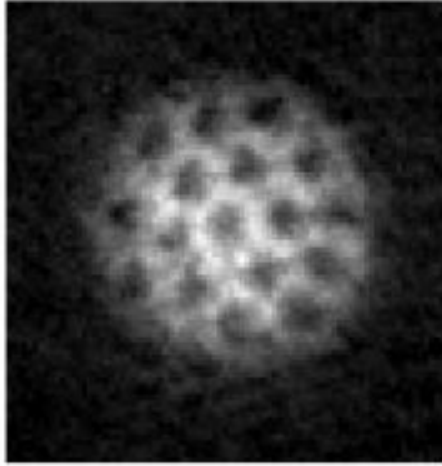


Figure 5.5: Image of a vortex lattice created by rotating an asymmetric TOP trap. The size of the image is $97 \mu\text{m} \times 97 \mu\text{m}$.

BEC equilibrate in the symmetric TOP trap for at least 4 seconds to allow enough time for the lattice to form. After the equilibration period, 56 ms of expansion using the levitation coil scheme occurs before absorption imaging on the vertical axis. An image of a vortex lattice generated using the above recipe is shown in Figure 5.5.

Using the above procedure, we were able to create a vortex lattice of up to ~ 15 vortices by spinning in the weak TOP trap, and were able to see 2 or 3 times more vortices by spinning in a tighter TOP trap. We also investigated the regime of very weak spinning, to see what only a few vortex cores would look like, as our matter-wave interference experiment was designed to look for only a few vortices. Example images of small numbers of vortices generated by weak spinning are shown in Figure 5.6. These images were all generated by using weak spinning amplitudes and short spinning times.

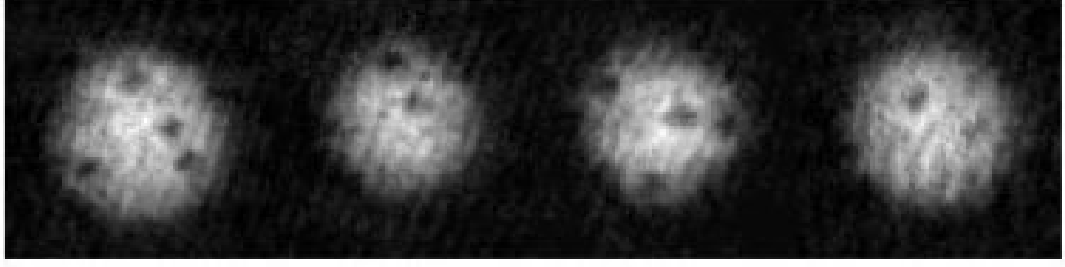


Figure 5.6: Images showing only a few vortices created by rotating an asymmetric TOP trap. The size of each image is $83 \mu\text{m} \times 83 \mu\text{m}$.

5.5 Vortex Formation by Merging Independent BECs

The concept behind our experiment and the experimental details have been presented in the previous sections, sections 5.5 through 5.7 will describe the results of the three major scientific projects presented in this dissertation.

5.5.1 Formation of independent BECs

In the first of three investigations, three spatially isolated condensates were created in the presence of a strong barrier of maximum potential energy $k_B \times 26 \text{ nK}$. To create three isolated condensates in a segmented trap, we modify the BEC formation procedure described in Section 5.4.1 by ramping on the optical barrier beam over 500 ms immediately before the final 10 second stage of evaporative cooling in the weak TOP trap. With $170 \mu\text{W}$ in the beam, which corresponds to a maximum barrier height of $k_B \times 26 \text{ nK}$ for our beam, three condensates are created and do not merge together during their growth. With a strong barrier, tunneling plays no role due to the large barrier width, and the BECs can be considered independent until merged. A set of three BECs created under these conditions is shown in Figure 5.7.

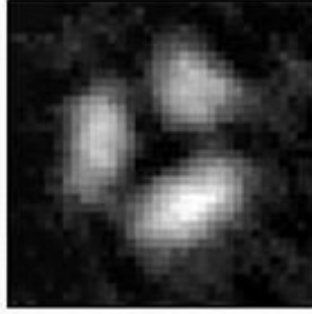


Figure 5.7: In-trap, phase-contrast image of a condensate formed in the presence of a strong barrier. The maximum strength of the optical barrier beam is $170 \mu\text{W}$, strong enough of a barrier to allow for three independent condensates to form in the bottom of each of the wells in the three-well potential. The size of the image is $85 \mu\text{m} \times 85 \mu\text{m}$.

5.5.2 Vortex observation fraction vs. merging time

After BEC formation, the three independent condensates were then merged by linearly ramping down the strength of the barrier to zero over a variable time τ . After the barrier ramp-down, the cloud expands for 56 ms using the levitation coil scheme, and the expanded cloud is imaged using absorption imaging along the vertical axis. This entire process was repeated between 5 and 11 times for each of 6 different values of the barrier ramp-down time τ between 50 ms and 5 s.

In a significant fraction of our images, one or more vortex cores were visible, a clear indication that condensate merging can indeed induce vortex formation. The spatial density distributions varied from shot to shot, as would be expected with indeterminate phase differences between the initial condensates, and many images were absent of vortices. Example images of expanded BECs in Figure 5.8 (a)-(d) show the presence of vortex cores after various barrier ramp-down times.

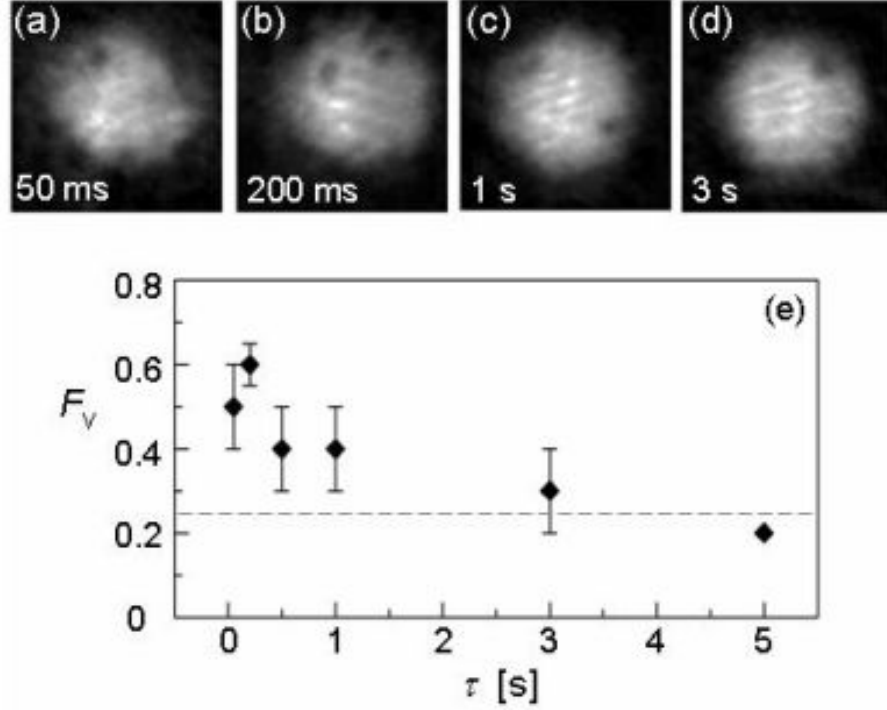


Figure 5.8: Example images of vortices created by merging independent BECs. Images (a)–(d) show vortices in condensates created in the presence of a strong ($k_B \times 26$ nK) barrier. Prior to release from the trap, the barrier was ramped off over the time τ indicated. The size of each image is $170 \mu\text{m} \times 170 \mu\text{m}$. (e) Vortex observation fraction F_v vs. barrier ramp-down time τ . The data for τ values of 50 ms, 200 ms, 500 ms, 1 s, 3 s, and 5 s consisted of 5, 11, 10, 10, 5, and 5 images, respectively. For clarity, statistical uncertainties due to finite sample sizes are not shown, but they generally exceed our counting uncertainties.

An analysis of vortex observation statistics is given in Figure 5.8 (e) for the different values of τ examined. We define the vortex observation fraction F_v as the fraction of images, for each value of τ , that show at least one vortex core. The error bars reflect our uncertainty in determining whether or not an image shows at least one vortex. For example, core-like features at the edge of the BEC or core-like features obscured by imaging noise may lead to uncertainty in our counting statistics and determination of F_v . As the plot shows, F_v displays a maximum of ~ 0.6 for the smaller τ values, and decreases to ~ 0.25 for long ramp-down times. We expect that with larger sample sizes, F_v should approximate P_v for each τ . Thus our results are consistent with our conceptual analysis, where $P_v > 0.25$ for fast merging times, and $P_v = 0.25$ for slow merging times according to the geodesic rule for random initial phase differences. This expected lower limit is represented by the dashed line in Figure 5.8 (e).

Multiple-vortex lifetime vs. single-vortex lifetime

For $\tau \leq 1$ s, multiple vortices were often observed in our images, as those of Figure 5.8 show, perhaps signifying the creation of both vortices and antivortices. Although we are unable to determine the direction of fluid circulation around our observed vortex cores, we performed an additional test in which the barrier was ramped off in 200 ms, forming multiple vortex cores with a high probability such as the ones shown in Figure 5.8 (b). We then inserted additional time in order to hold the final BEC in the unperturbed harmonic trap before our expansion imaging step. After such a sequence, the probability of observing multiple vortices dropped dramatically: for no extra hold time, we observed an average of 2.1 vortex cores

per image, whereas this number dropped to 0.7 for an extra 100 ms of hold time, suggestive of either vortex-antivortex recombination on the 100 ms timescale, or some other dynamical processes by which vortices leave the BEC. However, single vortices were observed even after 5 s of extra hold time in our trap following the 200 ms barrier ramp, indicating relatively long vortex lifetimes in our trap.

5.6 Vortex Formation During BEC Creation

5.6.1 Experimental sequence

In our second investigation, we used only $45 \mu\text{W}$ in the optical barrier beam, corresponding to a maximum barrier energy of $k_B \times 7 \text{ nK}$. Three independent condensates again *initially* form, but as the condensates grow in atom number, their repulsive interatomic interactions eventually provide enough energy for the three condensates to flow over the barrier arms. The three condensates thus naturally merge together into one BEC during evaporative cooling, as shown in the in-trap, phase contrast image of Figure 5.9, taken at the end of the evaporative cooling stage.

We emphasize that this merging process is due solely to the increasing chemical potential of each condensate exceeding the potential energy of the barrier arms between the wells; the barrier strength remained constant throughout the growth and merging of the condensates. After evaporative cooling, we ramped off the optical barrier over 100 ms and released the atoms from the trap to observe the BEC after a period of expansion. Under these conditions, our vortex observation fraction was $F_v = 0.56 \pm 0.06$ in a set of 16 images, with example images shown in Figure 5.10.

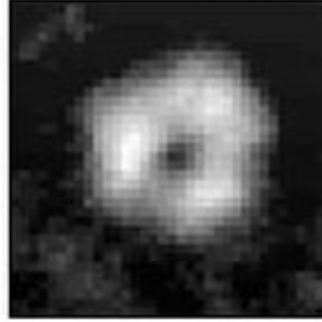


Figure 5.9: In-trap, phase-contrast image of a BEC formed in the presence of a weak barrier. The maximum strength of the optical barrier beam is $45 \mu\text{W}$, weak enough of a barrier to allow the initial condensates to merge together during evaporative cooling. The observable hole in the BEC is due to the beam displacing atoms from the center of the trap. The size of the image is $85 \mu\text{m} \times 85 \mu\text{m}$.

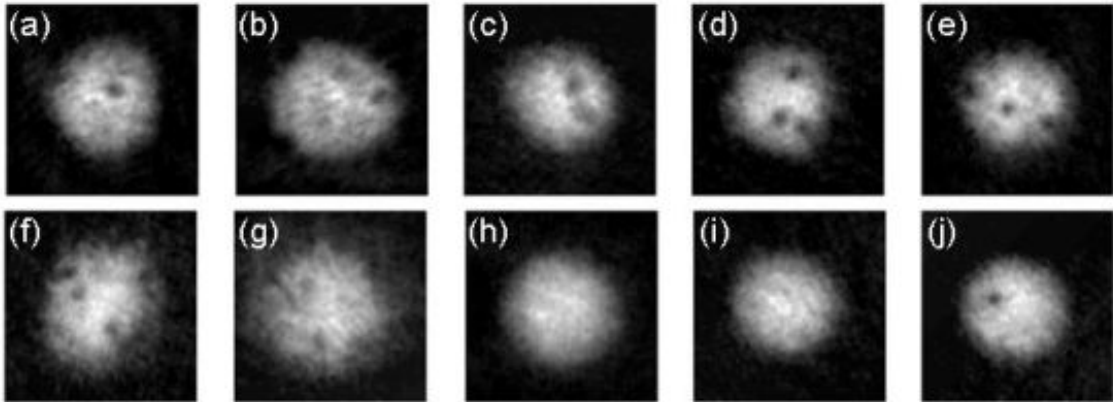


Figure 5.10: Gallery of images from weak, intermediate, and zero barrier strengths. Images (a) and (b) show vortices occurring in condensates created in a potential well with a $k_B \times 7 \text{ nK}$ segmenting barrier. Images (c)–(g) show an array of vortices obtained using intermediate barrier heights. For comparison, image (h) is a typical example of an expansion image without vortex cores present. Images (i) and (j) show BECs created without any central optical barrier. Note the presence of a spontaneously formed vortex in (j). All images are $170 \mu\text{m} \times 170 \mu\text{m}$ wide.

5.6.2 Discussion

By adding an extra 500 ms of hold time after the final 10 second stage of BEC formation but *before* the start of the 100 ms barrier ramp-down and ballistic expansion, the vortex observation fraction decreased to $F_v=0.28\pm0.14$. Again, this drop in probability may be due to vortex-antivortex recombination during extra hold time in the weakly perturbed trap. We thus conclude that with a maximum barrier energy of $k_B\times7$ nK, vortices are formed during the BEC creation process rather than during the ramp down of the weak barrier, consistent with our phase-contrast images of trapped BECs that show a doughnut-like rather than segmented final density distribution.

5.6.3 Intermediate potential barriers

Barrier strengths between the two limits so far described can also lead to vortex formation, either during BEC growth or during barrier ramp-down. With a barrier strength in this range, up to at least four clearly defined vortex cores have been observed in single images, as the examples in Figure 5.10 (c)–(g) show. Density defects other than clear vortex cores have also appeared in our images, as in the upper left of Figure 5.10 (g), where a “gash”-like feature may be a possible indicator of vortex-antivortex recombination; similar features have been seen in related numerical simulations. Often, however, no vortices are observed; an example with no vortex cores is shown in Figure 5.10 (h). For comparison, a BEC created in a trap without a barrier is shown in Figure 5.10 (i).

5.7 Vortex Formation by Splitting and Recombining a BEC

In our third investigation, a single BEC was formed in the tight TOP trap by evaporating to a lower than normal RF frequency. The BEC was then transferred to the weak TOP trap, and a strong optical barrier potential was then turned on. The maximum barrier strength was even larger than in our first investigation, ensuring that we coherently split the pre-formed BEC into three segments. The 10 second Phase II evaporation phase proceeded as usual in the weak TOP trap by decreasing the RF frequency while holding the cloud in the three-well potential². It should be noted that 10 seconds is longer than the phase diffusion time of our BEC, an estimate of which can be made based on the number-phase uncertainty principle. For Poissonian number fluctuations about a mean number of atoms N , the phase diffusion time τ is

$$\tau \approx \frac{5h\sqrt{N}}{2\mu} \quad (5.13)$$

where μ is the chemical potential [67]. Using $N = 1 \cdot 10^5$ atoms and $\mu = k_B \cdot 8$ nK, we expect the phase diffusion time to be $\tau \approx 5$ seconds.

Because the three condensates do not maintain a phase relationship after the 10 second separation time, they can be considered uncorrelated, independent BECs. Just like in our first investigation, by ramping down the strength of the optical barrier beam, the three independent condensates will interfere, and vortices may form. By looking at images of the cloud after a period of expansion, we observed a strong agreement with the results of our first investigation, with a high vortex observation fraction for short merging times decaying to a smaller observation fraction for longer

²The BEC had already been formed at the beginning of this evaporation phase, which only served as an RF shield, continuing to evaporate atoms away from the already-formed BEC.

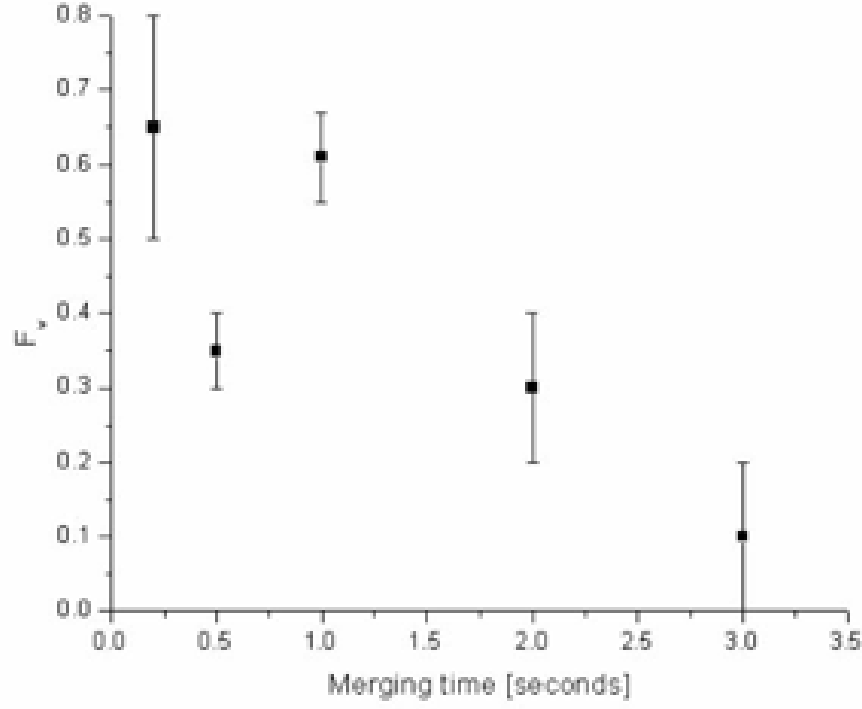


Figure 5.11: Vortex observation fraction F_v vs. merging time τ for splitting and then recombining condensates 10 seconds later. The data for τ values of 200 ms, 500 ms, 1 s, 2 s, and 3 s consisted of 10, 10, 9, 5, and 5 images, respectively.

merging times. A plot of the vortex observation fraction F_v vs. merging time τ for $\tau = 200$ ms, 500 ms, 1 s, 2 s, and 3 s is shown in Figure 5.11.

5.8 Spontaneous Vortices

During the course of the aforementioned experiments, we noticed that single vortex cores appear in $\sim 10\%$ of our expansion images taken in the absence of the optical barrier beam. In other words, for our basic single BEC creation procedure as outlined above, and *without a segmenting barrier ever turned on*, vortices occasionally form spontaneously and are observable in expansion images. Figure 5.10 (i)–(j) show

two example expansion images of condensates taken without any optical barrier in place. Figure 5.10 (j) shows a clear spontaneous vortex core visible in an expansion image taken without the presence of any optical barrier. These observations may be related to predictions of spontaneous vortex formation due to cooling a gas through the BEC transition [82, 83, 84, 85, 86, 87]. We are currently investigating these intriguing observations further.

5.9 Numerical Simulations

As a check on our results and analysis, we used the split-step numerical method [99] to solve the Gross-Pitaevskii equation in simulations of three merging two-dimensional condensates. Details of the simulations will not be given here; however, we mention that the simulations display features qualitatively similar to those seen in our experiment, namely: (1) arbitrarily slow merging gives a 25% probability for vortex formation, given random initial phases, and without formation of any interference fringes (dark solitons); (2) rapid merging leads to interference fringes that decay to multiple vortices and antivortices, which may annihilate each other in the BEC; and (3) as merging times decrease, P_v increases. Our simulations have shown two additional features: (1) slightly asymmetric or off-center barriers, or unequal numbers of atoms in the three wells, can also lead to vortex formation upon merging; and (2) a single vortex core may migrate to and be pinned at the center of the barrier where the energy cost of displacing fluid is low; this may help explain why a weak barrier does not appear to readily destroy all BEC angular momentum.

5.10 Where Does the Angular Momentum Come From?

To generate vortices by the mechanisms described above it is important for three reasons that the condensates merge and interfere while held in a trap. First, in a trapped BEC, the nonlinear dynamics due to interatomic interactions play a key role in the structural decay of interference fringes, which may be responsible for generation of multiple vortices and antivortices seen with fast merging times. Second, by keeping condensates trapped during their mixing, arbitrarily slow merging times and related vortex generation can be studied. Finally, a gas confined in an asymmetric potential can acquire orbital angular momentum from the trap. The barrier in this experiment breaks the trap's cylindrical symmetry, and thus allows for the exchange of orbital angular momentum between the atoms and the trap. The law of conservation of angular momentum is satisfied because the increase in angular momentum of the atomic gas comes from the trap itself.

CHAPTER 6

CONCLUSIONS

This dissertation includes a description of two major accomplishments: (1) the complete construction of an experimental apparatus used to create ^{87}Rb Bose-Einstein condensates; and (2) an experiment that resulted in the formation of vortices by merging and interfering multiple trapped BECs. The following sections summarize the main ideas presented in the description of these two achievements.

6.1 A Review of the Experimental Apparatus

A description of the components, techniques, and procedure used in our method of BEC formation is given in Chapters 2, 3, and 4. In summary, the three major steps in our BEC formation process are: (1) loading atoms in a MOT and transferring them into the initial magnetic trap in the MOT cell; (2) magnetic transfer of atoms from the MOT cell to the science cell; and (3) evaporatively cooling atoms in the TOP trap to form a BEC.

This dissertation includes a description of several novel implementations of previously demonstrated experimental techniques. For example, the advantages attained in using a diverging beam MOT are presented in Section 2.5.1. In addition, a description of a novel system for long-distance transfer of magnetically trapped atoms is presented in Chapter 3. Also, a description of the evaporative cooling sequence used for formation of a ^{87}Rb BEC in a weak ($f = 7.4$ Hz radially) TOP trap is

presented in Section 4.4.2. Finally, the use of the Maskless Lithography Tool to create arbitrary optical potentials is presented in Section 5.4.3.

6.2 A Summary of the Experimental Results

The experiments presented in Chapter 5 demonstrate the formation of vortices by merging initially isolated condensates into one BEC. These experiments link together the ideas of vortex formation, merging of independent condensates, and matter-wave interference between independent condensates in a new way, providing a novel paradigm for vortex formation in superfluids.

Our main results are: (1) vortex observations are consistent with a simple conceptual model regarding the indeterminate phase differences between the initial condensates and their merging rates; and (2) BECs created in the presence of weak trapping potential defects or perturbations, such as our weak optical barrier, may naturally acquire vorticity during BEC formation.

In a broader context, these experiments fit within the field of atom optics, but our observations may be relevant to other areas as well. For example, the formation of vortices in a condensate created in the presence of a weak optical barrier, which may be considered a defect, challenges the notion that a condensate *necessarily* forms with no orbital angular momentum in the lowest energy state of a trapping potential. We have shown that the shape of a static confining potential may be sufficient to induce vortex formation during condensate growth, a concept that may be important in the closely related field of superconductivity [100, 101].

6.3 Directions for Future Research

The work presented in this dissertation provides many avenues for further research. First, it is very scientifically interesting to be able to form a condensate in a smooth harmonic trap in a state that contains vorticity. This is something that we have seen in our experiment, the observation of single vortices in $\sim 10\%$ of our experimental runs. Because these spontaneous vortices occur with such infrequency, we do not currently have enough information on their occurrence to make quantitative predictions. Additional data, such as spontaneous vortex observation probability vs. condensation rate, RF evaporation time, and TOP trap trapping frequency need to be gathered in order to understand this new phenomenon and be able to compare it to theoretical predictions. This is the subject of current work in our research group.

Second, a measure of the phase coherence time of a split BEC could be made using our experimental setup. By forming one BEC and then coherently splitting it into three segments by turning on a strong optical barrier beam, we can partition a condensate into three segments. Then, one can hold the atoms in the three-well potential for a variable hold time before ramping down the barrier and looking at the vortex observation fraction. This is similar to the experiment described in Section 5.7, but with varying hold times. In the experiment described in Section 5.7, vortices have been observed to occur $\sim 25\%$ of the time when merging the condensates slowly, an observation that is consistent with our conceptual model of three interfering superfluids with indeterminate relative phases. For hold times less than the phase diffusion time of the split condensates, the condensates should still maintain a phase coherence, and the vortex observation probability may differ from the above $\sim 25\%$. For hold times larger than the phase diffusion time, we

expect the vortex observation probability to approach the $\sim 25\%$ seen for independent, uncorrelated BECs. We could therefore use our experimental apparatus for a measurement of the phase diffusion time of a split condensate, a measurement that has been previously performed by looking at interference fringes between condensates in expansion [67]. Our method has distinct advantages compared to looking at interference fringes in expansion: (1) by looking at interference between trapped condensates, we can explore arbitrarily long merging times; and (2) vortices are long-lived topological states in superfluids, whereas interference fringes are subject to decay and instability.

APPENDIX A

COHERENT MBR-110 AND VERDI V-10 LASER OPERATION TIPS

Over the years our research group has obtained considerable experience in using the Coherent MBR-110 titanium:sapphire laser, pumped by a Verdi V-10. This appendix is meant to serve as a resource for other users of the MBR laser and provide information on working with the optics and electronics of the MBR and Verdi.

Alignment of the MBR-110

As a safeguard in case misalignment should occur, two irises should be placed in the beam path between the Verdi and the MBR. These will be helpful in case the alignment of either of the two steering mirrors is lost. If lasing of the MBR is lost because of the two steering mirrors, lasing should be re-gained using only those two steering mirrors. In the event that this is not possible, or if something in the cavity gets misaligned, a full alignment of the MBR will need to be performed.

Preliminaries Generally, intracavity mirror adjustments should be performed with the tweeter disconnected, as the tweeter is always trying to maintain lock. The etalon tune knob should be adjusted so that it is fully clockwise, then the etalon will be at the maximum angle with respect to the intracavity beam, and back-reflections off of the etalon will diverge quickly and not be mistaken for something else.

Pump Beam Initial Setup The pump beam coming into the MBR should be level with the optical table and at a height of 4". This can be checked by placing an iris at a height of 4" directly in front of the MBR input window. The floor of the MBR cavity is 1" above the optical table, and an iris at a height of 3" will just fit in between the second focusing lens and mirror M1. The height of the pump beam can be set using these two irises. The horizontal adjustment of the pump beam can be set by placing the pump beam in the center of the two focusing lenses and the ti:sapphire crystal.

Index Card As a position reference for the laser beam inside the cavity, make an index card ~ 1 " wide and ~ 2 " tall with a horizontal line 28 mm from the bottom of the card and two vertical lines separated by 2 mm running up and down the middle of the card.

Pump Beam Alignment into Cavity As this point it is helpful to turn the pump beam power all the way down so you can see the beam comfortably. The pump beam should be centered on M2 and at the height of the horizontal line on the index card (from now on, everything should be at the 28 mm height). Use M2 to align the pump beam onto the M3. The pump should be centered vertically on M3 and approximately 1 mm to the left of center (*left, right* always mean from the viewpoint of an observer traveling with the the beam we are aligning). Use M3 to align the pump beam onto M4, it should be at the correct height vertically and horizontally centered on M4 and the output window. Use M4 to align the pump beam back onto M1. This is difficult because it is not possible to put a card in front of M1, as this blocks the input pump beam. But with the card as close as possible, you can get the height and horizontal position close enough to start.

Alignment of Fluorescence Spots The pump beam causes fluorescence out of the ti:sapphire crystal in all directions. The procedure to obtain lasing consists of getting the fluorescence in the forwards direction (ti:sapphire \rightarrow M2 \rightarrow M3 \rightarrow M4 \rightarrow M1) and the fluorescence in the backwards direction (ti:sapphire \rightarrow M1 \rightarrow M4 \rightarrow M3 \rightarrow M2) to be coincident. It is helpful to block the green pump beam while looking at the fluorescence spots, a convenient place to put the orange filter is against the walls 1" in front of M3. Remember that the orange filter will prevent lasing.

Fluorescence Spots on M3 After placing the index card in front of M3, two fluorescence spots should be visible to the human eye (we are working with 780 nm). One is the forwards spot coming from M2, this should be a round spot 2 mm in diameter. The other is the backwards spot coming from M4, this should be a slightly rectangular spot 1 $\frac{1}{2}$ mm tall and 1 mm wide. Set the spacing between the spots to be 2 mm on the index card. If you could place the card directly on M3, the two fluorescence spots would be coincident and centered on M3. The green pump beam will be slightly to the left of center on M3 because of dispersion.

Fluorescence Spots on M4 With the index card placed in front of M4, look for fluorescence spots on M4. It is necessary to use goggles that block the green light because of the large amount of scatter on M4. At least 2 fluorescence spots will be visible on M4. The backwards spot comes from M1 through the BRF; looking at this spot before the BRF, it looks like a round spot 6 mm in diameter. A small bright dot should be visible right in the middle of this spot. This round spot gets clipped by the BRF, so by the time it gets to M4, it is only a few mm wide. The bright dot should still be visible, however, and it will probably be right-of-center

with respect to the clipped beam. Depending on the angle of the BRF the clipping may not be purely from the left and the right, it may be angled. There may also be a much larger and weaker fluorescence glow behind all this, this is just scatter from the BRF. The second spot we need to align on M4 is the forwards spot, from M3. This is a slightly rectangular spot, $1 \frac{1}{2}$ mm tall and 1 mm wide. Align the center of the forwards spot to be 3-4 mm separated from the small bright dot of the backwards spot, and at the correct height. If you could place the index card on M4 directly, the beams would be coincident and approximately centered on M4. They should also be approximately centered on the output window.

Closing the cavity Now all that's left is closing the resonator cavity, which is done by 'connecting' mirror M4 to M1. It may be possible to look at the forwards spot after one round trip near M1, but you can't put a card right on M1. The forwards fluorescence spot should be visible outside of the cavity. When you are close to lasing, you can see a small second spot (from the second round trip through the cavity) appear outside of the cavity as well. This second spot (there is even a third when you are very close) is very difficult to see, even with an IR viewer. At this point the best thing to do is to walk the beam around horizontally with mirrors M1 and M4 and look for lasing outside of the cavity. Place a lens and a fast, high-responsivity photodiode directly outside of the laser, and remove the orange filter from the cavity and place it in front of the photodiode, which we'll use to monitor lasing. Small walks on the horizontal adjustments of M1 and M4 should produce lasing, which will register as a sharp increase on the photodiode. If you still can't get the laser to lase, another thing to try is to make the spots on M3 slightly closer than 2 mm apart and the spots on M4 4 mm apart. You can also remove the etalon from the cavity if it is in danger of clipping the beam.

Peaking up the Power Once lasing is obtained, peaking up the power is probably going to be easiest with a power meter placed right at the output of the laser. In general, the intracavity mirrors should be walked in order to peak up the power. The two external steering mirrors should NOT be walked, as this is counter-productive to our strategy. We want to align the cavity so that it is optimal for the existing pump beam, not the other way around. However, small tweaks on one of the external steering mirrors may be useful, after the intracavity alignment procedure is performed.

Do a 2-mirror walk between mirrors M1 and M4, and M2 and M3, and keep repeating this for a while. When this no longer produces gains, you can try walking M3 and M4, or M2 and M4. At some point you will probably want to clean all the optics in the cavity, as this can get you up to ~ 200 mW more power. Close the

Verdi shutter and re-obtain lasing after cleaning each component, in case alignment gets lost by bumping something.

Peaking up the power The following things can be adjusted to peak up the output power:

1. The angle of the input polarizer before the input window to the MBR.
2. The position of the focusing lenses, although adjusting these is not recommended unless you have poor mode quality.
3. The angle of the quartz crystal in the optical diode. Also make sure that it is not clipping.
4. The horizontal position of the housing for the magnet assembly of the optical diode. Make sure it is not clipping.
5. The angle of the BRF.
6. The position of the etalon. Dropping the etalon out of the cavity will not stop lasing, you should lose no more than ~ 200 mW by letting the etalon back in the cavity. Changing the location of where the beam hits the etalon can make a difference in output power, but be careful: this can also affect what the appropriate etalon drive frequency needs to be.

Electronics of the MBR-110

Occasionally it is necessary to peak up the electronics of the MBR because the laser does not stay in etalon lock or servo lock. The main indicator of an electronics problem with the MBR is the etalon sawtooth signal. This signal should have a peak-to-peak voltage of at least 1 V, and should display a rapid rise and slow fall when the etalon tune knob is turned clockwise. If the etalon sawtooth signal displays a slow rise and rapid fall when turning the tune knob clockwise, the MBR will lock to and lase at multiple frequencies until the phase is corrected by adjusting DIL switch SW10 in the controller box.

If the amplitude of the etalon sawtooth error signal is less than 500 mV peak-to-peak, the laser will have trouble locking and an electronics peak-up should be performed by adjusted some of the potentiometers in the MBR controller box. This peak-up may be as simple as adjusting PR14 (this is the fine adjustment of the etalon drive frequency) while rotating the etalon tune knob until a larger sawtooth signal is obtained. If this does not work, a full electronics peak-up is recommended.

This procedure is designed to adjust the amplitude, frequency, and phase of the etalon drive signal. If done correctly, it should adjust the drive signal to be

in resonance with the natural resonance frequency of the etalon, and the etalon sawtooth error signal will increase.

Preliminaries Two phases of the etalon drive voltage are available at TP5 and TP7. Use TP5 to trigger a scope for the rest of the procedure.

Etalon drive voltage adjustment Using a probe on the etalon itself, monitor the peak-to-peak amplitude of the etalon drive voltage. If this is different from the voltage given on the spec. sheet (~ 4 V peak-to-peak) adjust PR16 until it is corrected.

Etalon frequency adjustment Monitor TP6 on a scope. AC couple the scope and increase the sensitivity. Adjust PR14 (etalon drive frequency fine adjustment) and PR15 (etalon drive frequency course adjustment) until the amount of ‘breathing’ on TP6 is maximized. This breathing is when alternate peaks in the modulation signal differ by the maximum amount possible upon rotation of the etalon tune knob. Zero breathing corresponds to a sine wave, and full breathing corresponds to an oscillatory modulation signal that alternates between high and low peaks.

Etalon frequency fine adjustment Monitor TP8 on a scope. Turn off the MBR controller power, disconnect the umbilical cable to the laser head, and turn the power back on. Connect a jumper between TP9 and TP6. Maximize the amplitude of the signal on TP8 by adjusting capacitor CT1 (a non-metal tool should be used to adjust this capacitor). When you are done, turn the power off, disconnect the jumper, reconnect the umbilical, and turn the power back on.

Etalon phase adjustment Monitor TP10 on a scope. Adjust the signal on PR17 (0-90° etalon phase adjustment) until TP10 looks as symmetric as possible. After these adjustments, check that the amplitude of the etalon sawtooth error signal has increased.

Verdi V-10 Controller

The diodes in the controller that pump the Verdi via the umbilical cord are placed on temperature and current interlocks. Over time, the amount of current needed to operate these diodes so that they output the appropriate power to pump the Verdi will increase; this is due to a gradual degradation in the efficiency of the diodes. Our diodes, after being in use for ~ 4000 hours, will go into overcurrent mode when we try to turn on the Verdi to its maximum power of 10 W, because the current

in the pump diodes is too high. We are able to operate the Verdi at high powers, however, by first turning it on to 9 W and gradually increasing the output power.

Verdi V-10 Output Window

We have noticed that the output window of the Verdi V-10 will occasionally obtain a water stain on the *inside* of the hermetically sealed glass output window of the shutter assembly. This is visible by shining a flashlight onto the Verdi output window and looking directly into the laser. In addition to degrading the Verdi output beam quality, this causes a small amount of focussing of the Verdi output beam, and will result in decreased output power of the MBR. We remove the Verdi shutter assembly and clean the inside of the glass output window about once a year.

REFERENCES

- [1] S. N. Bose *Z. Phys*, vol. 26, no. 178, 1924.
- [2] A. Einstein *Sitzungsber. Kgl. Preuss. Aka. Wiss.*, vol. 261, 1924.
- [3] A. Einstein *Sitzungsber. Kgl. Preuss. Aka. Wiss.*, vol. 3, 1925.
- [4] E. Cornell and C. Wieman, “The Bose-Einstein condensate,” *Scientific American*, vol. 278, no. 3, pp. 40–45, 1998.
- [5] F. Dalfovo, S. Giorgini, L. Pitaevskii, and S. Stringari, “Theory of Bose-Einstein condensation in trapped gases,” *Reviews of Modern Physics*, vol. 71, no. 3, pp. 463–512, 1999.
- [6] A. Leggett, “Bose-Einstein condensation in the alkali gases: Some fundamental concepts,” *Reviews of Modern Physics*, vol. 73, no. 2, pp. 307–356, 2001.
- [7] J. Anglin and W. Ketterle, “Bose-Einstein condensation of atomic gases,” *Nature*, vol. 416, pp. 211–218, 2002.
- [8] P. Meystre, *Atom Optics*. Springer, 2001.
- [9] M. Kasevich, “Coherence with Atoms,” *Science*, vol. 298, no. 5597, p. 1363, 2002.
- [10] E. Hecht, *Optics*. Reading, MA: Addison-Wesley Publishing Company, 1987.
- [11] M. Andrews, C. Townsend, H. Miesner, D. Durfee, D. Kurn, and W. Ketterle, “Observation of Interference Between Two Bose Condensates,” *Science*, vol. 275, no. 5300, pp. 637–641, 1997.
- [12] A. Chikkatur, Y. Shin, A. Leanhardt, D. Kielpinski, E. Tsikata, T. Gustavson, D. Pritchard, and W. Ketterle, “A Continuous Source of Bose-Einstein Condensed Atoms,” *Science*, vol. 296, no. 5576, pp. 2193–2195, 2002.
- [13] D. Tilley and J. Tilley, *Superfluidity and Superconductivity*. Hilger, 1986.
- [14] R. Srinivasan, “Vortices in Bose-Einstein condensates: A review of the experimental results,” *Pramana-J. Phys*, vol. 66, no. 1, 2006.
- [15] D. Scherer, C. Weiler, T. Neely, and B. Anderson, “Vortex Formation by Merging of Multiple Trapped Bose-Einstein Condensates,” *Physical Review Letters*, vol. 98, no. 11, p. 110402, 2007.

- [16] M. Anderson, J. Ensher, M. Matthews, C. Wieman, and E. Cornell, "Observation of Bose-Einstein Condensation in a Dilute Atomic Vapor," *Science*, vol. 269, no. 5221, p. 198, 1995.
- [17] K. Davis, M. Mewes, M. Andrews, N. van Druten, D. Durfee, D. Kurn, and W. Ketterle, "Bose-Einstein Condensation in a Gas of Sodium Atoms," *Physical Review Letters*, vol. 75, no. 22, pp. 3969–3973, 1995.
- [18] C. Bradley, C. Sackett, J. Tollett, and R. Hulet, "Evidence of Bose-Einstein Condensation in an Atomic Gas with Attractive Interactions," *Physical Review Letters*, vol. 75, no. 9, pp. 1687–1690, 1995.
- [19] C. Bradley, C. Sackett, J. Tollett, and R. Hulet, "Errata: Evidence of Bose-Einstein Condensation in an Atomic Gas with Attractive Interactions," *Physical Review Letters*, vol. 79, no. 6, pp. 1170–1170, 1997.
- [20] J. Ensher, *The First Experiments with Bose-Einstein Condensation of ^{87}Rb* . PhD thesis, University of Colorado, 1999.
- [21] H. Lewandowski, *Coherences and correlations in an ultracold Bose gas*. PhD thesis, University of Colorado, 2002.
- [22] B. DeMarco, *Quantum Behavior of an Atomic Fermi Gas*. PhD thesis, University of Colorado, 2001.
- [23] M. Matthews, *Two-Component Bose-Einstein Condensation*. PhD thesis, University of Colorado, 1999.
- [24] P. Haljan, *Vortices in a Bose-Einstein Condensate*. PhD thesis, University of Colorado, 2003.
- [25] H. Lewandowski, D. Harber, D. Whitaker, and E. Cornell, "Simplified System for Creating a Bose-Einstein Condensate," *Journal of Low Temperature Physics*, vol. 132, no. 5, pp. 309–367, 2003.
- [26] E. Streed, A. Chikkatur, T. Gustavson, M. Boyd, Y. Torii, D. Schneble, G. Campbell, D. Pritchard, and W. Ketterle, "Large atom number Bose-Einstein condensate machines," *Review of Scientific Instruments*, vol. 77, no. 2, p. 23106, 2006.
- [27] D. Stamper-Kurn, *Peeking and poking at a new quantum fluid: Studies of gaseous Bose-Einstein condensates in magnetic and optical traps*. PhD thesis, Massachusetts Institute of Technology, 2000.
- [28] W. Ketterle, D. Durfee, and D. Stamper-Kurn, "Making, probing and understanding Bose-Einstein condensates," *Arxiv preprint cond-mat/9904034*, 1999.

- [29] C. Monroe, W. Swann, H. Robinson, and C. Wieman, "Very cold trapped atoms in a vapor cell," *Physical Review Letters*, vol. 65, no. 13, pp. 1571–1574, 1990.
- [30] J. Moore, C. Davis, and M. Coplan, *Building Scientific Apparatus*. Addison-Wesley, 1983.
- [31] D. Steck, "Rubidium 87 D Line Data, revision 1.6," *Source*—<http://steck.us/alkalidata>, 2003.
- [32] P. Hobbs, *Building electro-optical systems*. Wiley New York, 2000.
- [33] P. Hobbs, "Reaching the shot noise limit for \$10," *Optics & Photonics News*, vol. 2, no. 4, pp. 17–23, 1991.
- [34] P. Hobbs, "Ultrasensitive laser measurements without tears," *Appl. Opt.*, vol. 36, no. 4, pp. 903–920, 1997.
- [35] P. Hobbs, "Photodiode front ends The REAL story," *Optics & Photonics News*, vol. 12, no. 4, pp. 44–47, 2001.
- [36] J. Graeme, *Photodiode Amplifiers: OP AMP Solutions*. McGraw-Hill Professional, 1996.
- [37] A. Arnold, J. Wilson, and M. Boshier, "A simple extended-cavity diode laser," *Review of Scientific Instruments*, vol. 69, no. 3, p. 1236, 1998.
- [38] C. Hawthorn, K. Weber, and R. Scholten, "Littrow configuration tunable external cavity diode laser with fixed direction output beam," *Review of Scientific Instruments*, vol. 72, no. 12, p. 4477, 2001.
- [39] K. Corwin, Z. Lu, C. Hand, R. Epstein, and C. Wieman, "Frequency-stabilized diode laser with the Zeeman shift in an atomic vapor," *Appl. Opt.*, vol. 37, no. 15, pp. 3295–3298, 1998.
- [40] C. Cohen-Tannoudji and W. Phillips, "New mechanisms for laser cooling," *Physics Today*, vol. 43, no. 10, pp. 33–40, 2006.
- [41] C. Foot, "Laser cooling and trapping of atoms," *Contemporary Physics*, vol. 32, p. 369, 1991.
- [42] H. Metcalf and P. Van der Straten, *Laser Cooling and Trapping*. Springer, 1999.
- [43] E. Raab, M. Prentiss, A. Cable, S. Chu, and D. Pritchard, "Trapping of Neutral Sodium Atoms with Radiation Pressure," *Physical Review Letters*, vol. 59, no. 23, pp. 2631–2634, 1987.

- [44] K. Gibble, S. Kasapi, and S. Chu, “Improved magneto-optic trapping in a vapor cell,” *Optics Letters*, vol. 17, no. 7, p. 526, 1992.
- [45] P. Bouyer, P. Lemonde, M. Dahan, A. Michaud, C. Salomon, and J. Dalibard, “An Atom Trap Relying on Optical Pumping,” *Europhys. Lett.*, vol. 27, no. 8, pp. 569–574, 1994.
- [46] W. Petrich, M. Anderson, J. Ensher, and E. Cornell, “Behavior of atoms in a compressed magneto-optical trap,” *J. Opt. Soc. Am. B*, vol. 11, no. 8, p. 1332, 1994.
- [47] A. Migdall, J. Prodan, W. Phillips, T. Bergeman, and H. Metcalf, “First Observation of Magnetically Trapped Neutral Atoms,” *Physical Review Letters*, vol. 54, no. 24, pp. 2596–2599, 1985.
- [48] M. Greiner, I. Bloch, T. Hänsch, and T. Esslinger, “Magnetic transport of trapped cold atoms over a large distance,” *Physical Review A*, vol. 63, no. 3, p. 31401, 2001.
- [49] T. Bergeman, G. Erez, and H. Metcalf, “Magnetostatic trapping fields for neutral atoms,” *Physical Review A*, vol. 35, no. 4, pp. 1535–1546, 1987.
- [50] G. Arfken and H. Weber, *Mathematical Methods for Physicists*. Academic Press, New York, 2005.
- [51] M. Henry, “Magneto Optical Trap and Transfer Coil Control Circuit,” 2004.
- [52] S. Papp and C. Wieman, “Observation of Heteronuclear Feshbach Molecules from a ^{85}Rb - ^{87}Rb Gas,” *Physical Review Letters*, vol. 97, no. 18, p. 180404, 2006.
- [53] W. Petrich, M. Anderson, J. Ensher, and E. Cornell, “Stable, Tightly Confining Magnetic Trap for Evaporative Cooling of Neutral Atoms,” *Physical Review Letters*, vol. 74, no. 17, pp. 3352–3355, 1995.
- [54] D. Pritchard, “Cooling Neutral Atoms in a Magnetic Trap for Precision Spectroscopy,” *Physical Review Letters*, vol. 51, no. 15, pp. 1336–1339, 1983.
- [55] M. Mewes, M. Andrews, N. van Druten, D. Kurn, D. Durfee, and W. Ketterle, “Bose-Einstein Condensation in a Tightly Confining dc Magnetic Trap,” *Physical Review Letters*, vol. 77, no. 3, pp. 416–419, 1996.
- [56] J. Grienkamp, *Field Guide to Geometrical Optics*, vol. FG01, SPIE Field Guides. SPIE, 2004.

- [57] K. Davis, M. Mewes, and W. Ketterle, “An analytical model for evaporative cooling of atoms,” *Applied Physics B: Lasers and Optics*, vol. 60, no. 2, pp. 155–159, 1995.
- [58] C. Sackett, C. Bradley, and R. Hulet, “Optimization of evaporative cooling,” *Physical Review A*, vol. 55, no. 5, pp. 3797–3801, 1997.
- [59] W. Ketterle and N. van Druten, “Evaporative cooling of trapped atoms,” *Adv. At. Mol. Opt. Phys.*, vol. 37, no. 181, p. 40, 1996.
- [60] A. Thomas, *Ultra-cold Collisions and Evaporative Cooling of Caesium in a Magnetic Trap*. PhD thesis, University of Oxford, 2004.
- [61] T. Esslinger, I. Bloch, and T. Hänsch, “Bose-Einstein condensation in a quadrupole-Ioffe-configuration trap,” *Physical Review A*, vol. 58, no. 4, pp. 2664–2667, 1998.
- [62] A. Leggett and F. Sols, “On the concept of spontaneously broken gauge symmetry in condensed matter physics,” *Foundations of Physics*, vol. 21, no. 3, pp. 353–364, 1991.
- [63] C. Cohen-Tannoudji, B. Diu, and F. Laloe, *Quantum Mechanics*. 1986.
- [64] P. Anderson, *The Lesson of Quantum Theory*, edited by J. de Boer, E. Dal, and O. Ulfbeck (Elsevier, Amsterdam, 1986). 1986.
- [65] J. Javanainen and M. Wilkens, “Phase and Phase Diffusion of a Split Bose-Einstein Condensate,” *Physical Review Letters*, vol. 78, no. 25, pp. 4675–4678, 1997.
- [66] W. Mullin, R. Krotkov, and F. Laloë, “The origin of the phase in the interference of Bose-Einstein condensates,” *American Journal of Physics*, vol. 74, p. 880, 2006.
- [67] Y. Shin, M. Saba, T. Pasquini, W. Ketterle, D. Pritchard, and A. Leanhardt, “Atom Interferometry with Bose-Einstein Condensates in a Double-Well Potential,” *Physical Review Letters*, vol. 92, no. 5, p. 50405, 2004.
- [68] Y. Shin, C. Sanner, G. Jo, T. Pasquini, M. Saba, W. Ketterle, D. Pritchard, M. Vengalattore, and M. Prentiss, “Interference of Bose-Einstein condensates split with an atom chip,” *Physical Review A*, vol. 72, no. 2, p. 21604, 2005.
- [69] S. Inouye, S. Gupta, T. Rosenband, A. Chikkatur, A. Görlitz, T. Gustavson, A. Leanhardt, D. Pritchard, and W. Ketterle, “Observation of Vortex Phase Singularities in Bose-Einstein Condensates,” *Physical Review Letters*, vol. 87, no. 8, p. 80402, 2001.

- [70] R. Donnelly, *Quantized Vortices in Helium II*. Cambridge University Press, 1991.
- [71] M. Matthews, B. Anderson, P. Haljan, D. Hall, C. Wieman, and E. Cornell, “Vortices in a Bose-Einstein Condensate,” *Physical Review Letters*, vol. 83, no. 13, pp. 2498–2501, 1999.
- [72] A. Aftalion, “Properties of vortices in Bose-Einstein condensates,” *CR Physique*, vol. 5, pp. 9–20, 2004.
- [73] P. Kevrekidis, R. Carretero-González, D. Frantzeskakis, and I. Kevrekidis, “Vortices in Bose-Einstein Condensates,” *Modern Physics Letters B*, vol. 18, no. 30, pp. 1481–1505, 2004.
- [74] A. Leanhardt, A. Görlitz, A. Chikkatur, D. Kielpinski, Y. Shin, D. Pritchard, and W. Ketterle, “Imprinting Vortices in a Bose-Einstein Condensate using Topological Phases,” *Physical Review Letters*, vol. 89, no. 19, p. 190403, 2002.
- [75] G. Batchelor, “An Introduction to Fluid Mechanics,” *Cambridge University Press, Cambridge*, 1980.
- [76] K. Madison, F. Chevy, W. Wohlleben, and J. Dalibard, “Vortex Formation in a Stirred Bose-Einstein Condensate,” *Physical Review Letters*, vol. 84, no. 5, pp. 806–809, 2000.
- [77] J. Abo-Shaeer, C. Raman, J. Vogels, and W. Ketterle, “Observation of vortex lattices in Bose-Einstein condensates,” *Science*, vol. 292, no. 5516, pp. 476–479, 2001.
- [78] E. Hodby, G. Hechenblaikner, S. Hopkins, O. Maragò, and C. Foot, “Vortex Nucleation in Bose-Einstein Condensates in an Oblate, Purely Magnetic Potential,” *Physical Review Letters*, vol. 88, no. 1, p. 10405, 2001.
- [79] P. Haljan, I. Coddington, P. Engels, and E. Cornell, “Driving Bose-Einstein-Condensate Vorticity with a Rotating Normal Cloud,” *Physical Review Letters*, vol. 87, no. 21, p. 210403, 2001.
- [80] B. Anderson, P. Haljan, C. Regal, D. Feder, L. Collins, C. Clark, and E. Cornell, “Watching Dark Solitons Decay into Vortex Rings in a Bose-Einstein Condensate,” *Physical Review Letters*, vol. 86, no. 14, pp. 2926–2929, 2001.
- [81] Z. Dutton, M. Budde, C. Slowe, and L. Hau, “Observation of quantum shock waves created with ultra-compressed slow light pulses in a Bose-Einstein condensate,” *Science*, vol. 293, no. 5530, pp. 663–668, 2001.

- [82] T. Kibble, “Topology of cosmic domains and strings,” *J. Phys. A: Math. Gen.*, vol. 9, no. 8, 1976.
- [83] W. Zurek, “Cosmological experiments in superfluid helium?,” *Nature*, vol. 317, pp. 505–508, 1985.
- [84] P. Drummond and J. Corney, “Quantum dynamics of evaporatively cooled Bose-Einstein condensates,” *Physical Review A*, vol. 60, no. 4, pp. 2661–2664, 1999.
- [85] J. Anglin and W. Zurek, “Vortices in the Wake of Rapid Bose-Einstein Condensation,” *Physical Review Letters*, vol. 83, no. 9, pp. 1707–1710, 1999.
- [86] R. Marshall, G. New, K. Burnett, and S. Choi, “Exciting, cooling, and vortex trapping in a Bose-condensed gas,” *Physical Review A*, vol. 59, no. 3, pp. 2085–2093, 1999.
- [87] L. Sadler, J. Higbie, S. Leslie, M. Vengalattore, and D. Stamper-Kurn, “Spontaneous symmetry breaking in a quenched ferromagnetic spinor Bose-Einstein condensate,” *Nature*, vol. 443, no. 7109, pp. 312–315, 2006.
- [88] B. Josephson, “Possible new effects in superconductors,” *Phys. Lett.*, vol. 1, pp. 251–3, 1962.
- [89] R. Feynman, “Feynman lectures on physics. Volume 3: Quantum mechanics,” *Reading*, 1965.
- [90] M. Berry, “The Adiabatic Phase and Pancharatnam’s Phase for Polarized Light,” *Journal of Modern Optics*, vol. 34, no. 11, pp. 1401–1407, 1987.
- [91] J. Samuel and R. Bhandari, “General Setting for Berry’s Phase,” *Physical Review Letters*, vol. 60, no. 23, pp. 2339–2342, 1988.
- [92] K. Kasamatsu and M. Tsubota, “Modulation Instability and Pattern Formation in Two-component Bose-Einstein Condensates,” *Journal of Low Temperature Physics*, vol. 138, no. 3, pp. 669–674, 2005.
- [93] I. Chuang, R. Durrer, N. Turok, and B. Yurke, “Cosmology in the Laboratory: Defect Dynamics in Liquid Crystals,” *Science*, vol. 251, no. 4999, p. 1336, 1991.
- [94] M. Bowick, L. Chandar, E. Schiff, and A. Srivastava, “The Cosmological Kibble Mechanism in the Laboratory: String Formation in Liquid Crystals,” *Science*, vol. 263, no. 5149, pp. 943–945, 1994.
- [95] D. Feder, M. Pindzola, L. Collins, B. Schneider, and C. Clark, “Dark-soliton states of Bose-Einstein condensates in anisotropic traps,” *Physical Review A*, vol. 62, no. 5, p. 53606, 2000.

- [96] N. Whitaker, P. Kevrekidis, R. Carretero-Gonzalez, and D. Frantzeskakis, “Formation of Vortices, Vortex Necklaces and Vortex Rings in Sliced Condensates,” *Arxiv preprint cond-mat/0610242*, 2006.
- [97] J. Arlt, O. Marago, E. Hodby, S. Hopkins, G. Hechenblaikner, S. Webster, and C. Foot, “Bose-Einstein condensation in a rotating anisotropic TOP trap,” *Journal of Physics B*, vol. 32, pp. 5861–69, 1999.
- [98] N. Parker and C. Adams, “Response of an atomic Bose–Einstein condensate to a rotating elliptical trap,” *J. Phys. B: At. Mol. Opt. Phys*, vol. 39, pp. 43–55, 2006.
- [99] G. Agrawal, *Nonlinear Fiber Optics*. Academic Press, 2001.
- [100] S. Tung, V. Schweikhard, and E. Cornell, “Observation of Vortex Pinning in Bose-Einstein Condensates,” *Arxiv preprint cond-mat/0607697*, 2006.
- [101] M. Baert, V. Metlushko, R. Jonckheere, V. Moshchalkov, and Y. Bruynseraede, “Composite Flux-Line Lattices Stabilized in Superconducting Films by a Regular Array of Artificial Defects,” *Physical Review Letters*, vol. 74, no. 16, pp. 3269–3272, 1995.